ABSTRACT

Title of Dissertation: On the Typical and Average Contributions to the Persistent Current in Mesoscopic Rings

Enrique Manher Quinto Jariwala, Doctor of Philosophy, 2004

Dissertation directed by: Professor Richard A. Webb
Department of Physics

Low-temperature measurements of the magnetic response of one or more electrically-isolated, micron-sized metallic rings yield an unexpected yet unequivocal result: the presence of equilibrium *persistent* currents, with nanoampere-sized amplitudes and either h/e- or $h/2e$-periodicity in the applied magnetic flux. This effect follows from the extended phase coherence of the conduction electrons in this disordered mesoscopic system. As with transport phenomena, this thermodynamic effect demonstrates sample-specific as well as ensemble-averaging qualities common to mesoscopic physics. With few exceptions, however, there is strong disagreement between the different theoretical calculations and the few successful experiments to date.

For this thesis work, we have designed and executed a unique and unprecedented new experiment: the measurement of the sign, amplitude, and temperature dependences of both the typical and average current contributions to the

h/e- and $h/2e$-periodic magnetic response of the same sample of thirty mesoscopic Au rings. Of particular interest here is the innovative design of our custom SQUID-based detector as well as the unusually long phase coherence of electrons in our lithographically-patterned Au sample. Remarkably, both the typical and average contributions are diamagnetic in sign near zero field, over multiple cooldowns, and comparable in magnitude per ring to the Thouless scale E_c of energy level correlations. Taken in conjunction with earlier experiments, the new data strongly challenge conventional theories of the persistent current.

On the Typical and Average Contributions to the Persistent Current in Mesoscopic Rings

by

Enrique Manher Quinto Jariwala

Dissertation submitted to the Faculty of the Graduate School of the
University of Maryland at College Park in partial fulfillment
of the requirements for the degree of
Doctor of Philosophy
2004

Advisory Committee:

Professor Richard A. Webb, Chairman/Advisor
Professor J. Robert Anderson
Professor H. Dennis Drew
Professor Christopher J. Lobb
Professor Ichiro Takeuchi
Professor Frederick C. Wellstood

TABLE OF CONTENTS

LIST OF TABLES

LIST OF FIGURES

Chapter 1

Introduction

Nearly half a century ago, the physicist Richard Feynman gave an informal talk entitled "There's plenty of room at the bottom" [1], in which he openly speculated about the limits of miniaturization, offered a wide assortment of ideas for manipulating and controlling objects at ever smaller length scales, and in turn described the future of nanotechnology with remarkable foresight. Most notably, he predicted that the room-sized computing machines of his time could be shrunk in size but multiplied in power dramatically using wires and elements on the order of hundreds of nanometers. But Feynman also ruminated on many other far-off subjects, including the storage of information digitally as microscopic bits on the surface of appropriate substrates, the manufacture of nanoscale structures using electron-beam lithography and precision evaporation, the synthesis of made-to-order materials grown layer by atomic layer, and even the interdisciplinary possibilities of performing microsurgery using machines *in vivo* or observing and controlling individual molecules of biological interest.

But more than a list of technological predictions, Feynman's talk was a scientific call to arms, an invitation to enter a new field of physics that we today call

mesoscopics. In the everyday macroscopic world, classical mechanics applies and the collective behavior of billions of atoms determines the properties of materials. In the mesoscopic world, quantum mechanics and the sample-specific behavior of individual atoms lead to novel, yet fundamental, low-energy corrections to both transport and thermodynamic properties, especially when measured at temperatures approaching absolute zero. As Feynman emphasized, as we transition down to microscopic dimensions, "we are working with different laws, and we can expect to do different things" [1].

One very different and uniquely mesoscopic phenomenon is the persistent current in normal-metal rings. Consider an electrically-isolated, micron-sized metallic ring, as shown in Fig. 1.1. Low-temperature measurements of the magnetic response of one or more such ordinary rings yield amazing results: the presence of equilibrium persistent currents, with nanoampere-scale amplitudes and either h/e- or $h/2e$-periodicity in applied magnetic flux. Generally speaking, the persistent current follows from the phase coherence of conduction electrons circumnavigating the rings; however, the size and robustness of the effect appear to run contrary to our expectations from ensemble-averaged statistical mechanics. Over the last decade, considerable effort has been put forth to explain more precisely the different contributions to the persistent current, observed in either single rings or in very large arrays of rings [2–10]. With few exceptions, however, more questions than answers remain regarding the detailed behavior of the persistent current, for which both experimental data as well as theoretical understanding are in short supply.

For this thesis, we propose a new experiment, investigating the different statistical contributions to the persistent current, through a novel measurement

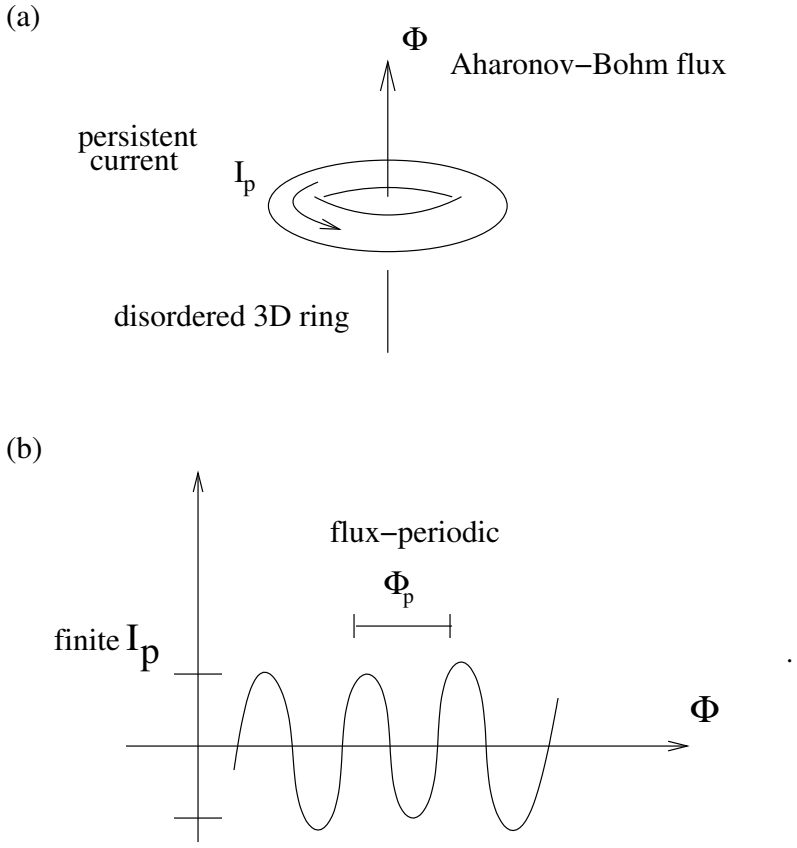

Figure 1.1: The persistent current in an isolated, metallic ring. (a) In the presence of an applied magnetic flux Φ, an ordinary micron-sized conducting ring demonstrates a uniquely quantum-mechanical phenomenon: an equilibrium persistent current I_p carried by phase-coherent conduction electrons. (b) The measured amplitude of this nanoampere-sized current oscillates with specific periodicity in the flux quanta Φ_p passing through the ring. A decade after the first experiments, the full picture of this complex phenomenon remains incomplete.

of the h/e- as well as the $h/2e$-periodic magnetic response of a single mesoscopic sample. With a unique configuration of thirty weakly-disordered Au rings in a linear array, we are able to explore the ensemble-average as well as the sample-specific response of each ring to a finite magnetic field. To summarize, we observe an unexpected diamagnetic (negative) response, nanoampere-sized amplitudes, and weak exponential temperature dependences for both the h/e and $h/2e$ components of the magnetic response. Taken in conjunction with previous experiments, these results pose a significant challenge to conventional theories of the persistent current.

The majority of this thesis focuses on the design, execution, and analysis of our SQUID-based measurements of the persistent current. We begin in Ch. 2 with an introduction to some key concepts from mesoscopic physics research. In Ch. 3, we review the persistent current problem itself, distinguishing between the typical and the average current contributions, as explored in previous experimental and theoretical work. Ch. 4 introduces our specific research purpose, including the motivation and design of our new experimental effort. In Chs. 5 and 6, we present the bulk of our measurements and analyze the results in the context of previous experiments. In the cross-examination in Ch. 7, we anticipate some criticism of our results and perform additional tests to rule out several systematic errors. Finally, Ch. 8 both summarizes our research conclusions and reviews the notable original contributions of this thesis.

Chapter 2

Background

In mesoscopic physics, the fundamental concept is the phase coherence time τ_φ, the time during which an electron maintains its quantum phase coherence while traversing a sample. Like many other mesoscopic phenomena, the persistent current is a quantum interference effect that reflects this extended phase coherence at low temperatures, even in disordered samples with static impurities or dislocations. In this Chapter, we introduce some key concepts for understanding mesoscopic electron transport in general, including the requirements for reduced dimensionality and the relevant length and energy scales. We also discuss the measurements of weak localization, conductance fluctuations, and the electron-electron interaction correction to the resistance, laying the foundation for understanding phase coherence and ensemble-averaging in the persistent current problem.

2.1 Mesoscopic Electron Transport

The term *mesoscopics* historically refers to the transition from macroscopic to microscopic dimensions, in which the usually hidden underpinnings of quan-

tum mechanics begin to modify our classical understanding of condensed-matter physics [11]. Specifically, mesoscopic phenomena are manifested as small but measurable quantum interference corrections to classical transport and thermodynamic properties such as conductivity and magnetization [12–16]. As laboratories for testing textbook principles in actual devices, even the simplest mesoscopic systems can yield significant insights.

Consider for example a simple wire with metallic conductivity, as shown in Fig. 2.1. We can assume that this long meandering wire of total length L with a narrow width w and thickness t has a finite resistance R. According to the Drude model, the major contribution to the resistivity $\rho = Rwt/L$ at very low temperatures follows from the elastic scattering of conduction electrons by randomly-arranged impurities and defects [17]. Assuming an average time τ_e between such scattering events, the electronic conductivity σ is given by:

$$\sigma \equiv \frac{1}{\rho} = \frac{ne^2\tau_e}{m_e} = \frac{ne^2}{m_e}\left(\frac{\ell_e}{v_F}\right), \tag{2.1}$$

where typically (for Au and Cu) the electron number density $n \sim 10^{22}\,\mathrm{m}^{-3}$ and the Fermi velocity $v_F \sim 10^6\,\mathrm{m/s}$. We define here a characteristic length scale $\ell_e = v_F\tau_e$ for elastic scattering called the *mean free path*, which can be calculated through a careful four-terminal measurement of the resistance. (Typically, we find $\ell_e \sim 10^{-8}\,\mathrm{m}$. See Ch. 5.) The important assumption here for classical physics is that electrons move along classical trajectories between scattering events or, equivalently, that the mean free path ℓ_e is much greater than the Fermi wavelength λ_F of the electron [17].

Alternatively, the conductivity can also be described by the Einstein relation:

$$\sigma = \mathcal{N}_0\, e^2 D, \tag{2.2}$$

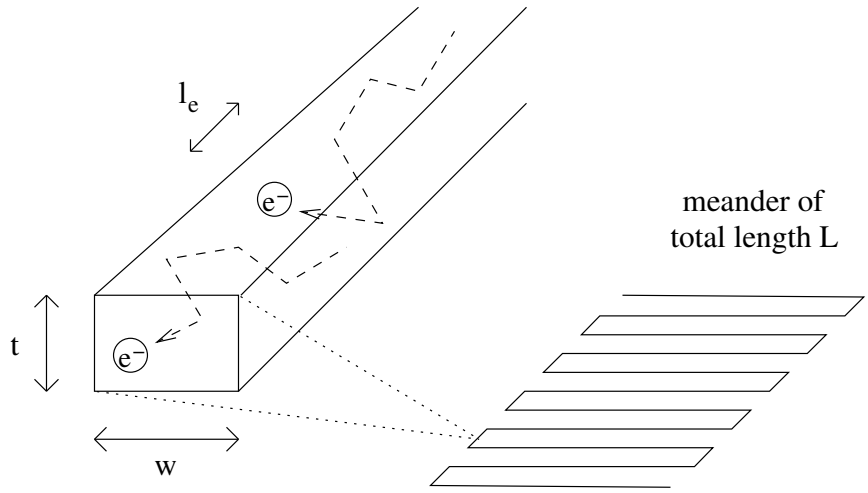

Figure 2.1: Electron diffusion in a lithographically-fabricated mesoscopic system of reduced dimensionality. For this metallic conducting wire of length L but narrow width w and thickness t, electrons effectively diffuse in only one direction if the mean free path ℓ_e is greater than both w and t. A series of four-terminal measurements of the meander's resistance $R \equiv R(H,T)$ yields the diffusion length scale ℓ_e and the diffusion constant D.

$d = 1$	$L > \ell_e$	$\ell_e \geq w, t$	$D = v_F \ell_e$
$d = 2$	$L, w > \ell_e$	$\ell_e \geq t$	$D = \frac{1}{2} v_F \ell_e$
$d = 3$	$L, w, t > \ell_e$		$D = \frac{1}{3} v_F \ell_e$

Table 2.1: Classical dimensionality for diffusive motion. The effective dimension d used for calculating the classical diffusion constant D follows from comparison of the sample's physical dimensions L, w, t to the elastic mean free path ℓ_e.

where $\mathcal{N}_0 \equiv dn/dE$ is the electron density of states and D is the diffusion constant [17]. For the metallic case, the connection to ℓ_e and the Drude model is through the definition $D \equiv \frac{1}{d} v_f \ell_e$, which characterizes the diffusive motion of electrons through the wire as they scatter elastically. Normally $d = 3$, referring to the macroscopic three-dimensional case where all three dimensions are much greater than the mean free path ℓ_e. But, in the mesoscopic regime, we use $d = 1$, for example, if two of the dimensions are less than or equal to ℓ_e. In this case, the width w and thickness t may be larger than λ_F, but electrons effectively diffuse in only one dimension, traversing the length L in a characteristic time defined by:

$$\tau_D \equiv \frac{L^2}{D} \,. \tag{2.3}$$

We summarize the dimensionality requirements for calculating the diffusion constant D in Table 2.1.

We also use the diffusion constant in a similar definition:

$$\tau_\varphi \equiv \frac{L_\varphi^2}{D} \,, \tag{2.4}$$

where L_φ is the average distance an electron travels without losing phase coherence. We note that the phase coherence length L_φ can be many times longer than

the mean free path ℓ_e, since individual elastic scattering events need not change the quantum state of the electron. Finally, taking dimension into account, we can define the conductance G as:

$$G \equiv \sigma L^{d-2}. \tag{2.5}$$

Interestingly, many mesoscopic corrections to the conductance become more readily apparent in systems with reduced dimensionality ($d < 3$) [12–14].

The physical dimensions also factor into the definitions of two relevant energy scales for describing mesoscopic systems. The first is the mean level spacing Δ between energy levels:

$$\Delta = \frac{1}{2\mathcal{N}_0\mathcal{V}}\,, \tag{2.6}$$

which can be significant (on the order of μK in temperature units) for systems with small volumes $\mathcal{V} = Lwt$. This discreteness defined by Δ is in contrast to the continuous energy spectrum of macroscopic samples. The second important energy scale is the Thouless energy E_c, which follows from the diffusion time τ_D:

$$E_c = \frac{\hbar}{\tau_D} = \frac{\hbar D}{L^2}\,. \tag{2.7}$$

Typically on the order of mK, the Thouless energy in effect indicates the scale of correlations of electron energy levels around the Fermi energy E_F in a disordered system of finite length $L < L_\varphi$ [18]. (For systems where $L_\varphi < L$, we replace L with L_φ in Eq. (2.7).) From a theoretical standpoint, the Thouless energy E_c and the mean level spacing Δ together determine the basic behavior of a mesoscopic system [19]; but it is the more phenomenological concept of the phase coherence time τ_φ that informs our understanding of uniquely mesoscopic effects, such as the weak localization correction to the resistance.

2.2 Weak Localization

In mesoscopic physics, the classical picture of a well-defined electron trajectory is replaced by a probabilistic sum over of all possible paths for an electron traversing a sample, leading to small but measurable quantum interference corrections to the conductance G in the classical Drude model. The first correction is known as the weak localization (WL) correction and arises as a result of the quantum interference of electron waves among pairs of time-reversed paths [20, 21]. More importantly, weak localization measurements serve as the primary tool for determining the phase coherence time τ_φ in a disordered sample [22, 23].

In the path-integral formulation of Feynman and Hibbs [24], the resistance of a sample can be calculated as the sum of all possible partial wavefunctions for an electron, as shown in Fig. 2.2(a). Fig. 2.2(b) shows two specific paths, one being the time-reversed counterpart of the other. Because the difference in phase acquired by each path is equal, these paths interfere constructively, increasing the calculated probability of finding the electron at the intersection spot. This yields a change ΔG_{WL} in the conductance:

$$\Delta G_{\mathrm{WL}} \sim \frac{e^2}{\pi\hbar}\left(\frac{L_\varphi}{L}\right) \tag{2.8}$$

that is directly proportional to the effective length scale L_φ for electron phase coherence. Correspondingly, the longer the phase coherence length L_φ, the more pairs of paths contribute to the weak localization correction.

This weak localization effect can be quantitatively determined by making a low temperature four-terminal measurement of the magnetoresistance [22, 23]. By applying a magnetic field, time-reversal symmetry is broken and weak localization is destroyed. This appears in a magnetoresistance trace as a small bump

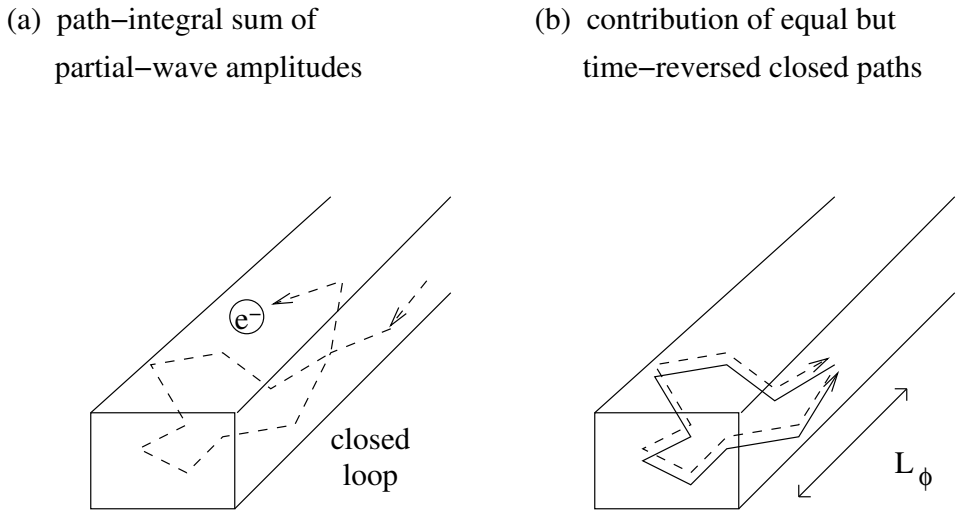

Figure 2.2: Weak localization and pairs of time-reversed paths. (a) Among all possible paths for a single electron, some may self-intersect and form closed loops, as shown. (b) The probability amplitudes of a self-intersecting path and its time-reversed pair add constructively, resulting in a small change in the resistance. These pairs of time-reversed paths are more numerous if L_φ is long.

or dip near zero field, as shown in Fig. 2.3. Though representing only a 0.1% change in the total resistance, this small correction can typically be fit to the theory [20] to yield a value for the phase coherence length L_φ.

Due to the spin of the electron, the formula for quasi-1D weak localization (where $w, t < L_\varphi$) contains both a triplet and singlet term [25]:

$$\begin{aligned} \frac{\Delta R}{R} &= \frac{e^2}{\pi\hbar}\left(\frac{R}{L}\right) \\ &\times \underbrace{\left\{\frac{3}{2}\left(\frac{1}{{L_\varphi}^2}+\frac{4}{3{L_{\rm so}}^2}+\frac{(ewB)^2}{3\hbar^2}\right)^{-\frac{1}{2}}\right.}_{\text{triplet term}} \underbrace{\left.-\frac{1}{2}\left(\frac{1}{{L_\varphi}^2}+\frac{(ewB)^2}{3\hbar^2}\right)^{-\frac{1}{2}}\right\}}_{\text{singlet term}} \end{aligned} \tag{2.9}$$

where $L_{\rm so}$ is the spin-orbit scattering length and $L_{\rm H} = \sqrt{3}\,\hbar/ewB$ is the magnetic phase-breaking length. For strong spin-orbit scattering ($L_{\rm so} << L_\varphi$), the triplet term is negligible, leaving only the contribution from the singlet term:

$$\frac{\Delta R}{R} = -\frac{1}{2}\frac{e^2}{\pi\hbar}\left(\frac{R}{L}\right)\left(\frac{1}{{L_\varphi}^2}+\frac{(ewB)^2}{3\hbar^2}\right)^{-\frac{1}{2}} \tag{2.10}$$

The data in Fig. 2.3 corresponds to this strong spin-orbit scattering case, leading to a dip (instead of a bump) in the resistance near zero field. Over the years, the experimental techniques for measuring weak localization have been refined to provide standard determinations of phase coherence times and lengths in a wide variety of materials, and over a range of cryogenic temperatures [22,23]. In Ch. 5, we present our own measurements of weak localization in the context of the persistent current problem.

2.3 Conductance Fluctuations

In a weak localization measurement, the sample length L is typically many times longer than the phase coherence length L_φ; in essence, weak localization can be

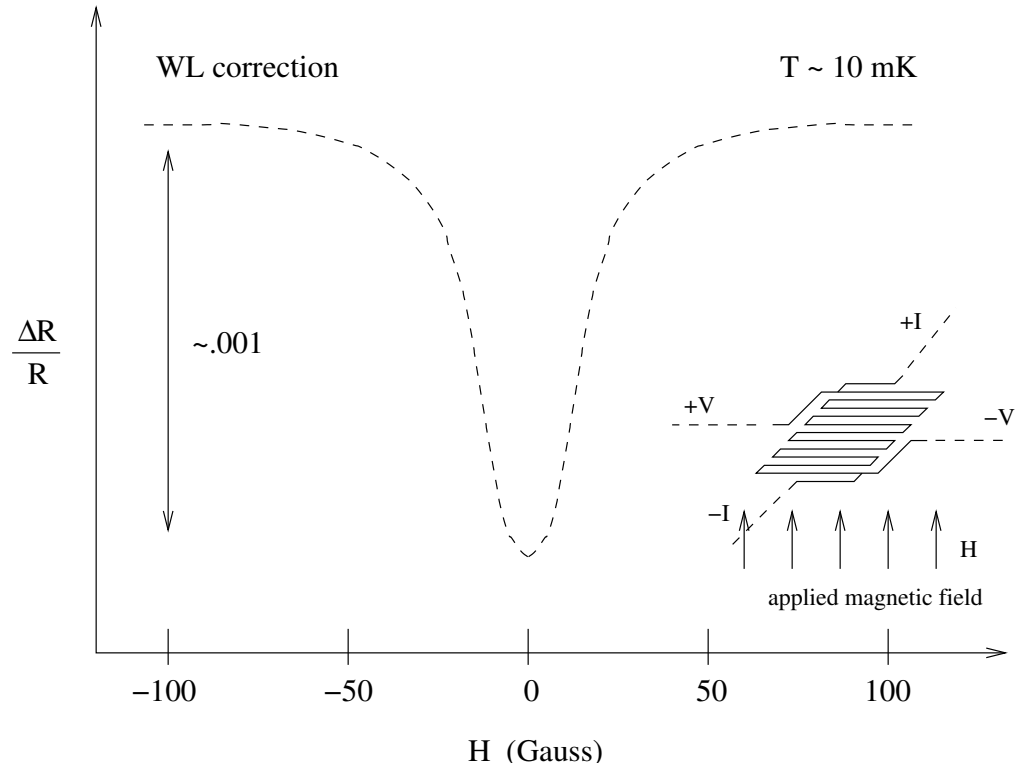

Figure 2.3: Weak localization measurement of the magnetoresistance at millikelvin temperatures. A small correction to the resistance (1 part in 10^3) is seen in the narrow range of applied magnetic field around zero field. The size of the correction is directly proportional to the phase coherence length L_φ. Though less than 0.1% of the total resistance, the dip corresponds to a phase coherence length approaching $\sim 20\,\mu$m in a mm-long meander.

categorized as an *ensemble-average* effect measured over a large number $N = L/L_\varphi$ of uncorrelated phase-coherent segments. For much shorter samples, such that $L \leq L_\varphi$, quantum interference is manifested as reproducible *sample-specific* corrections called universal conductance fluctuations (UCF) [26, 27].

The measurement of these aperiodic fluctuations in the magnetoconductance does not factor directly into our discussion of the persistent current problem. The important point here is that, in the mesoscopic regime, the conductance is not a self-averaging quantity and its behavior is more fully described by the root-mean-square value of the conductance:

$$\sqrt{\langle G^2 \rangle} \simeq C_1 \frac{e^2}{\hbar} \,, \tag{2.11}$$

in addition to the average value $\langle G \rangle$. (Here C_1 is a constant of the order of 1.) In addition, for samples of length L larger than L_φ, this correction is reduced by a factor of $1/\sqrt{N}$, as follows from the addition of random variables. (Here again $N = L/L_\varphi$ is the number of uncorrelated phase-coherent segments.) In Ch. 3, we will discuss an analogous situation in the theoretical formulation of the persistent current.

2.4 Electron-electron interaction

Up to this point, we have assumed that electrons are noninteracting; however, interactions in fact play a significant role in understanding many mesoscopic phenomena. Often invoked to explain the difference between theory and experiment, electron-electron interactions, for example, are thought to be the primary source of decoherence at very low temperatures, leading to a finite L_φ at non-zero temperatures.

For the conductance, the electron-electron interaction modifies the single-particle density of states $\mathcal{N}_0$, leading to a correction:

$$\Delta G_{\mathrm{EEI}} \sim \frac{e^2}{\pi\hbar}\left(\frac{L_T}{L}\right), \tag{2.12}$$

or, in terms of resistance:

$$\frac{\Delta R}{R} = \frac{e^2}{\pi\hbar}\left(\frac{R}{L}\right)\sqrt{\frac{\hbar D}{k_B T}}. \tag{2.13}$$

The new length scale here is the thermal diffusion length $L_T \equiv \sqrt{\hbar D/k_B T}$, where k_B is Boltzmann's constant and T is the temperature. In mesoscopic systems, L_T is the average distance over which dephasing of the electrons occurs due to thermal excitations in the system. As $T \to 0$, the fluctuations in the Coulomb potential disappear and L_T diverges.

Fig. 2.4 illustrates the measurement of the EEI correction to the resistance as a function of temperature, using the same four-terminal setup as for weak localization. At zero applied magnetic field ($H_0 = 0$), the temperature dependence of $\Delta R/R$ may be relatively flat (dotted line), since the EEI and WL corrections can cancel each other out if they are opposite in sign. The EEI correction can be measured separately, however, at finite magnetic field $H_0 \neq 0$ (dashed line), where the weak localization correction is suppressed [28]. By fitting the data to a $T^{-1/2}$ temperature dependence, we can extract the thermal diffusion length L_T and confirm the calculation of the diffusion constant D. Plotted versus $T^{-1/2}$ instead of T, the EEI correction to $\Delta R/R$ naturally appears as a straight line.

Both the thermal diffusion length L_T and the phase coherence length L_φ factor prominently in mesoscopic physics, leading us to introduce in Table 2.2 the concept of *quasi-dimensionality*. For example, a mesoscopic system is considered

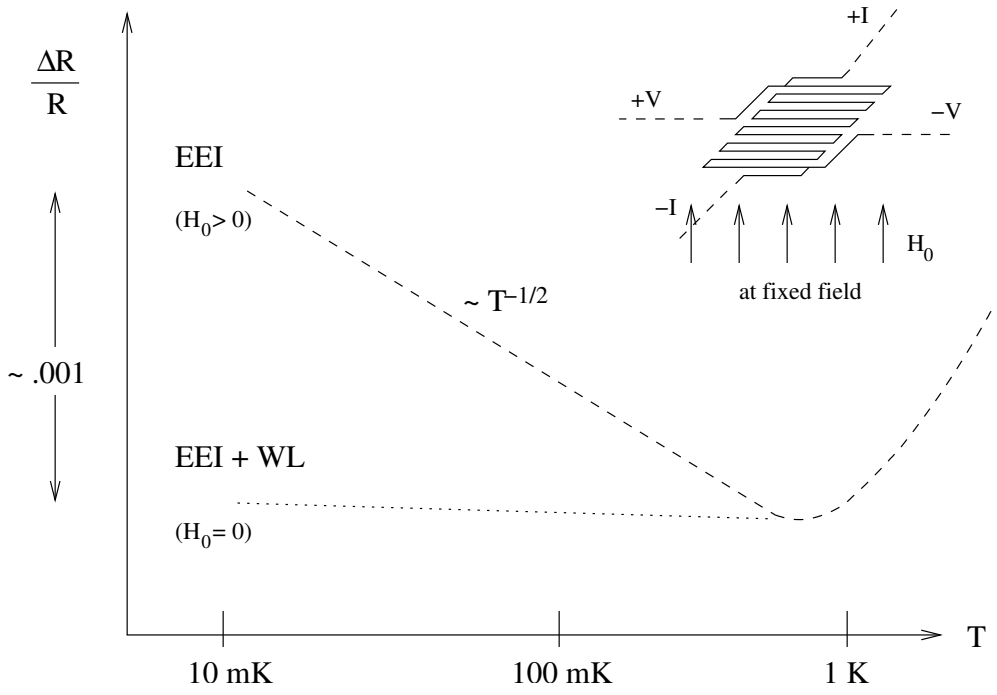

Figure 2.4: Temperature and field dependences of the electron-electron interaction (EEI) correction to the resistance of a quasi-1D wire. For a fixed magnetic field $H_0 \neq 0$, the weak localization (WL) correction observed only near zero field is suppressed, leaving the $T^{-1/2}$ signature temperature dependence of the EEI correction below $\sim$ 1K. (Inset) The same four-terminal current-voltage setup can be used for measurements of both the WL and EEI corrections.

quasi-1D	$L > \{L_\varphi, L_T\} \geq w, t$
quasi-2D	$L, w > \{L_\varphi, L_T\} \geq t$
quasi-3D	$L, w, t > \{L_\varphi, L_T\}$

Table 2.2: Quasi-dimensionality in mesoscopic systems. For mesoscopic systems, the sample's physical dimensions L, w, t must be compared to the phase coherence length L_φ and the thermal diffusion length L_T.

λ_F	Fermi wavelength
ℓ_e	elastic mean free path
L_φ	phase coherence length
L_T	thermal diffusion time
L_H	magnetic phase-breaking length
$L_{\rm so}$	spin-orbit scattering length
L, w, t	sample length, width & thickness

Table 2.3: Summary of definitions of different mesoscopic length scales.

to be "quasi-1D" if the width w and thickness t are less than L_φ and L_T. This differs from the classical dimensionality described in Table 2.1.

To review, we have described an assortment of different length scales that arise in mesoscopics (see Table 2.3). Though derived from transport properties of mesoscopic systems, these length scales also figure strongly into the description of thermodynamic properties and the persistent current problem.

Chapter 3

Recap

In this chapter, we review the present understanding of the persistent current problem – in both theoretical and experimental terms. Following the historical development of the problem [29–31], we introduce the ideal current model, which serves to illustrate the periodic nature and thermodynamic quality of the flux-dependence of the magnetic response of a single, isolated metallic ring. We further divide the problem into separate calculations of the *typical* and the *average* contributions to the persistent current and discuss the competing theoretical explanations [32–39]. We also discuss in detail the handful of previous experimental efforts, distinguishing between measurements on single rings or multiple-ring arrays [2–8]. Our overall focus is on the significant gaps between the wide range of theories and the combined set of existing measurements of the sign, amplitude, and temperature dependence of the persistent current. Regarding the recent publications that have followed our thesis work [10,40], we reserve their discussion for Ch. 6.

3.1 Theoretical Basis

Consider an isolated mesoscopic ring of length L, as shown in Fig. 3.1(a), where the phase coherence length L_φ is long enough that electrons preserve their phase coherence while circumnavigating the ring ($L_\varphi > L$). For any one electron, this implies no change in the quantum state and thus no dissipation – over a time τ_φ. The addition of an Aharonov-Bohm flux Φ through the center [41] introduces a phase factor into the Bloch-like boundary matching condition [42, 43]:

$$\Psi(x+L) = \Psi(x)e^{i\varphi} = \Psi(x)e^{2\pi i(\Phi/\Phi_0)}\,, \tag{3.1}$$

where the additional phase shift is:

$$\varphi = \frac{e}{\hbar}\oint \vec{A}\cdot\vec{dl} \tag{3.2}$$

for a vector potential $\vec{A}$.

One result is that the energy eigenstates as well as all thermodynamic quantities are oscillatory in the applied flux, with a period equal to the fundamental flux quantum h/e. To minimize its free energy F, an isolated ring will support an equilibrium, flux-periodic persistent current:

$$I_p = -\frac{\partial F}{\partial \Phi}\,, \tag{3.3}$$

even in the presence of disorder [29–31]. As noted in Ch. 2, elastic scattering does not change the quantum state of the electron; in fact, an electron here experiences the same random but static potential by moving again and again around the ring, in an effectively periodic situation in a unit cell of size L. In this analogy, the energy levels of the ring as a function of Φ correspond to traditional 1D Bloch levels [11], as shown in Fig. 3.1(b).

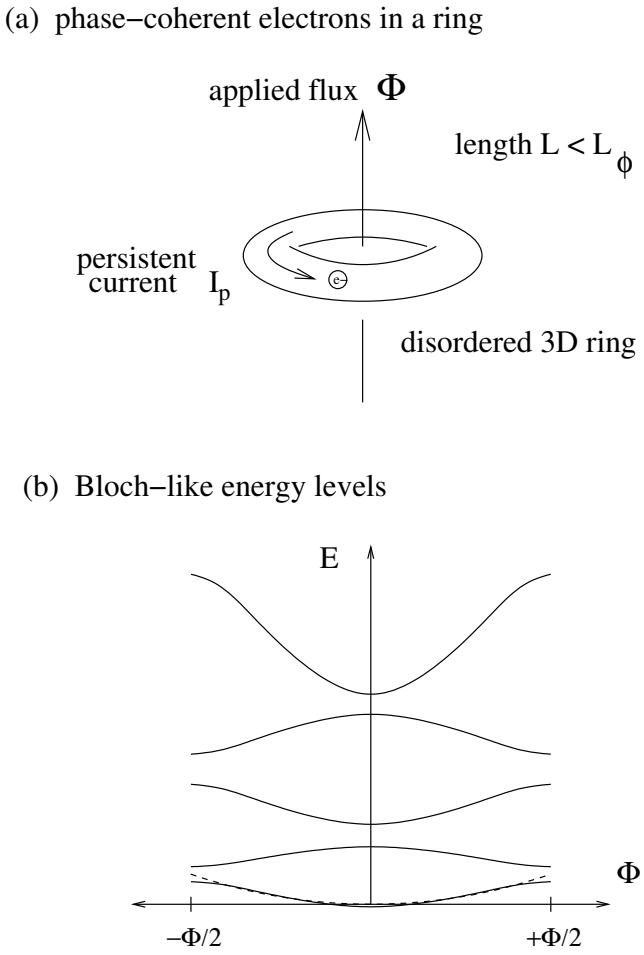

Figure 3.1: The analogy to Bloch-like boundary conditions for phase coherent electrons in a disordered metallic ring. (a) The presence of an Aharonov-Bohm flux Φ adds a periodic component $\exp[2\pi i(\Phi/\Phi_0)]$ to the phase of extended electron wavefunctions, resulting in (b) energy eigenstates that are periodic in flux, in an analogy to traditional 1D Bloch levels.

Nondecaying currents and flux quantization effects are already well-known from studies of superconducting rings [17]. Though outwardly similar, the persistent current in a normal-conducting ring is decidedly different. For one, the superconducting persistent current is a dynamical effect characterized by a much larger current that does not oscillate but rather increases monotonically (and in steps) with the flux, forming a metastable state. In a normal ring, the persistent current is small but finite, oscillates strictly with the applied flux, and is an equilibrium thermodynamic effect. Moreover, in a superconducting ring, the superconducting state is described by a single macroscopic wavefunction that retains its phase coherence over arbitrarily large lengths [11]; the phase itself is a macroscopic commutating variable. In a normal ring, each electron wavefunction has its own well-defined phase φ; after traveling a finite length L_φ, the electron accumulates a change of order $\Delta\varphi \approx 2\pi$ and loses phase coherence. But, it is the collective behavior of these individual electron states that supports the equilibrium persistent current in a phase-coherent normal-conducting ring.

For an ensemble of normal rings, the fundamental harmonic of this current (with flux periodicity h/e) is strongly suppressed, whereas the next harmonic (with flux periodicity $h/2e$) survives due to the contribution of time-reversed paths of the electron [32, 33]. In addition, the h/e current may be either paramagnetic or diamagnetic in sign, depending on the microscopic details of the disorder of each ring; the $h/2e$ current is believed to always be the same sign. Following this distinction, we separate the persistent current problem into two parts: as with our discussion of sample-to-sample fluctuations in the conductance $\sqrt{\langle G^2 \rangle}$ from the previous chapter, we distinguish between a typical, root-mean-square current $\sqrt{\langle I^2 \rangle}$ and an ensemble averaged current $\langle I \rangle$. Unless otherwise

stated, all calculations presented are for disordered metallic systems, where $\langle \cdots \rangle$ represents an average taken over the ensemble of disorder configurations.

3.1.1 The Typical Current

For a single ring, the relevant concept is the *typical current*. In a mesoscopic sample at low enough temperatures, sample-specific fluctuations in the actual distribution of electron energy levels near the Fermi level, rather than the mean level spacing Δ, determine the thermodynamic properties [19]. Subsequently, correlations in the energy spectrum of the ring can lead to a nonvanishing variance for the current, even though the mean itself may be zero. Thus:

$$\langle (\delta I^2) \rangle = \langle I^2 \rangle - \langle I \rangle^2 \neq 0 \tag{3.4}$$

In the literature on persistent current, the typical current typically refers to the root-mean-square amplitude of $\sqrt{\langle I^2 \rangle}$.

The sign of a random quantity with zero mean can, of course, be either positive or negative. For the case of the typical current, which has a dominant period of h/e, we refer to the sign of the response as either paramagnetic or diamagnetic near zero magnetic field. For clarity, consider Fig. 3.2. The signal measured by a pickup loop from a single ring is plotted here as an odd, oscillatory function of the applied magnetic field. The period shown corresponds to one h/e flux quantum through the area of the ring. A positive (paramagnetic) signal is defined as increasing positively from zero with the applied magnetic field, as shown. A negative (diamagnetic) signal would be flipped over the x-axis, starting at zero and becoming more negative with the field. For the specific response from any one given ring, either sign is equally probable *a priori*.

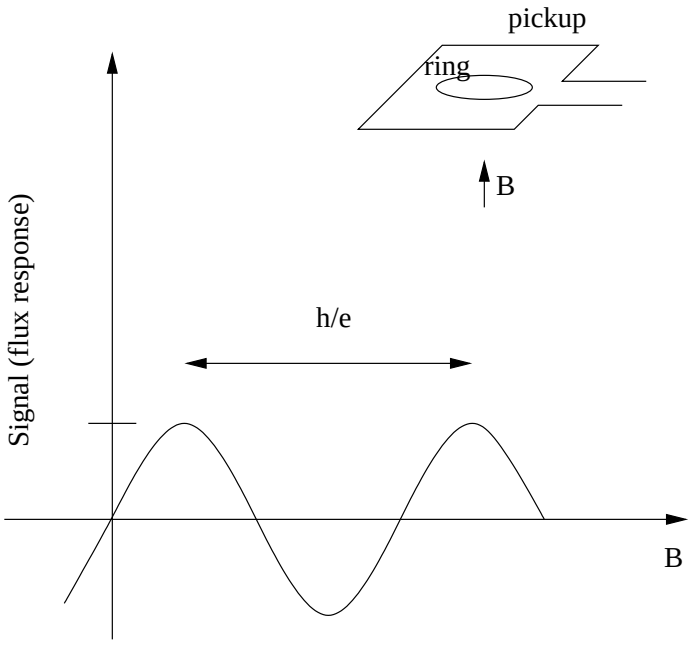

Figure 3.2: The h/e-periodic component of the typical current in a single normal-metal ring. The inset depicts the measurement of the magnetic response due to the persistent current in an isolated mesoscopic ring. The flux signal coupled to the detector coil is shown in the graph as oscillating with the applied magnetic field, with a period equal to one h/e flux quantum through the area of the ring. The sign of the current is paramagnetic, shown at zero magnetic field as increasing with applied field. A diamagnetic current conversely would be shown as decreasing.

The amplitude of the typical current shown in the figure is related in theory to the Thouless energy E_c, according to:

$$\sqrt{\langle I^2 \rangle} \sim \frac{eE_c}{\hbar}\,, \tag{3.5}$$

suggesting that the amplitude (and also temperature dependence) of the effect is governed by energy correlations on the scale of E_c [34]. This result has been obtained both analytically and numerically, for strictly 1D samples and for 3D samples, in the presence of elastic scattering [32–34]. Given the ideal current in the ballistic regime as $I_0 = ev_F/L$, we can also interpret Eq. 3.5 as a reduction of I_0 by a multiplicative factor (l_e/L) due to disorder. Here the independent electron picture is assumed; however, including the electron-electron interaction through a correction to the density of states – as seen in studies of other mesoscopic phenomena [28] – does not change the typical current result [44, 45].

The dominant period of the magnetic response due to the typical current is h/e as shown in Fig. 3.2, but $h/2e$ or higher order h/me-periodic responses are not ruled out; however, these additional currents of $\sqrt{\langle I_m^2 \rangle}$ for $m = 2, 3, 4, \ldots$ are attenuated by an extra factor of $m^{3/2}$. The harmonics of the typical current are given by the following formula (adapted from Ref. [15]):

$$\langle I_m^2 \rangle = 4 \times \frac{96}{(2\pi)^2 m^3} \left(\frac{eE_c}{\hbar}\right)^2 \left[1 + \frac{m}{2}\frac{L}{L_\varphi} + \frac{m^2}{3}\left(\frac{L}{L_\varphi}\right)^2\right] e^{-mL/L_\varphi} \tag{3.6}$$

where the factor of 4 accounts for the electron spin degeneracy. The $h/2e$ component of the typical current, for example, is almost three times smaller than the h/e component. For this reason, most theoretical and experimental efforts have focused solely on the h/e-periodic contribution to the typical current.

In the zero-temperature limit of $(L/L_\varphi) \to 0$, we find:

$$\langle I_m^2 \rangle = \frac{96}{\pi^2 m^3} \left(\frac{eE_c}{\hbar}\right)^2, \tag{3.7}$$

such that the typical current is proportional to E_c. From here follows the commonly-quoted result of

$$\sqrt{\langle I_1^2 \rangle} = (2 \times 1.56)\left(\frac{eE_c}{\hbar}\right) \tag{3.8}$$

for the h/e-periodic current ($m = 1$), where again the factor of 2 accounts for the spin. For more accurate comparisons to experimental results, as in Ch.6, we must include the other terms in (L/L_φ).

3.1.2 The Average Current

The challenge of measuring even the dominant h/e contribution to the typical current in a single ring touches on another important point: for an ensemble of N rings, the total current response should only grow as $\sqrt{N}$, leading to an overall reduction of $1/\sqrt{N}$ in the current per ring. In the multiple-ring case, however, a completely different contribution to the persistent current – an average over the ensemble of rings – comes into play.

In Fig. 3.3, we illustrate the concept of the *average current*. As opposed to the response of a single ring in Fig.3.2, here the overall signal response is measured from an array of N independent rings. The typical current contribution $\sqrt{\langle I^2 \rangle}$ from this array is negligibly small, but there now appears an ensemble-average contribution $\langle I \rangle$, with a dominant flux-period of $h/2e$ instead of h/e. This ensemble-average current corresponds in theory to the average current calculated over the disorder ensemble, i.e. over the set of configurations of the disorder potential in one ring but representing the microscopic differences present in a large array of nominally similar rings. In contrast, we note that the disappearance of the h/e response is dependent on the inherent random sign of the

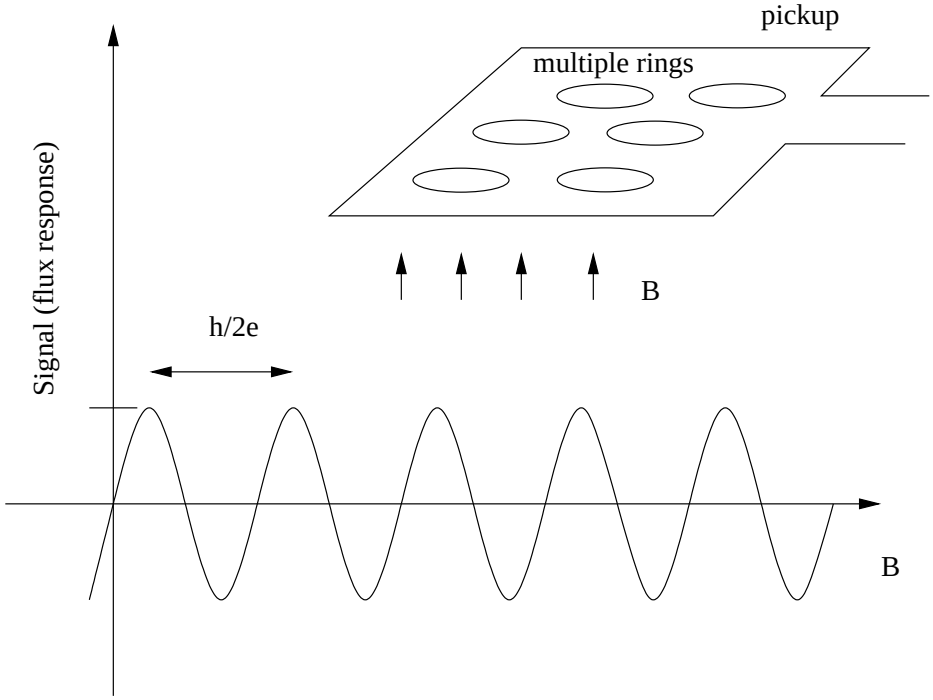

Figure 3.3: The $h/2e$-periodic component of the average current in an array of normal-metal rings. The inset depicts a measurement of the net magnetic response of an array of N independent rings. The flux signal coupled to the detector coil is shown in the graph as oscillating with the applied magnetic field, with a faster period equal to $\frac{1}{2}$ of an h/e flux quantum, or $h/2e$, through the average area of the rings. For large N, we associate this $h/2e$-periodic net response with the average current $\langle I_2 \rangle$ calculated over the disorder ensemble.

typical current from each ring, and not from systematic fabrication differences between rings.

The most striking feature of the ensemble-average current is the dominant $h/2e$ flux period of the response. Also referred to as "period doubling", this effect has been demonstrated both numerically and analytically under differing conditions. We feel however that a simpler explanation follows from an almost exact analogy to the weak localization correction. As described in the previous chapter, there exists a a quantum interference contribution from coherent backscattering; in a ring, these pairs of equal but time-reversed paths effectively enclose twice the area and are thus sensitive to half as much flux, or $h/2e$.

The calculation of the average current for noninteracting electrons depends upon the choice of statistical ensemble [37, 39]. Using the grand canonical ensemble, where the chemical potential μ is kept fixed and the number of electrons N_e is allowed to vary with flux Φ, the average current is proportional to e^{-L/ℓ_e} and practically zero [34]. In the canonical ensemble, the number of electrons N_e in each member of the disorder ensemble is fixed and thus flux independent; however, by expanding the sample-to-sample variations in the chemical potential as $\mu = \langle\mu\rangle + \delta\mu(\Phi)$, we can express the average current as:

$$\langle I\rangle \simeq -\frac{\Delta}{2}\frac{\partial}{\partial\phi}\langle(\delta N_e)^2\rangle\,, \tag{3.9}$$

where the fluctuations of the particle number $\langle(\delta N_e)^2\rangle$ are calculated at a fixed chemical potential $\mu = \langle\mu\rangle$. The above equivalence relationship leads to a non-vanishing $h/2e$-periodic average current, with a finite amplitude:

$$\langle I_2\rangle = \frac{4}{\pi}\left(\frac{e\Delta}{\hbar}\right) \tag{3.10}$$

and a strictly paramagnetic sign [39].

For the typical current calculation, we mentioned above that including the electron-electron interaction [28] has little effect on the result; the same is not true for the average current, with significant implications. Here one important theory utilizes the electron-electron interaction as a source of fluctuations to provide the pairings responsible for the $h/2e$ period, in the absence of an external field [35]. (In the nonequilibrium case of weak localization, the applied electric field can produce electron-hole pairs that lead to the pairing effect. In the equilibrium case of persistent currents in isolated rings, no external field is present.) The resulting prediction is:

$$\langle I_2 \rangle = \mu^* \frac{8}{3\pi} \left(\frac{e v_F}{L} \right) \frac{l_e}{L} \,, \tag{3.11}$$

where μ^* is a dimensionless coupling constant. In addition, the temperature dependence is given by $\exp(-k_B T/3E_c)$. Calculation of the coupling constant is nontrivial, with the most accurate estimates yielding a range:

$$\langle I_2 \rangle = [0.1 - 0.2] \left(\frac{e E_c}{\hbar} \right) \tag{3.12}$$

for normal metals [35, 36, 46]. The end result is the enhancement of the average current by two to three orders of magnitude over the noninteracting case, depending on the difference between E_c and Δ. The sign is coincidentally also paramagnetic, here following from the use of a repulsive interaction in calculating the coupling constant μ^*.

Table 3.1 summarizes the major theories for the ensemble-average current $I_{\rm av}$ as well as the typical current $I_{\rm typ}$, distinguishing between noninteracting (i.e. single-electron picture) and interacting (i.e. collective response due to Coulomb interaction) calculations. We list the dominant flux-period, the sign near zero field, the maximum amplitude, and the temperature dependence for each calcu-

Theory	$I_{\rm typ} = \sqrt{\langle I^2 \rangle}$				$I_{\rm av} = \langle I \rangle$			
	per	sign	ampl	temp	per	sign	ampl	temp
g.c.e.	h/e	$\pm$	$\sim \frac{eE_c}{\hbar}$	$e^{-\sqrt{k_BT/E_c}}$	h/e	$\pm$	$\to 0$	—
c.e.	h/e	$\pm$	$\sim \frac{eE_c}{\hbar}$	$e^{-\sqrt{k_BT/E_c}}$	$h/2e$	para	$\frac{4}{\pi}\frac{e\Delta}{\hbar}$	$e^{-\sqrt{k_BT/E_c}}$
e-e int	*No additional contribution.*				$h/2e$	para	$[.1 - .2]\,\frac{eE_c}{\hbar}$	$e^{-k_BT/3E_c}$

Table 3.1: Comparison of major theories of the typical current $\sqrt{\langle I^2 \rangle}$ and the average current $\langle I \rangle$ per ring, according to type of statistical ensemble used (grand canonical or canonical) and if electron-electron interactions are included. We list the dominant flux-period, the sign near zero field, the maximum amplitude, and the temperature dependence for each calculation. See text for details.

lation. For the typical current, the results are unchanged if calculated using the canonical or grand canonical ensemble, or if electron-electron interactions are included. In all cases, the typical current has a dominant h/e harmonic, with either a paramagnetic or diamagnetic sign. For the average current, however, the difference made by including e-e interactions is evident in a comparison of the energy scales associated with each theory. In a disordered metallic system, this difference between the mean level spacing Δ and the Thouless energy E_c can be as large as three orders of magnitude. Without interactions, the ensemble-average $h/2e$ current only survives in the canonical ensemble and not the grand canonical ensemble [37–39]. Though both predictions feature an $h/2e$-periodic current with paramagnetic sign, the significant differences in amplitude and temperature dependence indicate that the theoretical picture of the average current remains unclear, despite a decade of work.

3.2 Experimental Findings

Nanoampere-sized h/e- or $h/2e$-periodic currents have been separately observed in a few experiments: the h/e current has been measured in single Au rings [4] and in a GaAs-AlGaAs ring [5], while the $h/2e$ current has been measured in multiple-ring arrays of 10^7 Cu rings [2] and 10^5 GaAs-AlGaAs rings [7], where the h/e response was not observable. Table 3.2 summarizes the results for each experiment, listing the dominant flux-period of the response, the amplitude of the current at lowest temperatures, the sign near zero field, and the reported exponential temperature dependence and characteristic temperature T_0, if any. We describe each experiment in detail below, beginning with those that utilize diffusive metallic rings.

In the first published experiment on an array of 10^7 copper loops [2], each of perimeter $L = 2.2\,\mu$m and with $l_e \approx 30\,$nm, the average current exhibited a flux-periodicity of $h/2e$, not h/e. Though existing analytical [32] and numerical [33] theories could demonstrate period-halving for the ensemble-averaged current, the amplitudes predicted for this nonvanishing second moment $\langle I_2 \rangle$ were two orders of magnitude smaller than the measured value of 0.4 nA per ring, extrapolated to zero temperature. In terms of the perimeter L of the ring, this corresponds to $0.0035\, ev_F/L \simeq 0.26\,(ev_F/L)(l_e/L)$ per ring, using the standard value $v_F = 1.57 \times 10^6\,$m/s for the Fermi velocity in copper. As pointed out shortly thereafter [35], the electron-electron interaction can significantly enhance the average current, yielding a more agreeable prediction of $\mu^*(8/3\pi)(ev_F/L)(l_e/L)$, where μ^* is a dimensionless coupling constant. The initial estimate of $\mu^* = 0.3$ gives a good match to experiment, although higher-order logarithmic corrections reduce this value by a factor of five [36]. We note

Experiments			$I_{\text{typical}} \equiv \sqrt{\langle I_n^2 \rangle}$				$I_{\text{average}} \equiv \langle I_n \rangle$			
N	system	[Ref]	per	sign	ampl	temp	per	sign	ampl	temp
1	GaAs	[5]	$\frac{h}{e}$	– ? –	$0.77\,\frac{ev_F}{L}$	– ? –	*Not measured.*			
1	Au	[4]	$\frac{h}{e}$	– ? –	$0.17\,\frac{ev_F}{L}$	– ? –				
1	Au	[4]	$\frac{h}{e}$	para	$1.0\,\frac{ev_F}{L}$	$e^{-\sqrt{\frac{T}{4.8}}}$				
1	Au	[4]	$\frac{h}{e}$	para	$0.21\,\frac{ev_F}{L}$	$e^{-\sqrt{\frac{T}{4.8}}}$				
10^5	GaAs	[7]	*Not measured.*				$\frac{h}{2e}$	dia	$2.24\,\frac{eE_c}{\hbar}$	$e^{-\frac{T}{190}}$
10^7	Cu	[2]					$\frac{h}{2e}$	– ? –	$0.77\,\frac{eE_c}{\hbar}$	$e^{-\frac{T}{80}}$

Table 3.2: The experiments: four different measurements of the typical or the average persistent current. For each sample, we list the dominant flux-period of the response, the sign near zero field, the amplitude of the current at lowest temperatures, and the reported exponential temperature dependence and characteristic temperature T_0, if any. The average current, with $h/2e$ period, is seen only in multiple-ring arrays, as expected. The typical current, dominated by the h/e-periodic signal, is correspondingly the focus of the single-ring measurements. For comparison, we present the current amplitudes in terms of either the respective ballistic (ev_F/L) or diffusive ($eE_c/\hbar$) current scales for each system.

here that the screened Coulomb potential is repulsive ($\mu^* > 0$), which implies a paramagnetic sign for this current. In addition, this interaction calculation also appears to give the correct temperature dependence $\sim \exp[-T/3T_1]$ for the data from the 10^7 Cu rings, given the estimate of $T_1 \approx 25\,\mathrm{mK}$ for the Thouless scale $E_c \sim k_B T_1$ of correlations of energy levels in the rings. Incidentally, the temperature dependence calculated by Ambegaokar and Eckern [35] is given in the paper by Levy [3] as $\exp(-\pi^2 T/3E_c)$ for $T \sim E_c$ and as $\exp(-2\pi L/L_T)$ for higher temperatures. Since Levy uses a different definition of E_c as $\pi^2\hbar/DL^2$ and L_T as $\pi\sqrt{\hbar D/k_B T}$, we translate into the approximations usually cited, i.e. $\exp(-T/3E_c)$ and $\exp(-2L/L_T) \sim \exp(-\sqrt{4T/E_c})$. Using the standard definition $E_c \equiv \hbar D/L^2$ from Ch. 2, we point out that the current is of order $eE_c/\hbar \sim (ev_F/L)(l_e/L)$. Overall, the Thouless energy thus seems to play a role in both the amplitude and temperature dependence of the ensemble-averaged $h/2e$ persistent current, as measured in in this multiple-ring experiment.

Instead of measuring an average current in a multiple-ring array, a more sensitive experiment on a single ring investigates the typical current, denoted by the two-point correlator $\langle I_m^2 \rangle$ of the variations of the persistent current with flux. The first moment I_1 of this typical current displays the conventional flux-period of h/e. In the experiment on single metallic rings [4], using three different gold loops with perimeters 7.5, 8.0, and 12.6 μm and $l_e \approx 70\,\mathrm{nm}$, the h/e-periodic signals of $30 \pm 15, 6 \pm 2$, and $3 \pm 2\,\mathrm{nA}$, respectively, measured at the base temperature of 4.5 mK, correspond to a persistent current $\simeq (0.3 - 2.0)\, ev_F/L$, given $v_F = 1.4 \times 10^6\,\mathrm{m/s}$ in gold. Note that, in terms of ev_F/L, the h/e typical currents in these single Au rings are more than two orders of magnitude larger than the value per ring given above for the $h/2e$ average current in an array

of 10^7 Cu rings [2]. The single ring typical currents are also two orders larger than the scale $\sim eE_c/\hbar \approx 10^{-2}\, ev_F/L$ predicted for noninteracting electrons in diffusive systems; here, the effect of electron-electron interactions remains unclear as to any enhancement [44,45]. The h/e data fit an $\sim \exp[-T^{1/2}]$ as well as an $\sim \exp[-T]$ temperature dependence, with an apparent saturation below the estimated $E_c \approx 10\,\mathrm{mK}$. Additionally, in this single-ring measurement, the h/e signal dominates any $h/2e$ contribution associated with the second moment I_2 of the current. Despite many theoretical attempts, the large amplitudes of the typical currents measured in single normal-metal rings still remain unexplained.

Persistent currents have also been measured in both single and multiple semiconductor rings, in which the electron motion is nearly ballistic. In the experiment on a single $L \approx 8.5\,\mu\mathrm{m}$ ring patterned in a high-mobility GaAs/AlGaAs heterostructure [5,6], the mean value of $4 \pm 2\,\mathrm{nA}$ measured for the h/e typical current at 15 mK agrees with the expectation of $ev_F/L \approx 5\,\mathrm{nA}$ per channel, using a separately measured value of $v_F = 2.6 \times 10^5\,\mathrm{m/s}$. Note that the form ev_F/L does not contain the factor (l_e/L) attributed to disorder; however, the value measured in this ballistic ring is comparable to the h/e typical currents in single diffusive rings [4] described above. In a more recent experiment on an array of 10^5 isolated GaAs/AlGaAs rings coupled to a microresonator [7,8], the $h/2e$-periodic oscillations observed in the complex magnetoconductance correspond to an average persistent current of order $\sim eE_c/\hbar$ per ring, using their slightly different definition of $E_c \equiv 2\pi\hbar D/L^2 \approx 200\,\mathrm{mK}$. Again, this measurement of the $h/2e$ current in an array of nearly ballistic GaAs/AlGaAs rings parallels the result from the array of diffusive Cu rings [2], with also no discernible h/e signal.

Regarding the sign of the persistent current, we note in Table 3.2 that the

measurement of the sign of the response is reported in only two experiments [4,7], and in only three of the six samples overall [3]. Considering that the sign of the typical current is defined to be either positive or negative with equal probability [34], the uniform observation of a paramagnetic sign in only two different samples in Ref. [4] is, by itself, not statistically significant. In the absence of any other measurements, however, the predicted randomness in sign for $I_{\rm typ}$ has yet to be demonstrated explicitly. The sole measurement of the sign of the average current $I_{\rm av}$ yields a diamagnetic response for an array of 10^5 GaAs rings [7], in striking disagreement with the paramagnetic prediction of almost all theories [35, 39]. For both the typical and average currents, this suggests that the sign is still an open question for further investigation.

Regarding the amplitude of the persistent current, all of the reported amplitudes are remarkably 10–100 times larger than theoretically expected, except for the one result in a single GaAs ring [5]. For comparison, the values for the amplitudes of either current are given in Table 3.2 in terms of one of three descending energy scales: ev_F/L for free electrons at the Fermi level, $eE_c/\hbar$ corresponding to the Thouless scale E_c, or $e\Delta/\hbar$ based on the mean level spacing Δ. For the typical current, the results from the two experiments are all of order $\sim ev_F/L$; however, a maximum value of only $\sqrt{\frac{96}{\pi^2}}\, eE_c/\hbar$ at $T = 0$, i.e. up to two orders of magnitude smaller than ev_F/L, is predicted for the case of the three gold rings in the diffusive regime. For the average current, the two experiments yield results of order $\sim eE_c/\hbar$, also up to two orders of magnitude larger than the predictions of $\sim e\Delta/\hbar$ for the diffusive case and $\sim e\sqrt{E_c\Delta}/\hbar$ for the ballistic case. As opposed to obtaining an unusually small result, the observation of an anomalously large response cannot be so easily attributed to random or systematic errors in

a measurement. For three of the four original experiments, then, the amplitude of the persistent current is also an open question.

Finally, the physical origin of the temperature dependence of either the typical or the average current is perhaps the most difficult to ascertain. For example, Table 3.2 gives the reported fits to $e^{-\sqrt{T/T_0}}$ for the typical current, but to e^{-T/T_0} for the average current; in reality, this distinction is almost arbitrary. For one, on the experimental side, the range of temperatures for which data is available is limited to $T < 200\,\mathrm{mK}$; accordingly both of the exponential forms e^{-T/T_0} and $e^{-\sqrt{T/T_0}}$ fit any of the data sets, as shown explicitly for samples in Ref. [4]. On the theoretical side, most results for the temperature dependence are not strictly simple exponential dependences, inferred from the corresponding energy scale of the predicted amplitude. In the e-e interaction calculation [35], for example, the initial result is in fact an unwieldy combination of algebraic and exponential dependences, which reduces to the much simpler form of $e^{-T/3T_1}$ only within a specific range of intermediate temperatures. It is also unclear if an additional factor of $e^{-L/L_\varphi(T)}$ is warranted in any formulation, since the value of the phase coherence length L_φ is usually fixed and assumed to be temperature independent at these low temperatures. Overall, the specific temperature dependence of the persistent current has not been uniquely identified for any of the possible cases.

In addition to these specific disagreements with theory for the sign, the amplitude, or the temperature dependence, the four experiments are completely independent of each other and alone are insufficient for resolving our understanding of the persistent current. As shown in Table 3.2, the results are split not only between single rings and multiple ring arrays, but also between metallic and semiconducting systems. As with other mesoscopic phenomena, the persis-

tent current problem changes if transport is characterized as ballistic rather than diffusive, in contrast to macroscopic thermodynamic properties that are strictly independent of disorder [19]. In addition, not only does one experiment not corroborate another, but theoretical work – on this singular problem of the persistent current – is consequently also divided into two separate and, at times, conflicting groups of predictions for either the typical or the average current contributions. The serious disagreement between theory and experiment by itself seems to warrant new measurements for confirmation; we can add that no experiment has additionally allowed for direct comparisons between the two contributions i.e. focusing on both the h/e- and $h/2e$-periodic responses of the typical and average current contributions in the same ensemble.

As a final note, in comparing the experiments and theories of others, we have uniformly used the most common definition of the Thouless energy $E_c \equiv \hbar D/L^2$, even if the original references themselves utilize other variants such as $\pi\hbar D/L^2$, $2\pi\hbar D/L^2 = hD/L^2$, or even $\pi\hbar D/(2L)^2$. This confusion over the empirical definition of E_c extends to most of the literature in mesoscopic physics – past or present. The case of persistent currents, however, seems to suggest this particular definition: if $E_c \equiv \hbar D/L^2$ for a ring of length L, then an electron moving diffusively around the ring in a time $\tau_D = L^2/D$ carries a current of e/τ_D, or equivalently $eE_c/\hbar$. Another, more general argument concerns the description of the thermal diffusion of electrons in small systems: the choice of $E_c = \hbar D/L^2$ treats the equivalent conditions for energy scale $k_B T < E_c$ and length scale $L_T > L$ in a consistent fashion.

Chapter 4

Proposal

In dissecting the persistent current problem in Ch. 3, we have distinguished between two formally different concepts: the typical current associated with sample-specific fluctuations about the average, and the ensemble-averaged current itself – neither of which could be expected in a metallic ring of macroscopic dimensions. The measurements themselves are similarly divided between the dominant h/e oscillations in individual rings and the $h/2e$ signal seen in large arrays of rings. Despite these distinctions, the central question at hand regarding persistent currents remains the anomalous sign and magnitude of the periodic magnetic response of micron-sized rings, for which both experimental data as well as theoretical understanding are in short supply.

As the primary objective of this thesis, we propose a new experiment investigating the typical and average contributions together, through a unique measurement of both the h/e- and $h/2e$-periodic components of the persistent current in a single sample of mesoscopic rings. In this prefatory Chapter, we formally outline our proposal, beginning with the conceptual basis behind this novel undertaking. In conjunction, we identify essential methods and techniques

– regarding detector design, sample fabrication, and data analysis – that help to distinguish our experiment from previous efforts. Referring back to the unresolved issues of Ch. 3, we introduce specific goals for this thesis and motivate the original contributions to follow – setting the stage for the presentation and discussion of the experiment itself in Chs. 5 and 6.

4.1 Concept

The idea of measuring both contributions in the same array draws upon the statistical nature of the persistent current problem, as described by the number of rings N in the sample. In theory, for very large N approaching the limit of $N \to \infty$, the ensemble-average calculation alone is considered; only for much smaller sets, closer to $N = 1$, are statistical fluctuations in individual rings deemed relevant. For any size array, however, the total response by definition contains both contributions:

$$\sum_{n=1}^{N} I_n = \left\{ I_{\text{typ}} \times \sqrt{N} \right\} \; + \; \left\{ I_{\text{av}} \times N \right\} \tag{4.1}$$

where I_{typ} and I_{av} represent the predicted current amplitudes for the typical and average contributions, respectively. The factor of $\sqrt{N}$, as opposed to N, shown in the fluctuation current contribution follows from the statistics of adding random variables. Dividing both sides of Eq. (4.1) by N, we note that the estimated typical current per ring decreases as $1/\sqrt{N}$ for increasing N, leaving only significant contributions from the constant ensemble-average value per ring.

This conceptual dependence on ensemble number N is borne out by experiment. Consider Fig. 4.1, which illustrates the gap between single-ring and multiple-ring experiments; in contrast, we propose to measure precisely $N = 30$

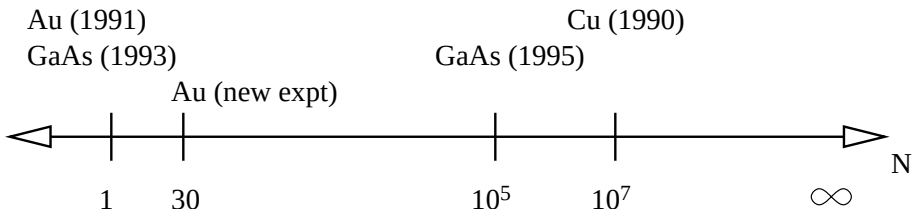

Figure 4.1: Comparison of the number of rings N in all experimental ensembles, including the new effort proposed here. Our choice of a finite number $N = 30$ is of course larger than $N = 1$ as in the single-ring studies, but still distant from the thermodynamic limit of $N \to \infty$ suggested by the two larger ensembles.

rings in this new experiment [47]. Though larger of course than $N = 1$ in the single ring studies [4,5], our choice for N is nonetheless far from the thermodynamic limit of $N \to \infty$ suggested by the two larger ensembles [2,7], thus preserving the sample-specific contributions of the typical current. At the heart of our thesis proposal is the postulate that an array comprised of an intermediate number of rings, such that $1 < N << \infty$, should demonstrate both the typical and the average contributions to the persistent current, if N is not too large.

The total response can also be divided according to the different flux-periods of oscillation. In terms of integral flux-quanta $\phi_p \equiv h/pe$, where $\phi_1 = h/e$ and $\phi_2 = h/2e$, the total response demonstrates multiple flux components:

$$\sum_p I_p \sin\left(2\pi\frac{\phi}{\phi_p}\right) = I_{1T}\sin\left(2\pi\frac{\phi}{\phi_1}\right) + I_{2T}\sin\left(2\pi\frac{\phi}{\phi_2}\right) + \ldots \qquad (4.2)$$

where I_{1T} and I_{2T} are the total h/e- and $h/2e$-periodic components, respectively, from the entire ring array. Though the given functional form of $I_p \sin\theta$ is commonly prescribed, the persistent current in general must only be periodic in flux. As discussed in Ch. 3, the typical current contribution can contain many

different flux-periods, though the h/e component is predominant. On the other hand, multiple-ring experiments suggest that the average current only has a significant $h/2e$ component. Based on these observations, we propose to consider separately the sample-specific fluctuations in the h/e-periodic signal, apart from the ensemble-average contribution to the $h/2e$ response.

4.2 Methodology

Besides these conceptual underpinnings, our new experiment also depends specifically on the details of measurement, as presented here. Most importantly, our proposal features a specialized inductance design for the SQUID-based measurement setup in order to achieve unique sensitivity to both the typical and average contributions, as well as to the overall flux signal. We also stress the fabrication of appropriate control samples for our experiment, in addition to the array of rings. Finally, in anticipation of the measurements, we consider the methods of data analysis needed to distinguish the h/e oscillations from the overlapping $h/2e$ signals. Although some of the techniques presented here are not unique to this thesis, the demonstration of their implementation or execution is critical to our thesis objective and constitutes the bulk of our efforts.

4.2.1 Measurement Design

For our experiment, the innovative design of the measurement setup is as important as our proposed choice for the number of rings. If we are to measure only $N = 30$ metallic rings as proposed, instead of 10^7 as in a previous experiment [2], our sensitivity must be significantly improved. Figure 4.2 shows three different

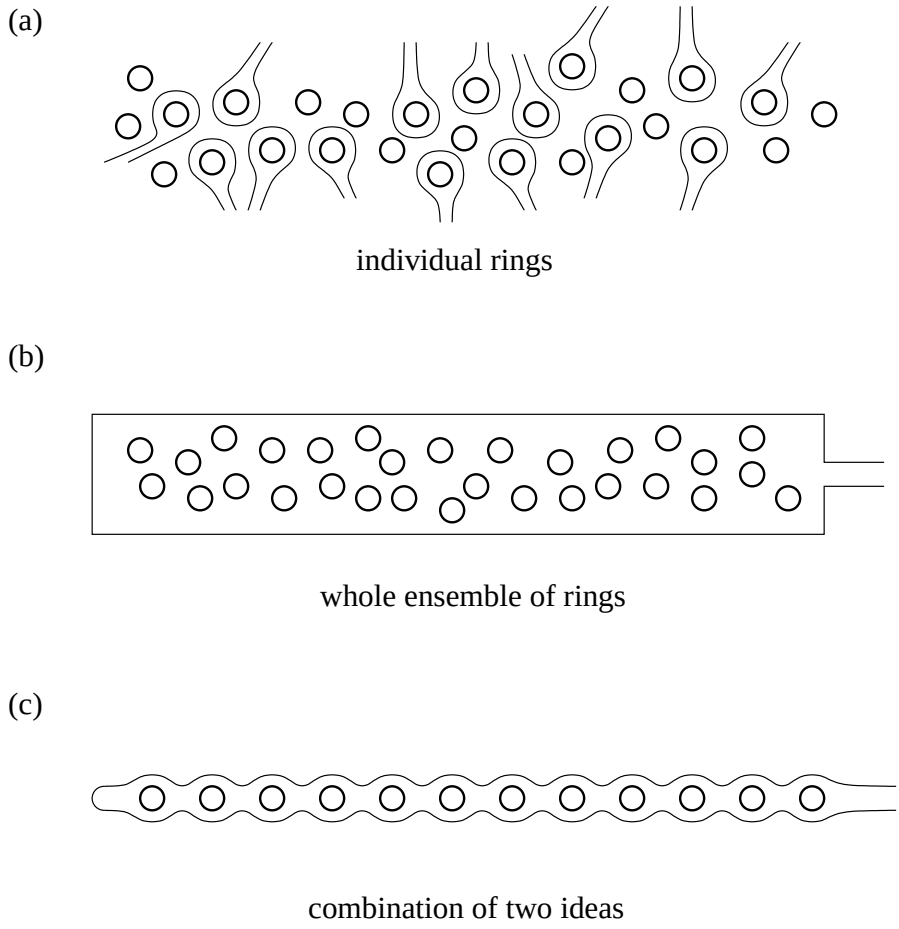

Figure 4.2: Proposal for combining measurement sensitivity to both the typical and the average contributions. In these three schemes for measuring the persistent current, we illustrate (a) a flux-sensitivity to individual rings, (b) a flux-sensitivity to the whole ensemble, and (c) our proposal for a combination of the two, featuring a uniquely-shaped pickup coil aligned with a linear array of rings. Factoring in our statistical choice for the ensemble number N, we propose to investigate both the sample-specific fluctuations as well as the ensemble-average contribution from the same array of $N = 30$ rings.

schemes for measuring persistent currents using a SQUID pickup coil, as seen from above. In Fig. 4.2(a), we show an assortment of small pickup loops, each coupled to a single small ring, for sensitivity to sample-specific fluctuations in each. In contrast, we depict in Fig. 4.2(b) a much larger pickup loop, like that used in a previous experiment [2], now encircling all of the rings for overall sensitivity to the ensemble-average current, but not to the typical current. Fig. 4.2(c) illustrates the unique design of our proposed measurement, combining the above designs into a long, narrow pickup coil with a rounded shape. Newer SQUID technology, as well as longer averaging times, can lead to overall improvements in flux sensitivity. But, with careful arrangement of the sample, our unique pickup coil design can provide specific sensitivity to different values for the current fluctuations from ring to ring, as well as to the average current value over the whole ensemble.

One major problem with the larger type of pickup loop shown in Fig. 4.2(b) is that each ring couples differently to the loop, depending on its placement. We show our new design in perspective in Fig. 4.3 to illustrate the highly sensitive yet uniform inductance geometry of our proposed pickup coil. The rounded shape of the pickup coil closely matches the configuration of rings regularly spaced in a linear array. To first approximation, the pickup coil is a connected series of thirty loops, each coupled inductively only to the ring directly above it. As such, a single, uniform parameter $\mathcal{M}$ describes the the flux coupled to the SQUID:

$$\Phi_{\mathrm{SQUID}} \;=\; \mathcal{M} \times \sum_{p} I_p \sin\left(2\pi \frac{\phi}{\phi_p}\right). \tag{4.3}$$

The magnitude of this mutual inductance $\mathcal{M}$ depends critically upon the coaxial alignment as well as the distance d of separation between the rings and these individual pickup loops.

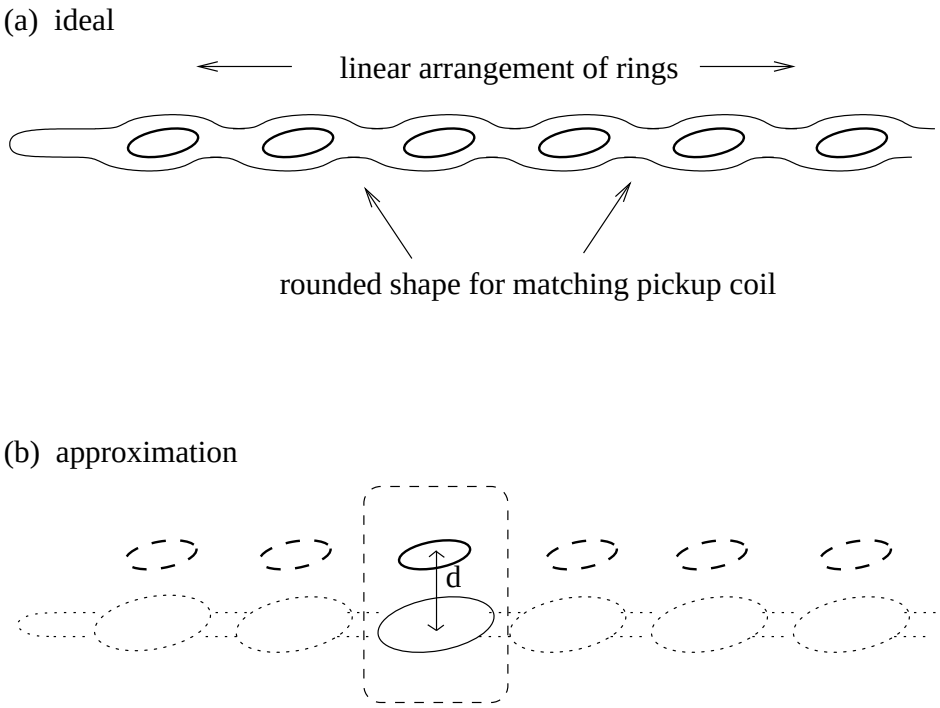

Figure 4.3: Illustration of the specific design and inductance geometry of the pickup coil in our proposed measurement. (a) Instead of a simple rectangular shape, we propose a rounded design that more closely matches the configuration of the rings in a linear array. In principle, the pickup coil is sensitive to the overall magnetic response of the ensemble, as well as to the specific fluctuations in a ring. (b) For an estimate of the coupling strength in this design, we model the pickup coil as a connected series of loops, each coupled only to the ring directly above it. For each pair, aligned coaxially with similar radii, the magnitude of the mutual inductance $\mathcal{M}$ depends most critically upon the distance d of separation.

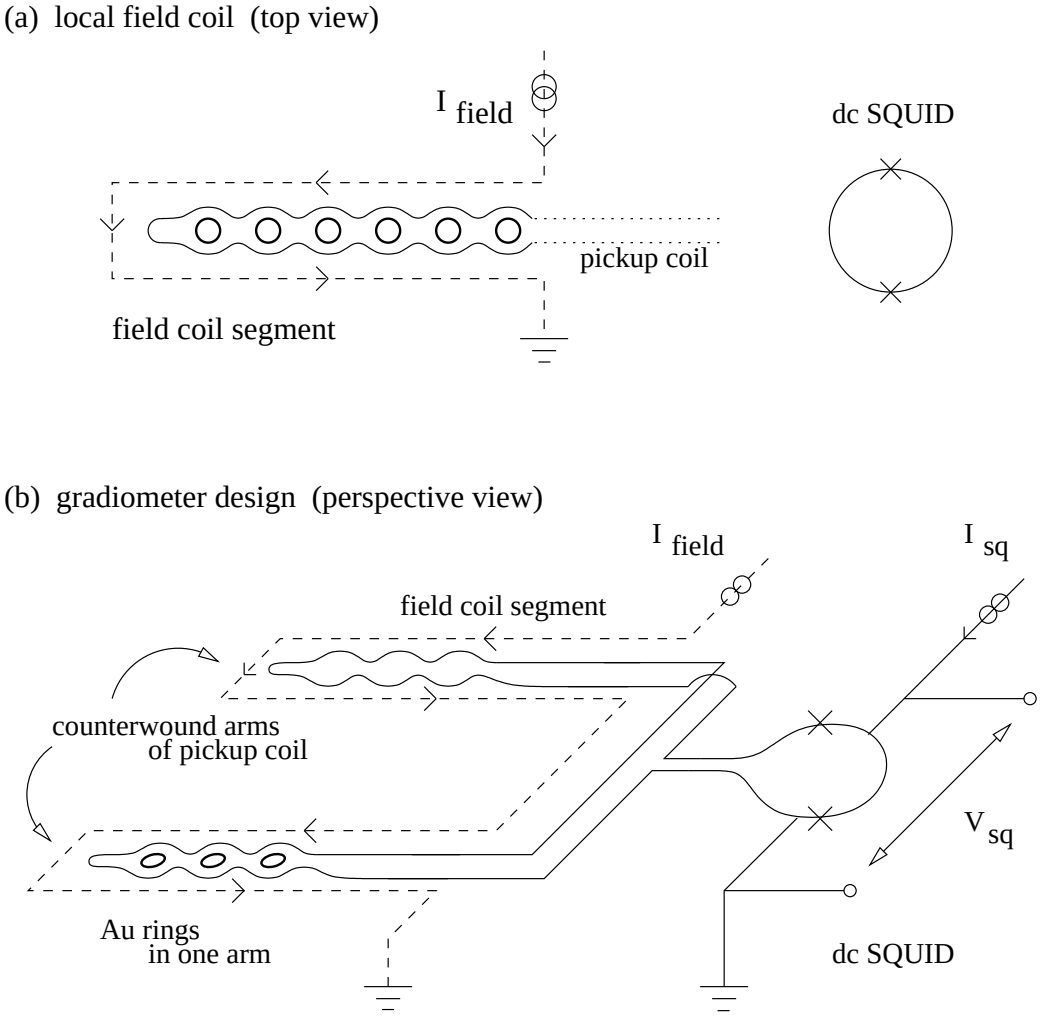

Figure 4.4: Proposed layout of our array of rings, relative to the counterwound pickup coil and on-chip field coils of the dc SQUID. (a) Viewed from above, the co-axial alignment of the rings to the pickup coil loops provides for stronger inductive coupling, as well as more uniform application of the applied magnetic field H_{field}. A current I_{field} passing through nearby field coil segments, away from the field-sensitive SQUID junctions. (b) Using a counterwound pickup loop, shown here in perspective, the dc SQUID is ultimately sensitive only to the response of the rings, patterned in the lower arm alone.

Regarding the measurement setup, we must also incorporate the field coils used for threading an Aharonov-Bohm flux through each ring while minimizing interference with the dc SQUID. In Fig. 4.4(a), we show a top-view of the rings, ideally aligned with the pickup coil underneath. We represent the field coil as a current-carrying wire situated on the same chip. Correct alignment of the rings to the pickup coil provides for stronger inductive coupling, as well as more uniform application of a magnetic field H_{field} for a given current I_{field}. In the design shown, the magnetic field is applied locally, away from the Josephson junctions of the dc SQUID. We note however that the amount of applied flux can greatly exceed the persistent current signal coupled to the SQUID. Our solution, shown in Fig. 4.4(b), is to stretch and fold the pickup coil into two counterwound arms, identical in shape but coupling flux to the SQUID in opposite directions. With a sample patterned only in one of the pickup coil arms, this gradiometer design effectively nulls out the applied field passing through both arms, while preserving sensitivity to the flux-response from the rings due to the persistent current.

Our proposed combination of a specialized pickup coil and on-chip field coil arrangement represents the most advanced design to date for a persistent current experiment, but not every device so manufactured will perform to expectations. Extensive testing of many such SQUID devices, at 4.2 K as well as at mK temperatures in the actual dilution refrigerator environment, is required to identify the devices with the best noise performance (typically, a few $\mu\Phi_0/\sqrt{\text{Hz}}$ at low frequencies) for possible use in a persistent current experiment. Depending on location, the presence of magnetic impurities near the pickup or field coils may also render some devices unsuitable. Significant dividends follow from careful testing and selection procedures at this stage, before patterning any rings.

4.2.2 Sample Fabrication

For our purposes, our array of thirty metallic rings, each approximately of size $L \sim 10\,\mu$m, must be accompanied by a similarly-fabricated control sample. Here we draw upon our knowledge base of nanofabrication procedures, especially the evaporation and lift-off of structures made from gold. The physical dimensions of each ring, such as the linewidth w and line thickness t shown in Fig. 4.5(a), as well as the relative spacing of the rings over the pickup coil, are defined during the lithographic and evaporation processes. In Fig. 4.5(b), we show a long control meander, to be co-fabricated with a similar linewidth w' and line thickness t' as the rings. From four-terminal measurements of this meander (see Ch. 2), we can estimate the length scales for disorder (ℓ_e) and phase coherence (L_φ) in the isolated ring.

In addition to providing details regarding the transport properties of electrons in our system, the Au control meander is essential for relating our experiment to the previous measurements. In Table 4.1, we list the relevant physical parameters of the samples from previous experiments, showing the range of different energy scales for the persistent current. Despite our emphasis on the difference in ensemble number, we propose to design our rings with roughly similar length and energy scales to allow side-by-side comparison.

To complete the comparison with previous experiments, especially with regards to the relevant energy scales, we propose to measure our sample at the lowest available temperatures in our cryostat. In Fig. 4.6, we plot logarithmically our estimates for the different energy scales, including the Thouless energy E_c for diffusion and the energy scale hv_F/l_e for ballistic transport. Given the approximate range of 1 mK to 10 K in cryogenic systems, shown also in Fig. 4.6,

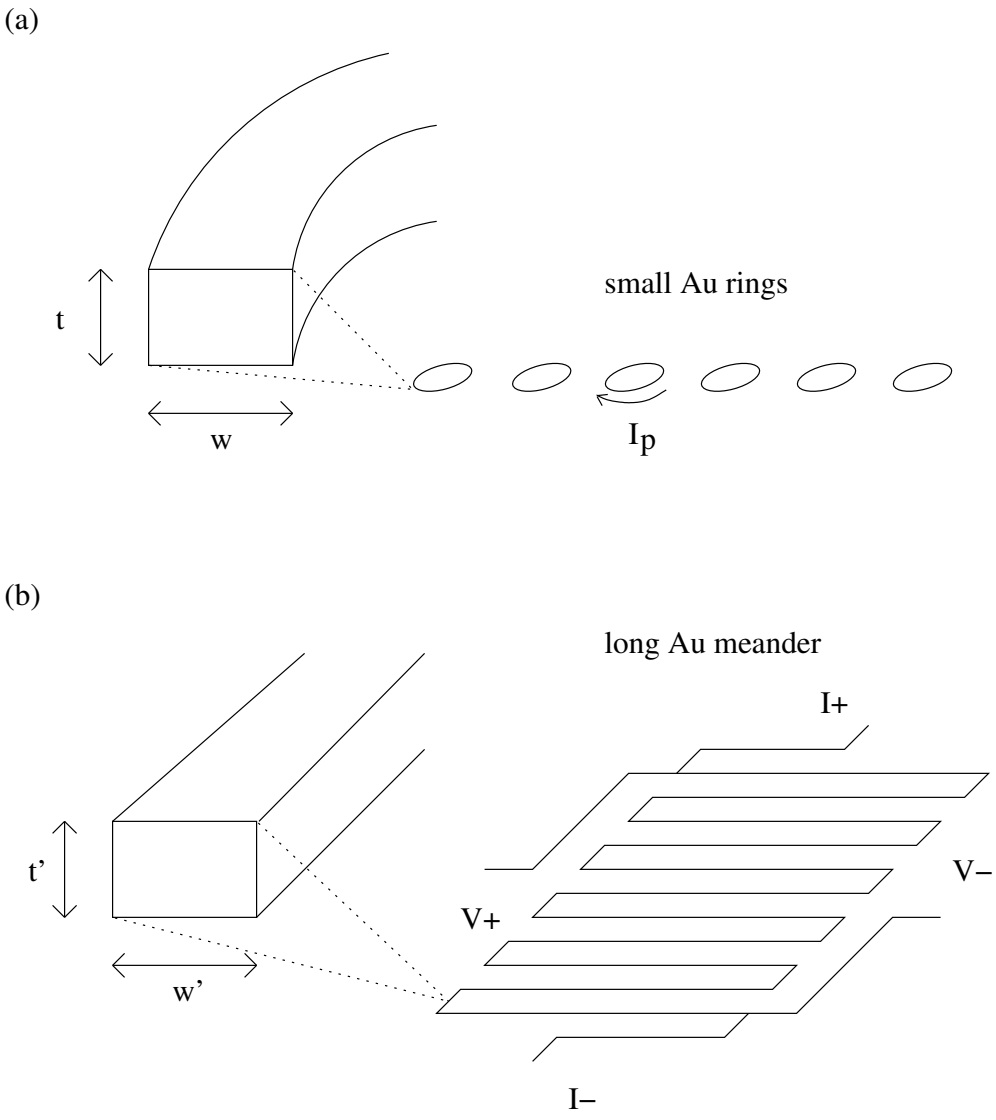

Figure 4.5: Cross-sectional diagrams of (a) one gold ring in the array and (b) the corresponding gold control meander. The similarities in fabricated linewidth ($w \approx w'$) and line thickness ($t \approx t'$) are controlled during the lithographic and evaporation processes. From four-terminal measurements of the meander, we can estimate the length scales for disorder (ℓ_e) and phase coherence (L_φ) in the isolated ring.

Experiments			L	L_φ	l_e	Δ	E_c	$e\Delta/\hbar$	$eE_c/\hbar$	ev_F/L
N	system	shape	(μm)	(μm)	(μm)	(mK)	(mK)	(nA)	(nA)	(nA)
1	GaAs	circ	8.3	25	11	32	159	0.67	3.33	5.2
1	Au	circ	12.6	12	0.07	0.016	4.78	0.00033	0.10	18
1	Au	circ	7.5	12	0.07	0.027	13.2	0.00056	0.28	30
1	Au	rect	8.0	12	0.07	0.025	11.8	0.00052	0.25	28
30	*Au*	*circ*	*To be designed with similar length, energy, and current scales.*							
10^5	GaAs	sq	8	7	3	8.2	33	0.17	0.67	3.6
10^7	Cu	sq	2.2	2.57	0.03	0.31	24.8	0.0065	0.52	102

Table 4.1: Comparison of our proposed ensemble of $N = 30$ Au rings to the sample sets measured previously. Despite our emphasis on the difference in ensemble number, we propose to design our rings with similar length, energy, and current scales, to allow for side-by-side comparison of our results. In the text, we describe the procedures for fabrication control of the quality of phase coherence (L_φ) and character of disorder (l_e) in our array of isolated rings.

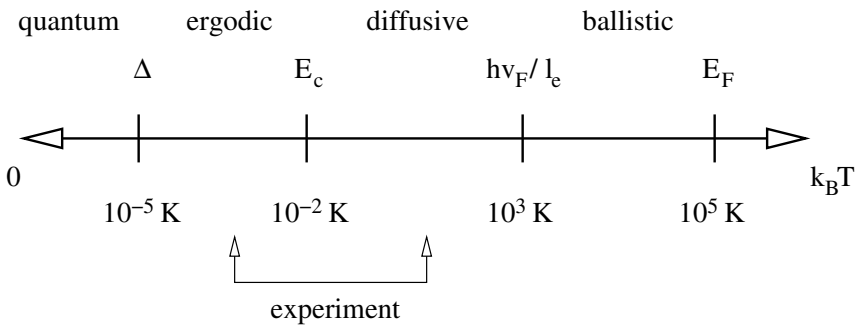

Figure 4.6: Logarithmic representation of relevant mesoscopic energy scales, in units of absolute temperature. In comparison to the mean level spacing Δ, the Thouless energy E_c for diffusion, the ballistic energy scale hv_F/l_e, and the Fermi energy E_F, the range of our experiment is primarily in the diffusive regime. (Adapted from Ref. [15].)

we expect our measurements to be limited primarily to the diffusive regime. We reiterate that these comparisons are made possible only after the fabrication and measurement of an appropriate control sample.

4.2.3 Data Analysis

As a result of our attention to the details of detector design and sample fabrication, we hope to measure distinctive h/e and $h/2e$-periodic oscillations in the magnetic response of the rings, as a function of the applied magnetic field. Despite the systematic errors expected from large magnetization signals in the background, a straightforward analysis using the Fourier transform would be sufficient for resolving a particular oscillatory component, limited only by the range of available data. Compared to the original unprocessed output from the SQUID, the inverse Fourier transform of the bandpassed signal of interest yields

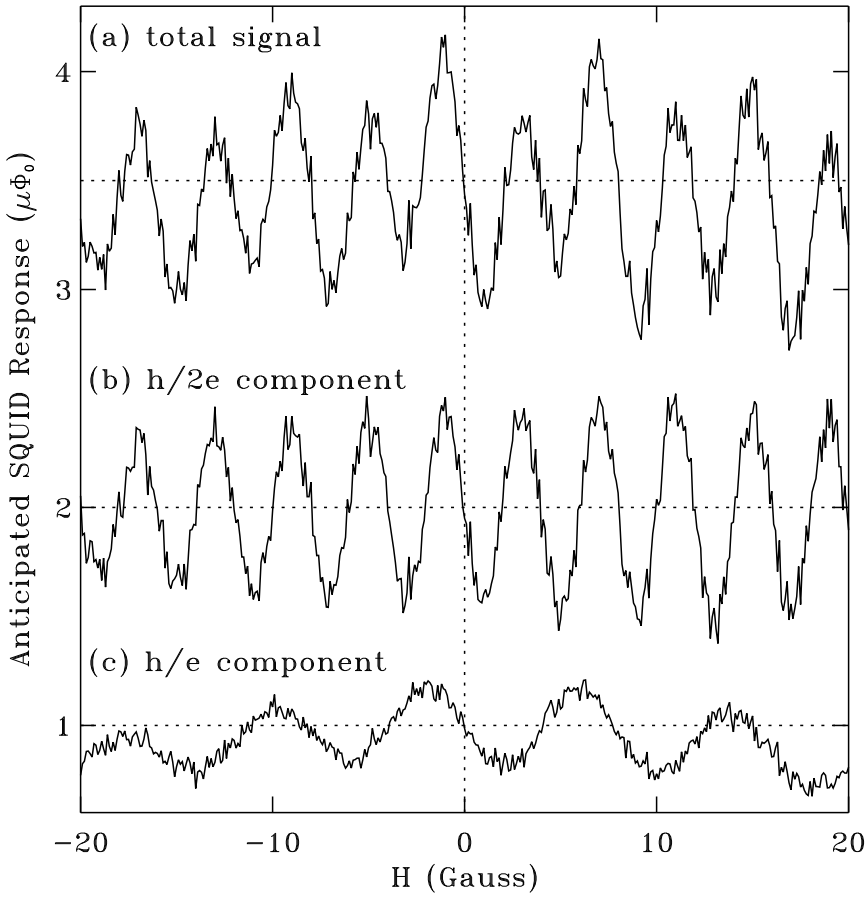

Figure 4.7: Simulation of the possible overlap of h/e- and $h/2e$-periodic components in a hypothetical data set. Though the total signal shown in (a) is exactly the sum of (b) a simulated $h/2e$ component and (c) a simulated h/e component, the larger $h/2e$ oscillations appear to mask the smaller h/e response. Through low frequency modulation of the applied magnetic field, each component can be isolated and selectively studied as a function of the modulation amplitude.

unambiguous results for the amplitude and sign of that particular periodic component of the magnetic response, apart from the background magnetization.

The expectation of both h/e- and $h/2e$-periodic components in the data, however, poses a separate challenge that is unique to our experiment. Eq. (4.2) illustrates that each oscillatory component (with period $\phi_p = h/e, h/2e, \dots$) is an odd function in the applied flux ϕ. Consequently, the overlap of the $h/2e$-periodic contribution may mask the observation of a smaller h/e oscillation at the origin: we illustrate such a scenario in Fig. 4.7, using simulated data of h/e- and $h/2e$-periodic signals with artificial high-frequency "noise" added in by hand. To consider each component separately, we must take full advantage of the ac modulation techniques used in previous experiments [2, 4] to filter the signal of interest in systematic fashion.

More precisely, we propose to control the amplitude of the ac modulation to selectively isolate either the h/e or $h/2e$ response in a specific harmonic of the magnetization, as demonstrated in the following derivation. By adding a small low-frequency signal ϕ_{ac} to the static flux ϕ_{dc} passing through each ring:

$$\phi \rightarrow \phi_{dc} + \phi_{ac} \sin(2\pi f t), \tag{4.4}$$

we introduce an added dependence on both the amplitude and frequency of this flux-modulation into the persistent current signal:

$$I_p \sin\left(2\pi \frac{\phi}{\phi_p}\right) \;=\; I_p \sin\left(2\pi \frac{\phi_{dc}}{\phi_p} + 2\pi \frac{\phi_{ac} \sin\left(2\pi f\, t\right)}{\phi_p}\right). \tag{4.5}$$

With the help of trigonometric addition formulas [48], the nested dependence of

the two sine functions can be expanded as:

$$\begin{aligned} I_p \sin\left(2\pi\frac{\phi}{\phi_p}\right) &= I_p \sin\Big(2\pi\frac{\phi_{dc}}{\phi_p}\Big)\, J_0\Big(2\pi\frac{\phi_{ac}}{\phi_p}\Big) \\ &+ 2I_p \cos\Big(2\pi\frac{\phi_{dc}}{\phi_p}\Big)\, J_1\Big(2\pi\frac{\phi_{ac}}{\phi_p}\Big)\, \sin\Big(2\pi f_1\, t\Big) \\ &- 2I_p \sin\Big(2\pi\frac{\phi_{dc}}{\phi_p}\Big)\, J_2\Big(2\pi\frac{\phi_{ac}}{\phi_p}\Big)\, \sin\Big(2\pi f_2\, t - \tfrac{\pi}{2}\Big) \\ &- 2I_p \cos\Big(2\pi\frac{\phi_{dc}}{\phi_p}\Big)\, J_3\Big(2\pi\frac{\phi_{ac}}{\phi_p}\Big)\, \sin\Big(2\pi f_3\, t - \pi\Big) \\ &+ \ldots \end{aligned} \tag{4.6}$$

to emphasize the distinct frequency components of the response (not to be confused with the flux-period components) – not only at the modulation frequency $f_1 = f$, but also at higher multiples given by $f_2 = 2f$, $f_3 = 3f$, etc. We refer to Eq. (4.6) as the Bessel function dependence relation, noting that the additional factors $J_n(2\pi x)$ modulating the magnitude of each n-th component are the usual integral Bessel functions $\{J_n\}$ (of the first kind). Following Ref. [48], we have utilized here the expansion formula

$$e^{2\pi i\, x \sin\theta} = \sum_n J_n(2\pi x)\, e^{in\theta}, \tag{4.7}$$

where the ratio $x = (\phi_{ac}/\phi_p)$ describes the relative degree of flux-modulation of a persistent current signal of the form $I_p \sin\theta$.

The Bessel function relation between the modulation and the resulting harmonics is the central result of this section. From Eq. (4.6), we see that each frequency component is still a sinusoidal function of the dc flux ϕ_{dc} through each ring, but with an additional dependence on the specific ac drive amplitude ϕ_{ac}. The use of a small ac flux-modulation in fact *reduces* the amplitude of the oscillation at each frequency f_n, by the corresponding Bessel function factor $J_n(2\pi x)$; however, by adjusting this ac modulation to maximize a specific nth-order Bessel

function value, we can filter the SQUID output to emphasize either the h/e- or $h/2e$-periodic signal in our choice of the n-th harmonic.

We illustrate this point by considering what happens if the amplitude of the ac modulation is chosen incorrectly: in principle, this maximizes the amplitude of any signals that oscillate at periods other than that of the desired persistent current signals. The h/e and $h/2e$ oscillations are still present in the data, but are now significantly reduced in amplitude and effectively filtered out. Reverting back to our original purpose, by calculating the correct modulation amplitude, we can instead filter out any background signals – including either the h/e or $h/2e$ signal – in order to study only one specific flux-periodic component.

Regarding Fig. 4.7, the Bessel function relation is essential in distinguishing between signals that overlap at the origin. Since the set of Bessel functions $\{J_n(2\pi x)\}$ are by definition not periodic in x, the modulation setting which maximizes the h/e oscillations helpfully does not also maximize the $h/2e$ oscillations at the same frequency f_n. Previous experiments have utilized this modulation technique to isolate one specific flux-periodic component from other background signals in the data; given our interest in both h/e- and $h/2e$-periodic signals, the specific Bessel function dependence of the data on different amplitudes of ac modulation is critical to our proposed analysis of both the flux-periodic contributions to the magnetic response.

4.3 Motivation

Aside from proof-of-principle, our motivation for undertaking this new experiment stems from the many questions surrounding the persistent current, re-

garding both experimental data as well as theoretical understanding. In a larger context, we also find that the persistent current problem bears upon the question of phase decoherence at low temperatures, but from a unique, thermodynamics-based perspective. In the following, we identify these motivations as means of defining specific goals for this thesis work.

To demonstrate the proposed measurement. Our stated objective is to measure conclusively the significant h/e and $h/2e$ contributions to the persistent current in the same sample of mesoscopic rings. As the backbone of an experimental thesis, this goal can be framed as a series of technical or skill-based challenges, as identified in Sec. 4.1 and Sec. 4.2. Our new experiment relies critically upon these measurement-related factors, including the statistical basis of the number of rings to measure, the precise design of the array and the matching SQUID pickup coil, the controlled fabrication of disordered samples with long phase coherence lengths, and the analysis of the data through its dependence on the ac modulation. This series of requirements, in turn, will dictate the format of the presentation of our experiment in Ch. 5.

To complement existing experimental data. We also emphasize the relatively sparse set of results from initial experiments [2, 4, 5, 7], for either the h/e- or $h/2e$-periodic response. Table 4.2 presents an overview of all results for the sign, amplitude, and temperature dependence. We draw attention to the sign of the response, which is reported in only two experiments, and in only three of the six samples overall. Moreover, the amplitudes reported in all cases are only reflective of the measurements made at lowest temperatures; like the sign, the exponential relationship of the response at higher temperatures is not reported for all the samples. In addition to these specific gaps in knowledge, we note that none

Experiments			$I_{\text{typical}} \equiv \sqrt{\langle I_n^2 \rangle}$				$I_{\text{average}} \equiv \langle I_n \rangle$			
N	system	[Ref]	per	sign	ampl	temp	per	sign	ampl	temp
1	GaAs	[5]	$\frac{h}{e}$	– ? –	$0.77\,\frac{ev_F}{L}$	– ? –	*— not measured —*			
1	Au	[4]	$\frac{h}{e}$	– ? –	$0.17\,\frac{ev_F}{L}$	– ? –				
1	Au	[4]	$\frac{h}{e}$	para	$1.0\,\frac{ev_F}{L}$	$e^{-\sqrt{\frac{T}{4.8}}}$				
1	Au	[4]	$\frac{h}{e}$	para	$0.21\,\frac{ev_F}{L}$	$e^{-\sqrt{\frac{T}{4.8}}}$				
30	*Au*	–	*Proposed measurement of both contributions to the persistent current.*							
10^5	GaAs	[7]	*— not measured —*				$\frac{h}{2e}$	dia	$2.24\,\frac{eE_c}{\hbar}$	$e^{-\frac{T}{190}}$
10^7	Cu	[2]					$\frac{h}{2e}$	– ? –	$0.77\,\frac{eE_c}{\hbar}$	$e^{-\frac{T}{80}}$

Table 4.2: Overlap of our proposed experiment with the original group of four experiments. For comparison, we present the current amplitudes in terms of either the respective ballistic (ev_F/L) or diffusive ($eE_c/\hbar$) current for each system. Following from our choice of an intermediate number $N = 30$ of Au rings, we propose to measure both the h/e and the $h/2e$-periodic contributions to the persistent current, specifically addressing the questions of sign, amplitude, and temperature dependence in the overall set of results.

of the measurements in either diffusive or ballistic systems are independently confirmed. With our new experiment, we seek to provide a complete set of results for both the typical and average current to compare directly to previous experiments.

To address major theoretical questions. As discussed in detail in Ch. 3, we can identify several unresolved issues regarding the theoretical description of the persistent current and its agreement with experiment. Of interest is the predicted randomness of the sign of the typical current, i.e. equally paramagnetic or diamagnetic, which has yet to be demonstrated explicitly. For the average current, we also note that the diamagnetic sign seen in ballistic systems in heterostructures has not been measured conclusively in a diffusive metallic system. In addition, our experiment aims to directly address the conceptual divide between the experimental data and competing calculations for the amplitude and temperature dependence for both the typical and the average contributions to the persistent current. Specifically, we note that only the first experiment listed in Table 4.2 can be accounted for within the framework of existing theories.

To investigate phase coherence in mesoscopic systems. More generally, we can identify a goal of studying the physics of electronic phase coherence, with the distinction of probing a more isolated system. The idea of phase coherence in condensed-matter systems is by itself not new: for one, superconductors have long been studied for their macroscopic phase coherent properties. On the mesoscopic scale, charge-related phase coherence effects are observed in metals, semiconductors, and even insulators – through the use of biased voltage and current probes. The study of the persistent current in rings allows for direct investigation of the phase coherent behavior of electrons, isolated from dephasing

or other transport-related effects in electron reservoirs.

To study thermodynamic properties in mesoscopic systems. In this sense, in addition to demonstrating phase coherence and the subsequent quantum mechanical phenomena, the persistent current problem is also significant in opening up a whole new field of investigation into the thermodynamics of mesoscopic systems. One immediate consequence is the discovery that there is something interesting at all about the thermodynamics of less-than-macroscopic systems [19].

To demonstrate the nature of self-averaging. Finally, we can identify a fundamental objective unique to our experiment: to demonstrate the mesoscopic character of the persistent current. Consider the number of rings measured: in single-rings, only the h/e typical current $\sqrt{\langle I^2 \rangle}$ is clearly measured; any $h/2e$ contribution from an average over an "ensemble" of $N = 1$ is not to be expected. In contrast, in the very large ($N = 10^5, 10^7$) multiple-ring arrays, any signal from the h/e typical current (which grows as $\sqrt{N}$) is apparently overwhelmed by the $h/2e$ average current (which grows as N). This manner of adding random variables versus summing up the ensemble average is, at heart, statistical; however, without experimental demonstration, the principle has not been shown to apply specifically to mesoscopic thermodynamic phenomena. For the case of persistent currents, the explicit demonstration of this fundamental averaging principle can be achieved via measurement of both the typical and average currents in an ensemble comprised of an intermediate number N' of rings, where $1 < N' << \infty$.

Chapter 5

Experiment

In this chapter, we describe in detail our new experiment on both the h/e- and $h/2e$-periodic contributions to the persistent current in the same ensemble of an array of thirty Au rings. Building upon our discussion of flux-sensitivity and inductance design in Ch. 4, we describe the layout of our SQUID-based experiment and the fabrication of our mesoscopic samples with long phase coherence lengths. As the central feature of our work, we present the data for the measurement of the magnetic response of our sample, focusing on our determination of the sign and our analysis of the signal amplitude of the two contributions – mainly at lowest temperatures as a function of applied magnetic field. We also present our data for the temperature dependences of both the h/e and $h/2e$ currents. The sum of all these data leads to our primary conclusion: in a small ensemble of mesoscopic Au rings, we unexpectedly but clearly observe a diamagnetic sign, robust nanoampere-size amplitudes, and relatively weak exponential temperature dependences for both the typical and average contributions to the persistent current.

5.1 Design

At the heart of our new experiment is the innovative SQUID design used to measure the small fluxes generated by the persistent current. Tailored specifically to measure the response of a linear array of thirty rings [47], these SQUIDs are designed and fabricated at IBM Research (Yorktown Heights) using a proprietary process called PARTS (Planarized All-Refractory Technology for Superconductors) [49]. Though personally not involved in the layout or manufacture of these SQUIDs, we refer here to two advantages of their fabrication using PARTS: the first is the patterning of Nb films into narrow wires with sub-micron scale features, using e-beam lithography and reactive ion etching; the second is the uniform deposition and chemical-mechanical planarization of a thick insulating SiO_x layer between different Nb levels, independent of the more delicate $Nb - AlO_x - Nb$ junction trilayers. The SEM photo in Fig. 5.1 illustrates the detailed patterns of the narrow pickup coil and SQUID wiring, defined in the bottom Nb level. The large segments shown in lighter contrast are the SQUID field coils and counterelectrode, defined in a higher Nb level. Separating the Nb levels is the intervening SiO_x layer, which has been planarized to allow for the clean evaporation and liftoff of additional lithographic structures; Fig. 5.1 also shows the Au rings we have deposited onto the SiO_x surface, above the pickup coil and in the same plane as the field coils.

The general outline and spacing of our array of rings reflects the rounded design of the underlying pickup coil. Fig. 5.2 shows the sub-micron linewidth of the Nb pickup coil lines, shaped to make a series of squarish loops, measuring $\sim 2.8\,\mu$m on a side. We pattern the Au rings approximately $5\,\mu$m apart with a mean diameter of $2.56\,\mu$m to match individually to these pickup loop segments,

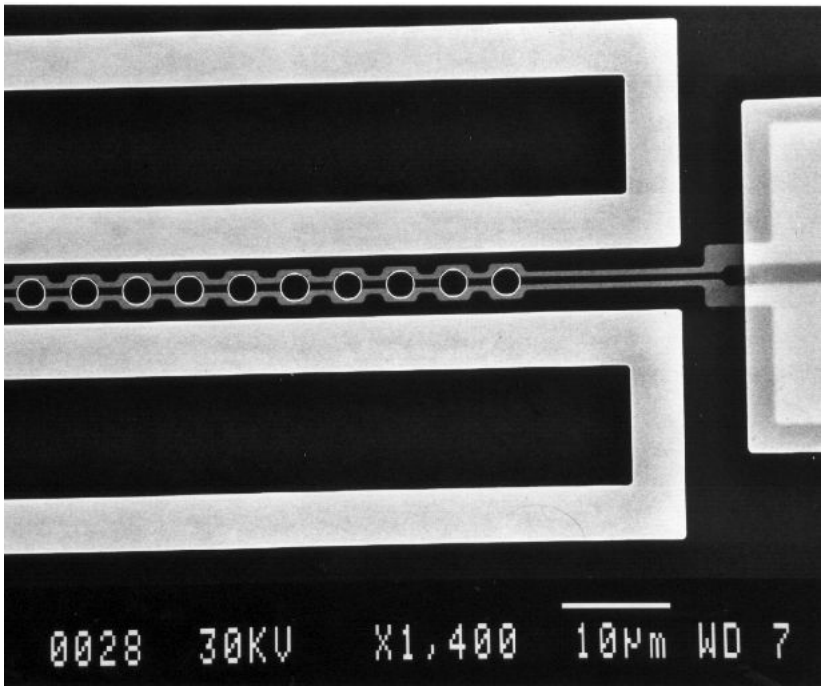

Figure 5.1: Detail of design levels in the fabrication of our SQUID device. At right, the SEM photo highlights the contrast between the bottom Nb level of SQUID wiring leading to the pickup coil, and the top Nb level of the SQUID counterelectrode. The 150nm thick Nb levels are separated by a 150nm thick insulating layer of SiO_x. Also visible in the upper level are the Au rings we have deposited on to the planarized SiO_x surface, above the matching pickup coil.

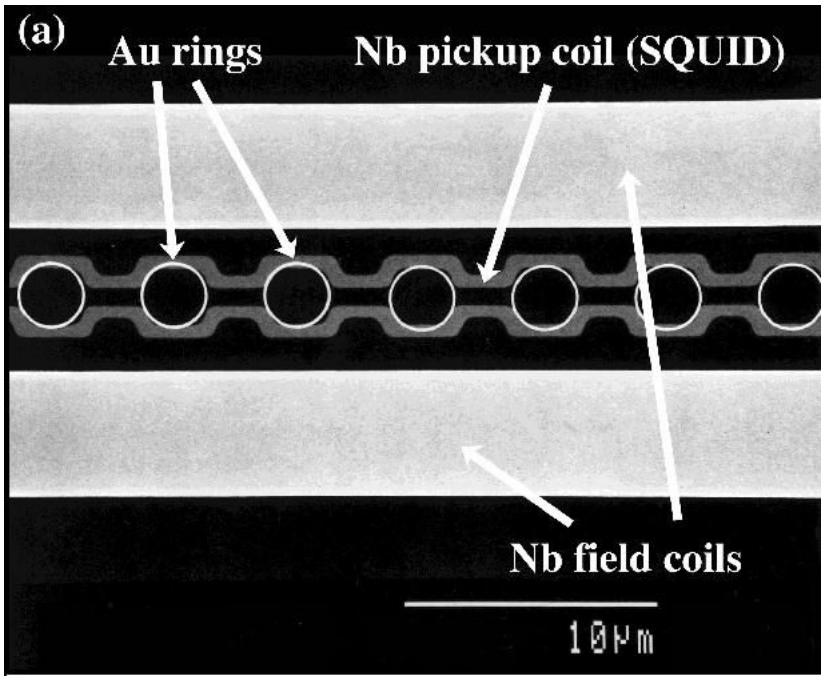

Figure 5.2: Unique design of the SQUID pickup coil to match a linear array of mesoscopic rings. The specific shape of our pickup coil resembles a connected series of squarish loops, each $\sim 2.8\,\mu$m on a side. Centered over each loop to within $\pm\,0.2\,\mu$m, we have fabricated thirty nominally identical Au rings of mean diameter $2.56\,\mu$m to match the pickup coil. Given the thin $0.15\,\mu$m $Si0_x$ interlayer, the calculated inductance of $\mathcal{M} = 2.7 \pm 0.1\,$pH per ring provides for good sensitivity to the typical current in each ring, as well as to the average current over the whole array.

thus providing sensitivity to the different values for the fluctuating current from ring to ring, as well as to the average current from the whole ensemble of rings. We differentiate the contributions according to the flux periods of oscillation. For the rings shown, each enclosing an area $\mathcal{A} \approx 5.15\,\mu\text{m}^2$, we calculate that a magnetic field of $\sim 8\,\text{gauss}$ passing through each ring corresponds to an h/e flux. Likewise $\sim 4\,\text{gauss}$ corresponds to an $h/2e$ flux.

As opposed to a large loop encircling an array of much smaller rings, our pickup coil is equally coupled to each of the thirty rings, separated only by the 150 nm thick insulating layer of SiO_x and aligned with the rings to within $\pm\,0.2\,\mu\text{m}$. Using inductance model programs to account for the finite cross-sections of the different segments [50], we calculate the mutual inductance to be $\mathcal{M} = 2.7\,\text{pH}$ per ring and uniform to within 5% from ring to ring, based on the quality in planarizing the SiO_x surface. We emphasize the importance of this sole factor $\mathcal{M}$ in consolidating our investigation of the typical and average persistent currents: by dividing the total flux response Φ_T by $\mathcal{M}$, we can compute an effective total current I_T from all N rings, independent of whether I_T adds up like $(N \times I_{\text{av}})$ or $(\sqrt{N} \times I_{\text{typ}})$.

To corroborate the computed values of this essential parameter $\mathcal{M}$, we consult some textbook tables for estimates of the mutual inductance of two coaxial rings of negligible cross-section. In these idealized situations, we must ignore the finite $0.5\,\mu\text{m}$ linewidth of the pickup coil, as compared to the other length scales in the problem. For two closely-spaced ideal rings of equal radius $a = 1.28\,\mu\text{m}$, we estimate the mutual inductance to be 3.6 pH [51], of the same order of magnitude as above. For coaxial circles of different radii, the coupling is reduced: choosing radii of $a = 1.28\,\mu\text{m}$ and $a' = 1.78\,\mu\text{m}$ (equal in perimeter

to the 2.8 μm square pickup loop) yields a mutual inductance of 2.2 pH [51]. Considering the benchmark of a few $\mu\Phi_0/\sqrt{\text{Hz}}$ for the noise bandwidth of one of our SQUID devices, this general range of values for the mutual inductance indicates sensitivity to a total current of ≤ 1 nA, before averaging.

With the use of inductance tables, we also address the problematic issue of interactions within our ensemble of thirty rings via inductive coupling between neighbors. The mutual inductance between coplanar equal rings is given for the cases of $(r/2a)$ large and $(r/2a)$ small, where r is the distance between centers [51]. For two rings of equal radii $a = 1.28\,\mu$m, spaced $r = 5\,\mu$m apart, as shown in Fig. 5.2, we estimate a mutual inductance between neighbors of ~ 0.025 pH; roughly a hundred times smaller than the primary coupling $\mathcal{M}$, this inductive coupling between rings is not of significant concern.

The pickup coil design is but one feature of our unique SQUID device. In Fig. 5.3, we show a larger view of this SQUID, with a white box highlighting the region previously shown in closeup. Besides the SQUID counterelectrode (at right), the primary feature in the photo is the pair of on-chip Nb field coils (at left), shaped like tuning forks stretching $\sim 150\,\mu$m to enclose the two counterwound arms of the SQUID pickup coil. In this gradiometer configuration, a current (of order ~ 10 mA) applied to the field coils produces roughly the same local magnetic field in each pickup coil arm, only one of which also contains our array of Au rings. Using an additional center tap (not shown), we can offset any inequality in the field coupled to both arms to better than 3 ppm, leaving the SQUID pickup coil sensitive only to the magnetic response of our array of rings.

Far away from these field coil lines, the magnetic field dies off very quickly, alleviating concerns over the amount of stray flux passing through the SQUID

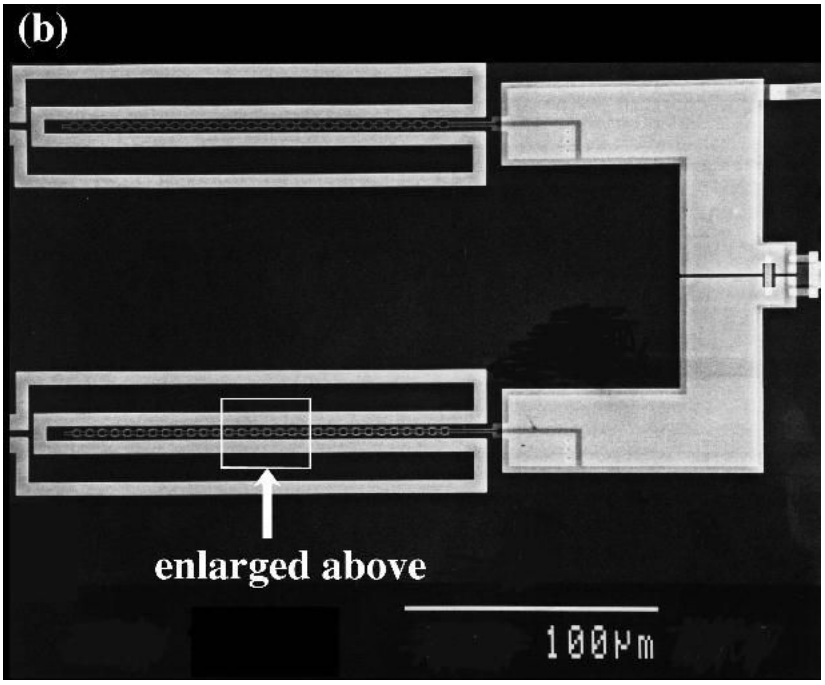

Figure 5.3: Gradiometer configuration of the wide superconducting field coils with respect to our single line of small Au rings and the two counterwound arms of the SQUID pickup coil. (For reference, the area detailed in Fig. 5.2 is labeled.) Running parallel to the pickup coil arms, this pair of on-chip field coils is in fact a continuous 5 μm-wide Nb line, designed to carry almost 25 mA before quenching. The two pickup coil arms are counterwound to null out the resulting $\pm$20 G field, sensing only the magnetic response of the Au rings over the lower arm.

$Nb - AlO_x - Nb$ junctions (shown at the far right edge of Fig. 5.3). By the same token, the local field close to the field coils is distinctly non-uniform, especially across the narrow area of the pickup coil in the transverse direction. In the case of a persistent current experiment, the total flux through the Au rings to be measured and not the field profile itself is of primary importance. In this sense, our measurement is self-calibrating: for a given current I applied to the field coils, we use a constant value of $(B/I) = 844\,\mathrm{G/A}$ for the resultant field strength in the plane of the pickup coil, derived from the spacing observed between $h/2e$ oscillations and the known area of the rings.

Nonetheless, for comparison, we can also numerically model the magnetic field profile in the region inside the pickup coil from currents passing through the four individual $5\,\mu$m-wide segments of the "tuning-fork" shaped Nb field coil. (See Fig. 5.3 for reference.) For modeling this wide but thin Nb film, we will assume that the applied current flows through the field coils along the inner and outer edges only and not through the middle; this corresponds to eight idealized current wires, at distances of $3.5, 8.5, 20.0,$ and $25.0\,\mu$m from the center line of the pickup coil. Superposition of our calculations for $B = \mu_0 I/2\pi r$ yields the in-plane field strength in the region inside the pickup coil from all eight current wires. Given the "tuning-fork" geometry of the field coil, we note that the greatest contribution to the magnetic field comes from the innermost field coil segments closest to the pickup coil.

Figure 5.4(a) shows a cross-sectional view of the field coil modeled as eight idealized wires. We use $\mathbf{p}$'s to identify the position of the pickup coil and $\mathbf{x}$'s and $\mathbf{o}$'s to signify end-on views of the applied current passing into and out of the page, respectively. Using $B = \mu_0 I/2\pi r$ for each of the current wires, we

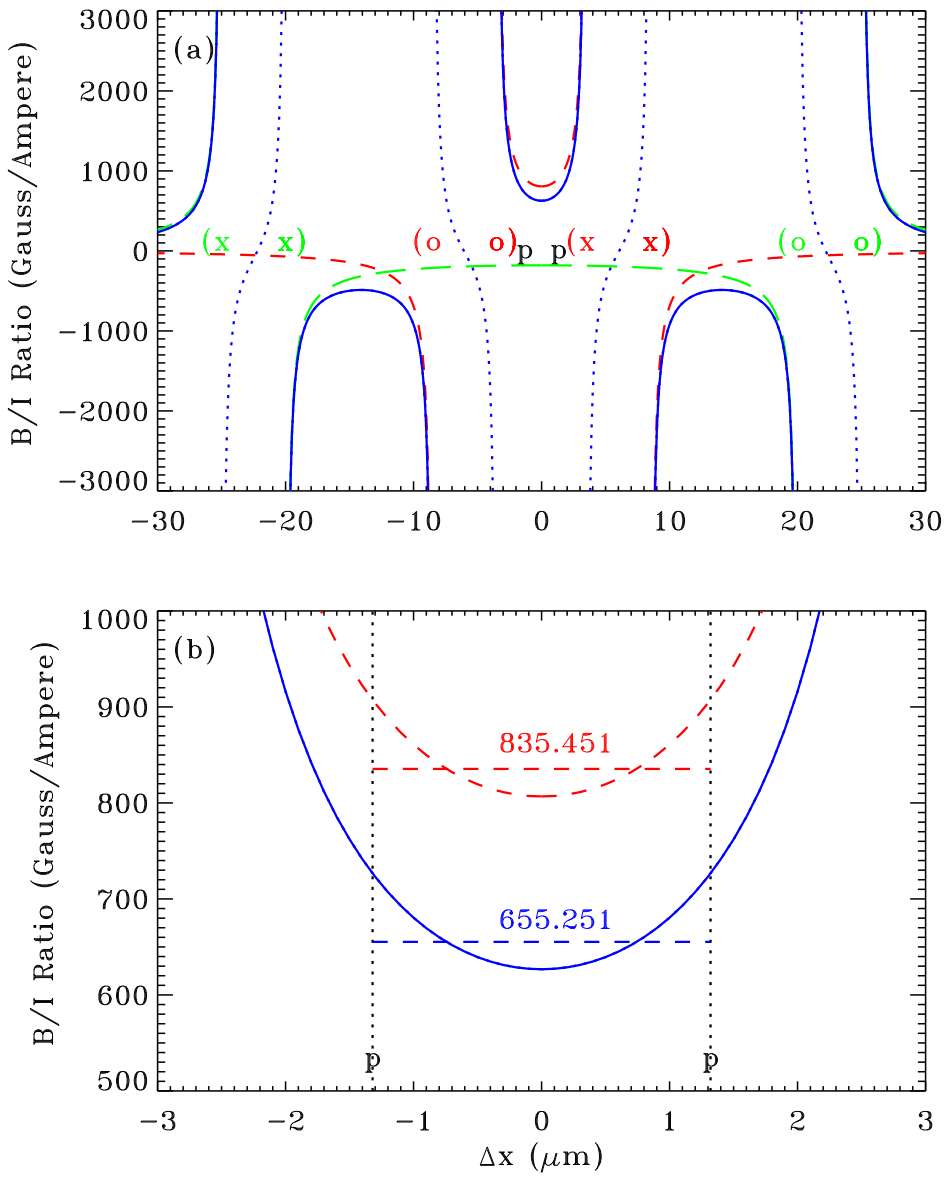

Figure 5.4: Numerical model of the in-plane magnetic field strength, based on the relative positions of currents in the field coil, as shown in cross-section. Please see the text for more details.

plot in Fig. 5.4(a) the scalar values for the in-plane magnetic field, with positive values assigned for the up direction through the pickup coil. The dashed lines in the plot show the dominant contribution from the innermost current wires as well as the counterbalancing contribution from the outer current wires. The combination of the two is plotted using solid lines, demonstrating the sharp curvature of the field strength in the regions between the field coil segments. As for the field passing through the segments themselves, we use dotted lines to represent the calculated field strength; in practice, however, magnetic field lines cannot in general penetrate these (borderline) Type I Nb films due to the Meissner effect, and are diverted outside.

In Fig. 5.4(b), we replot the critical region around the pickup coil. Again considering the Meissner effect and the width of our Nb pickup coil, roughly half of the displaced field lines are "focused" inside the pickup coil area; in the plot, then, we use the mean radius of $\pm 1.32\,\mu$m for marking **p**. Comparing the solid curve to the dashed curve, our model indicates that the counterbalancing contribution from the distant outer wires leads to a rather large reduction in the overall field strength, as well as a minor flattening of the field at the center. Computed by numerically integrating over the region inside the pickup coil, the two horizontal lines in Fig. 5.4(b) represent constant values of either 835 or 655 G/A for the (B/I) field strength factor. Both values are less than our empirically determined value of 844 G/A, suggesting some limitations exist in our simplified numerical model.

We repeat that, in our case, the profile of the magnetic field does not matter, only the total flux passing through our rings; the local field strength, however, must be sufficient to see more than a few persistent current oscillations, based

on the number of flux quanta passing through the area enclosed by each ring. Taking $J_c \sim 5 \times 10^6\,\mathrm{A/cm^2}$ for the critical current density of these $5\,\mu$m-wide, 150 nm-thin Nb films [52,53], we estimate that our field coils can support a superconducting current of 30 mA without going normal. Given $(B/I) = 844\,\mathrm{G/A}$, the field range of ± 25 gauss allows for the possibility of observing more than twelve $h/2e$ oscillations (4 G) or six h/e oscillations (8 G).

5.2 Fabrication

Following extensive testing of these IBM-made SQUID devices, at 4.2K as well as at mK temperatures in the dilution refrigerator environment, we must still successfully fabricate our sample of Au rings onto a viable SQUID device. Most of the steps used here follow standard recipes for nanoscale fabrication – emphasizing substrate and resist preparation, astigmatism and focus correction in SEM-based lithography, controlled evaporation and non-destructive liftoff of metallic structures, and careful sample handling and wire bonding to minimize electrostatic discharge. Though all critical to the success of our experiment, we focus instead on a few sample control procedures that, as above with the SQUID design, speak directly to the quality of our results for the persistent current.

We first focus on the physical dimensions of our Au sample. Figure 5.5 shows a high-magnification SEM photograph of one of the thirty Au rings; the SEM here is the same used for the computer-controlled e-beam lithographic process. The scale bar at lower right provides the primary method for verifying the physical dimensions of our rings *ex post facto*. We note that higher magnifications require more care in reducing the image blurring that comes with higher beam

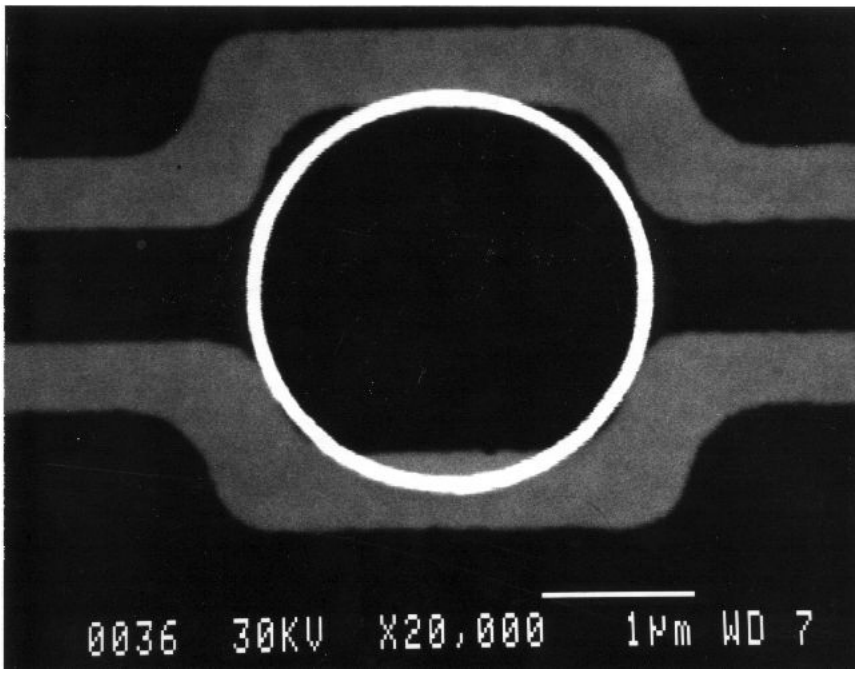

Figure 5.5: Photographic determination of the dimensions of the Au rings at high SEM magnification. The scale bar provides the primary method for feature size-measurement to within $\pm 20\,\mathrm{nm}$. We estimate a length $L = 8.0\,\mu\mathrm{m}$ and a linewidth $w = 110\,\mathrm{nm}$ for each of our nominally identical mesoscopic rings. In the text, we describe our methods for determining the thickness $t = 60\,\mu\mathrm{m}$.

currents. From a set of photographs at different scales, we estimate a mean diameter of 2.56 μm, and a linewidth $w = 110$ nm for each of our mesoscopic rings. It follows that each ring has a length $L = 8.0\,\mu$m and an area $\mathcal{A} = 5.15\,\mu\text{m}^2$ per ring. For the thickness $t = 60$ nm, we rely upon the accuracy of the crystal-oscillator rate-monitor inside the thermal evaporation chamber, but also check these values through subsequent alpha-step measurements of a co-evaporated Au film. For comparison to other classes of mesoscopic systems, e.g. quantum dots, we note that the volume $\mathcal{V} = 0.053\,\mu\text{m}^3$ corresponds to a 375 nm cube with discrete level spacings on the order of tens of μK (10^{-9} eV).

We turn next to determining the length scales for diffusion and phase coherence in our sample. Here, we must rely upon separate transport measurements in a co-evaporated Au sample with similar cross-sectional dimensions, but connected of course to macroscopic bonding pads. We prepare a 207 μm long Au control meander [23], defined lithographically with the same linewidth $w' = 110$ nm as the Au rings and co-evaporated at the same time to the same thickness $t' = 60$ nm using the same 99.999% pure Au material. From the resistance value of $R = 301\,\Omega$, we calculate a mean free path $l_e = 87$ nm using the Drude model formula

$$\sigma \equiv \frac{1}{\rho} = \frac{ne^2}{m_e}(\frac{v_F}{l_e}) \tag{5.1}$$

and the textbook values for the electron density n and Fermi velocity $v_F = 1.4 \times 10^6$ m/s in a perfect Au lattice [17]. Regarding the dimensions required for diffusive transport, we note that here $l_e > t$ but $l_e < w$, implying $d = 2$ for calculating the diffusion constant $D \equiv \frac{1}{d} v_F l_e = 0.061\,\text{m}^2/\text{s}$. Weak localization measurements of this control meander at cryogenic temperatures, as shown in Fig. 5.6, can be fit to the standard quasi-1D weak localization formula given

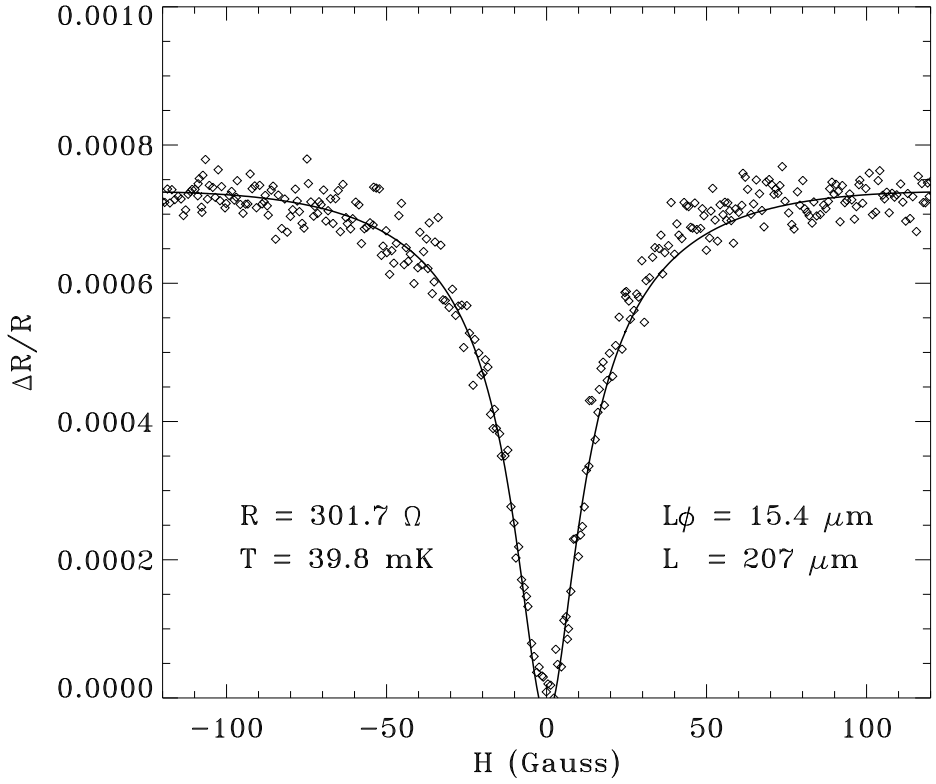

Figure 5.6: Magnetoresistance measurement of the Au control meander for our Au rings, demonstrating the weak localization interference correction to the quasi-1D wire's 301 Ω resistance at $T \approx 40\,\mathrm{mK}$. Though less than 0.1% of the total resistance, the magnitude of the dip corresponds to a phase coherence length of $L_\varphi \approx 15\,\mu\mathrm{m}$ in our 207 μm-long Au meander and, by inference, in our array of co-fabricated 8 μm-long Au rings.

in Eq. 2.9, yielding a phase coherence length $L_\varphi \approx 15\,\mu$m, or equivalently a phase coherence time $\tau_\varphi \approx 4\,$ns, at $T \approx 40\,$mK. In Fig. 5.7, we show the complete temperature dependence of $\tau_\varphi \equiv L_\varphi^2/D$ for a series of four disordered Au wires, including our control sample (here labeled Au-2). From this data on a co-evaporated control meander with $D = 0.061\,\mathrm{m}^2/\mathrm{s}$, we infer that $L_\varphi > L$ in our $8\,\mu$m-long rings up to temperatures as high as 1 K. In essence, we expect that electronic transport should be diffusive but dissipationless in our persistent current sample. We discuss the saturation of τ_φ at low temperatures in greater detail in Ref. [23].

We list the relevant energy and current scales for our Au rings in Table 5.1, along with the dimensional parameters from before. In temperature units, the discrete mean level spacing $\Delta \equiv (2\mathcal{N}_0\mathcal{V})^{-1} = 18.8\,\mu$K; we note this implies there are less than $E_F/\Delta \sim 10^9$ conduction electrons in each ring. At a more experimentally relevant temperature is the scale of correlations between energy levels, given by the Thouless energy $E_c \equiv \hbar D/L^2 = 7.3\,$mK. These two energy scales correspond to persistent currents of $e\Delta/\hbar = 0.0004\,$nA and $eE_c/\hbar = 0.15\,$nA, listed along with the current scale in the clean ballistic limit $ev_F/L = 28\,$nA. Multiplying these values for our particular sample design by the mutual inductance $\mathcal{M} = 2.7\,$pH for our particular pickup coil design yields a series of performance baselines for the SQUID device as a whole. To this end, our measurement of the noise bandwidth of our SQUID (incorporating any electronic noise referred back to the SQUID input) is $\sim 3\,\mu\Phi_0/\sqrt{\mathrm{Hz}}$ in the $2-20\,$Hz range, suggesting we must average the SQUID readout signal during experimental runs: for a feasible averaging time of $t \sim 10^2\,$sec per data point, the resulting noise floor is $\sim 0.3\,\mu\Phi_0$. Equivalent to a mean current of 0.008 nA per ring, i.e. after

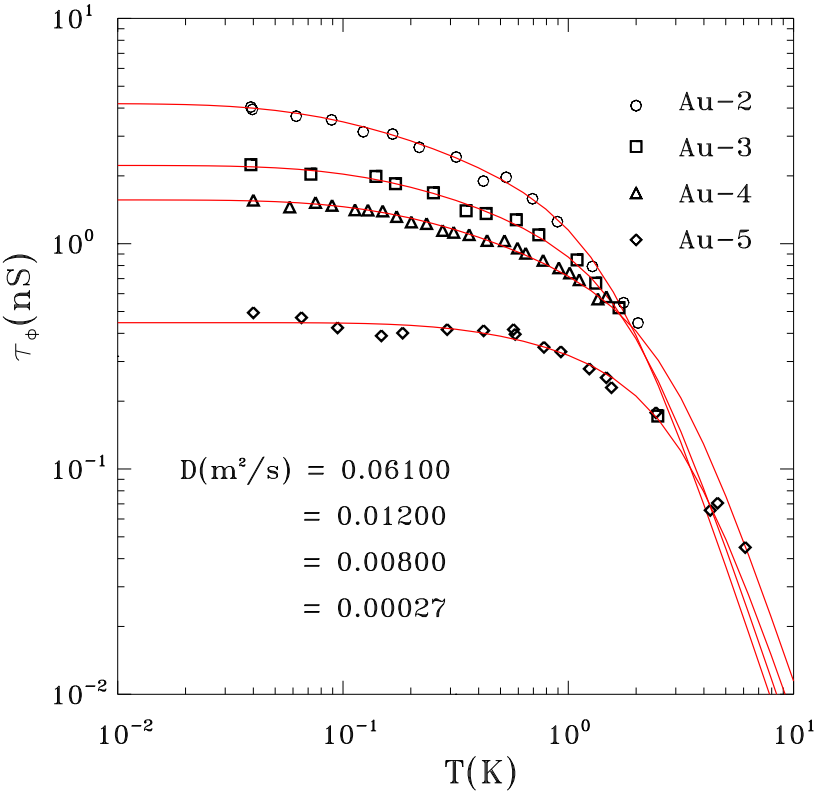

Figure 5.7: Temperature dependence of the phase coherence time $\tau_\varphi \equiv L_\varphi^2/D$ in a series of four disordered Au wires. The topmost trace corresponds to the control meander (Au-2) for our thirty co-fabricated rings, with $D = 0.061\,\mathrm{m}^2/\mathrm{s}$. From this data, we infer that $L_\varphi > L$ in our $8\,\mu$m-long rings and electron transport may be phase-coherent up to temperatures as high as 1 K. The saturation of τ_φ at low temperatures is discussed further in Ref. [23].

Measured parameters	
number N	30 rings
system	Au
shape	circular

Inferred parameters	
mean free path l_e	87 nm
diffusion constant D	$0.061\,\mathrm{m}^2/\mathrm{s}$
phase coherence length L_φ	$\sim 15\,\mu$m

diameter $2a$	$2.56\,\mu$m
width w	110 nm
thickness t	60 nm

mean level spacing Δ	0.019 mK
Thouless energy E_c	7.3 mK
Fermi velocity v_F	$1.4 \times 10^6\,\mathrm{m}/\mathrm{s}$

length L	$8.04\,\mu$m
area $\mathcal{A}$	$5.15\,\mu\mathrm{m}^2$
volume $\mathcal{V}$	$0.053\,\mu\mathrm{m}^3$

current scale $e\Delta/\hbar$	0.0004 nA
current scale $eE_c/\hbar$	0.15 nA
current scale ev_F/L	28 nA

Table 5.1: Essential physical parameters of our thirty-ring sample. We separate the inferred transport parameters from the dimensional values which we directly measure or confirm. The range of corresponding energy scales describing our rings results in a degree of disorder and phase coherence suitable for our persistent current experiment. In the text, we compare the range of current scales to both the flux-sensitivity of our SQUID pickup coil and the overall flux-noise in our SQUID device.

averaging and dividing by the number of rings, this level of ultimate sensitivity in our unique SQUID measurement setup facilitates the investigation of the mechanism of the persistent current, down to the smallest energy scales.

5.3 Sign and Amplitude

The preceding sections on SQUID design and sample fabrication bear directly on the quality of our data and our goal of measuring both the typical and average contributions in the same sample. As stated in Ch. 4, along with this dual sensitivity comes the additional challenge of measuring two independent signals with different periods of oscillation. For extracting the amplitude of each contribution, as well as the sign at zero field, the techniques of Fourier analysis and Bessel-function signal modulation are particularly suited to our experiment.

In this section, we describe our setup of the measurement electronics used to modulate the applied flux at low frequency f and also measure the magnetic response of the Au rings at multiple harmonics of f. Using data from measurement runs at our lowest base temperatures, we demonstrate the determination of the diamagnetic signs of both the h/e and $h/2e$ oscillations at zero field, as well as the mathematical relationship between different harmonics. We compare the outcomes from Fourier analysis of data sets from different harmonics and summarize our results for the magnitudes of the total current in terms of the different contributions I_{1T} and I_{2T}.

5.3.1 Measurement Setup

Even the most carefully engineered SQUID depends on the operating parameters of the SQUID electronics for optimal performance. For setting the bias current i and modulating the SQUID, we utilize an IBM custom-built SQUID electronics box. The standard $\Phi_0/4$ flux-modulation of the SQUID at 100 kHz is applied to the SQUID loop with the aforementioned SQUID field coils, using the half opposite to where the Au rings are placed. In the course of tuning up a SQUID for operation, we adjust the amplitude and dc offset of the 100 kHz modulation, as well as the SQUID bias current (typically $i \approx 14\,\mu$A), to minimize the flux-noise level, as measured at the output of the SQUID controller. For the best SQUID devices at our disposal, such as that used in this experiment, we achieve a noise baseline of $\sim 8 - 16\,\mu\text{V}/\sqrt{\text{Hz}}$ at 2 Hz, as measured with an HP low-frequency spectrum analyzer. Here an output voltage of $3.93\,\mu$V corresponds to a net flux of $1\,\mu\Phi_0$ through the pickup loop.

After placing the tuned-up SQUID in a negative flux-feedback mode (i.e. the flux-locked loop), we proceed to measure the response of the rings. Figure 5.8 shows the electronics setup for modulating the magnetic field at low frequencies (~ 2 Hz) to probe the h/e- and $h/2e$-periodic oscillations. We control the flux ϕ_{dc} through the rings using an HP 3325B synthesizer/function generator, usually set to sweep from end-to-end of the magnetic field range (± 25 G) over a 12-hour period. We set the small flux-modulation amplitude ϕ_{ac} using the primary PAR 124A lock-in at the fundamental frequency f. The sum $\phi_{dc} + \phi_{ac}\sin(2\pi ft)$ is passed through an HP 6826A current-limited power supply to the SQUID controller, then down the cryostat to the SQUID field coils. The counterwound design of the pickup coil nulls out the applied field itself, leaving the SQUID

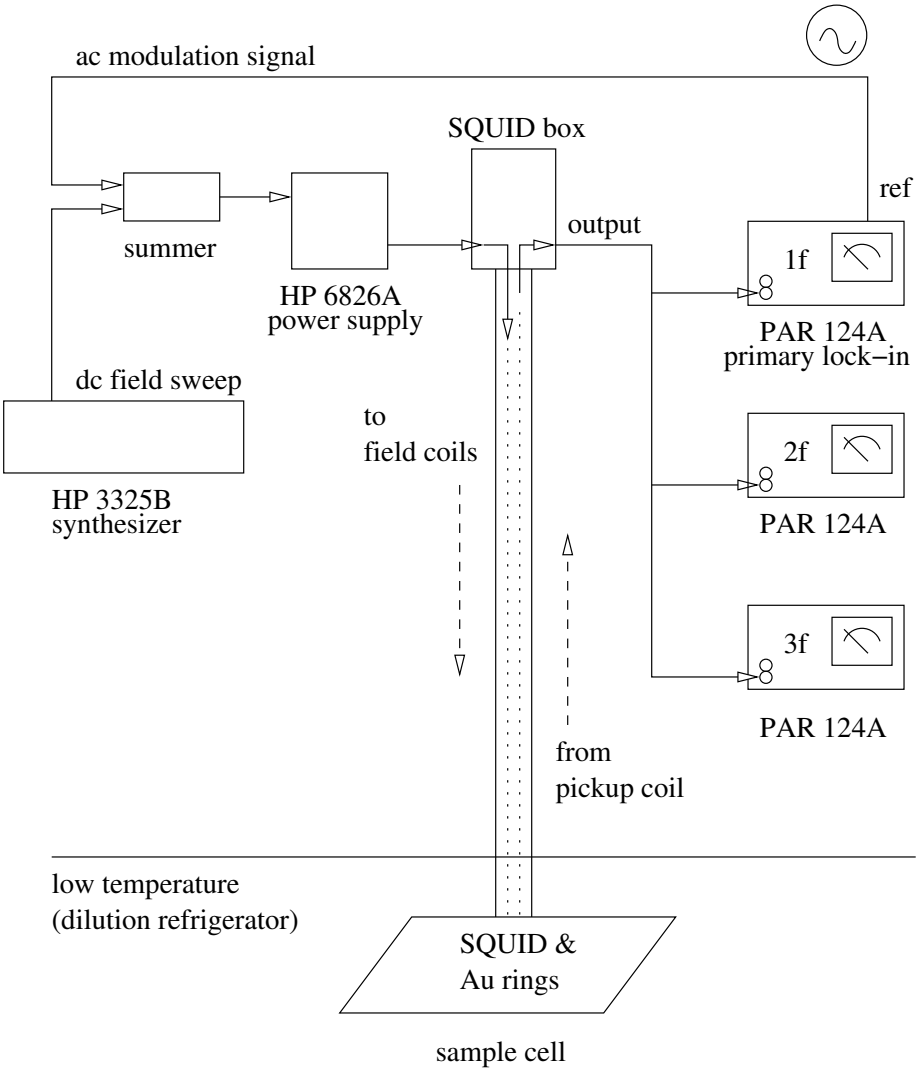

Figure 5.8: Simplified block diagram of the electronics setup for measuring both the h/e and $h/2e$ persistent currents. Using the primary lock-in amplifier, we add a small sinewave signal at frequency f to the slow ramp signal from the synthesizer. With the SQUID pickup coil, we subsequently measure the first three harmonics of the magnetic response of our rings at $1f$, $2f$, and $3f$, as a function of the average applied field. Not shown are the other functions of the multipurpose SQUID box, including the standard $\Phi_0/4$ modulation of the SQUID at 100 kHz.

sensitive only to the response of the rings. From the output signal of the SQUID controller, we isolate the fundamental response at $1f$ with the same lock-in; detecting the higher harmonics at $2f$ and $3f$ requires two more PAR 124A lock-ins triggered at corresponding multiples of the primary lock-in frequency f. As described in Ch. 4, the specific choice of modulation amplitude ϕ_{ac} maximizes a particular Bessel function $J_n(2\pi\phi_{ac}/\phi_p)$ (see Eq. 4.6), bringing out either the $\phi_p = h/e$ or $\phi_p = h/2e$ oscillations in the nth harmonic. Regarding the phase dependence of each harmonic, also shown in Eq. 4.6, we set the phase of the $2f$ and $3f$ lock-ins at 90° and 180°, respectively, with respect to the primary $1f$ lock-in (usually set at 0°). Referring to the counterwound design of our pickup coils and the split-design of our field coils (see Fig. 4.4), the correct phase relationship is preserved at each step in the wiring setup; therefore, for example, a positive slope at zero field in the $2f$ response will always correspond to a diamagnetic sign, due to the minus sign in front of the $f_2 = 2f$ term in Eq. 4.6. This can also be verified empirically in a separate test: by adding a modulation of the phase of the applied field to the present configuration, we can confirm the correct sign of the data at zero field for each harmonic, in response to a large, simulated paramagnetic signal.

5.3.2 Measuring the $h/2e$ Oscillations

A prime example of the need for measuring different harmonics is shown in the three data sets in Fig. 5.9. Taken simultaneously via computer during one slow sweep of the field at $\sim 3.6\,\mathrm{G/hr}$, each harmonic is averaged in 0.08 G bins for over 80 sec per bin. As with most of our data, the modulation frequency $f = 2.02\,\mathrm{Hz}$. A large background magnetization stretching over the entire field

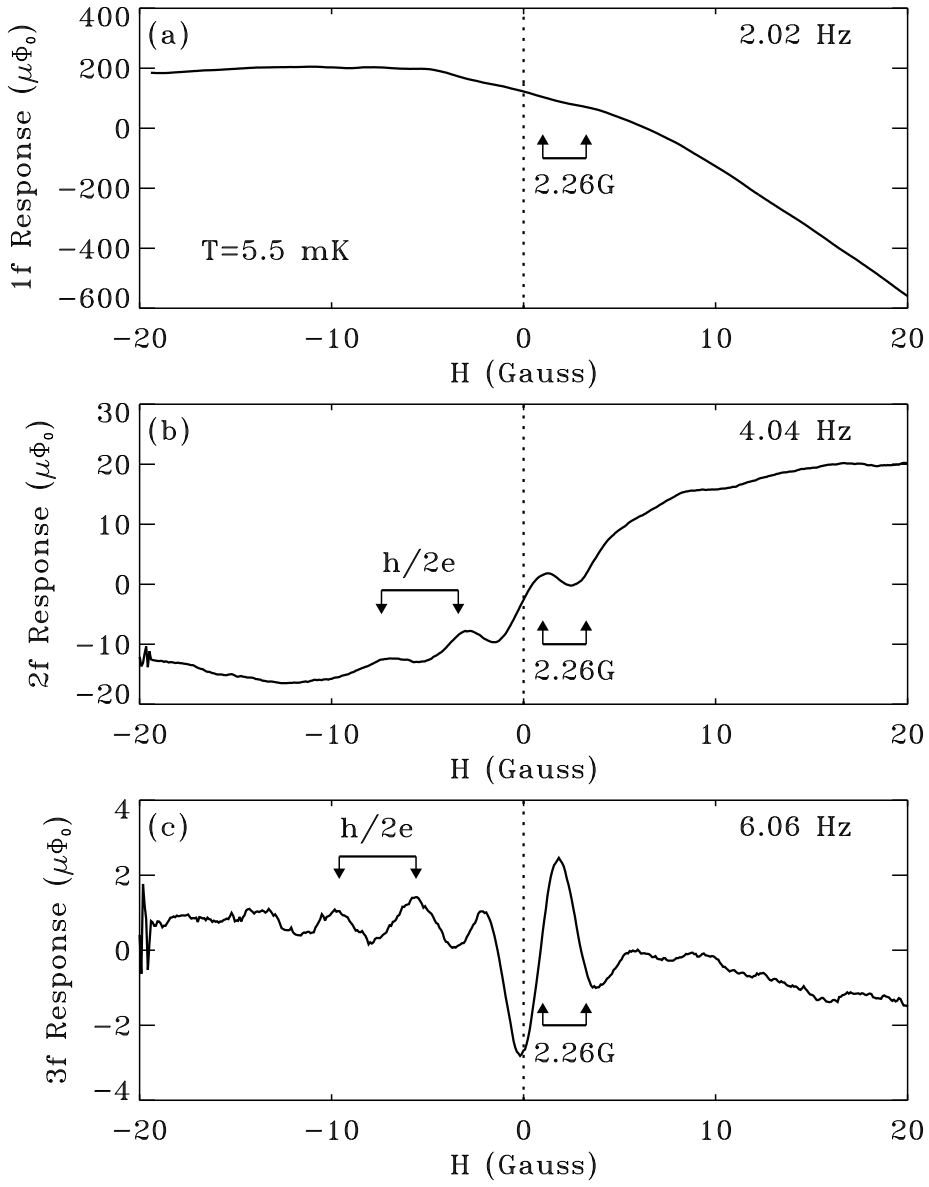

Figure 5.9: Suggestion of the oscillatory signature of the persistent current in the higher harmonics of the magnetic response, before Fourier analysis. A large background magnetization dominates (a) the fundamental response measured at 2.02 Hz; however, both (b) the $2f$ response at 4.04 Hz and (c) the $3f$ response at 6.06 Hz suggest a $\sim 4\,\mathrm{G}$ oscillation indicative of the $h/2e$-periodic current. The modulation amplitude chosen for this run is 2.26 G.

range dominates the fundamental $1f$ response shown in Fig. 5.9(a); any small $\sim \mu\Phi_0$ oscillations with flux-period h/e or $h/2e$ remain hidden. The responses in the higher harmonics at $2f = 4.04\,\mathrm{Hz}$ and $3f = 6.06\,\mathrm{Hz}$, however, clearly show oscillations near zero field; in both Figs. 5.9(b) and (c), we observe oscillations with period $\sim 4\,\mathrm{gauss}$, corresponding to the flux period expected for the $h/2e$ persistent current. Two features of the exact Bessel function relationship described in Ch. 4 can be seen in the data. First, the measured $2f$ response is shown to be an odd function of the field, whereas the $3f$ response is even, as expected from the form of the Bessel equation (Eq. 4.6). Second, considering the sign of the response, the positive upturns of the data near zero field, in comparison to the minus signs that appear in Eq. 4.6, indicate a diamagnetic sign for the response, as discussed in the previous subsection. Though the large $\sim 10^3\,\mu\Phi_0$ background in the fundamental response can be estimated and subtracted, the cleaner signals seen in the higher harmonics provide for immediate evaluation during the experimental runs. Throughout, we have relied upon the either the second or third harmonic data for precise measurements of the amplitude of the persistent current. Remarkably, in all cases, e.g. on multiple cooldowns, the sign of the current remains diamagnetic.

As described in Ch. 4, any h/e- or $h/2e$-periodic components embedded in the raw data show up as distinct peaks at specific locations in the Fourier transform. To illustrate, we focus first on the $2f$ response shown before in Fig. 5.9(b). For this sweep at our base temperature $T = 5.5\,\mathrm{mK}$, we have chosen a zero-to-peak modulation amplitude of $2.26\,\mathrm{G}$ to bring out the $4\,\mathrm{G}$ oscillations of the $h/2e$ current, by maximizing the second-order Bessel function $J_2(2\pi x)$ where $x = (2.26/4.00)$. The raw data is re-plotted in Fig. 5.10(a) (dashed line), after

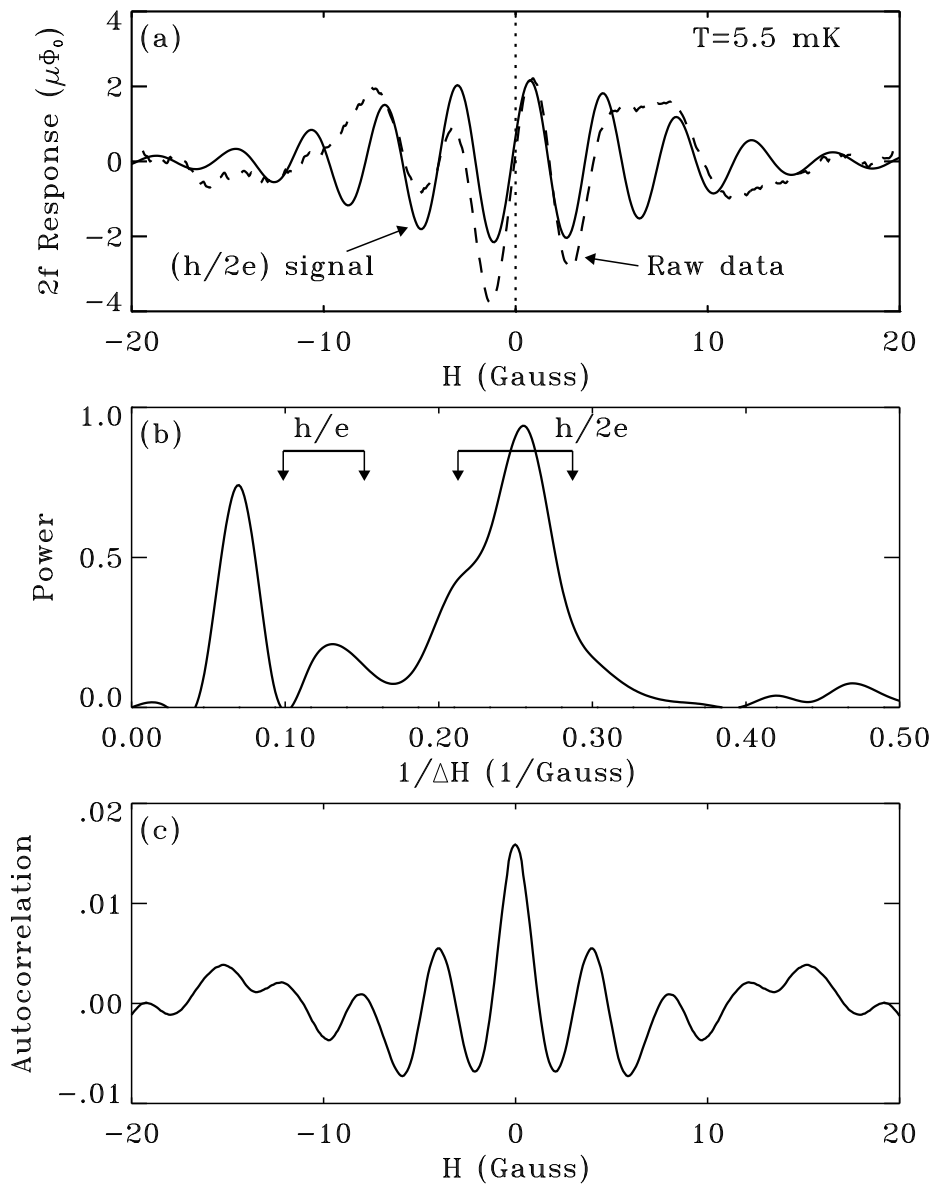

Figure 5.10: Fourier analysis of the $h/2e$-periodic oscillations embedded in the $2f$ response. The dashed line in (a) represents the raw data, after subtracting a polynomial-fit background. The solid line represents the $h/2e$ contribution, taken from the $h/2e$ window in the power spectrum in (b). The $h/2e$-periodic signal is also evident in the autocorrelation in (c).

subtracting a 3rd-order polynomial fit for the background; we also plot the $h/2e$-periodic component of the data (solid line), extracted from the power spectrum shown in Fig. 5.10(b). The width of the h/e and $h/2e$ spectrum windows reflect the finite linewidth of our Au rings; furthermore, the windows are broadened to account for the effect of the intrinsic width of the transform due to the finite field range of the data. We note the $h/2e$-periodic component appears to decrease with increasing field, in a manner similar to weak localization. From solely the $h/2e$ contribution around zero field, then, we estimate a total current of $I_{2T} = 1.98\,\mathrm{nA}$, after dividing by the mutual inductance $\mathcal{M} = 2.7\,\mathrm{pH}$ and accounting for the Bessel dependence reduction factor $J_2(2\pi x) \approx 0.454$. The sign of the response is diamagnetic. We note that the autocorrelation shown in Fig. 5.10(c) also demonstrates the oscillatory component of the data corresponding to the $h/2e$ current.

Though the choice of ac modulation amplitude specifically emphasizes the $2f$ response by maximizing $J_2(2\pi x)$, we can also observe the $h/2e$ oscillations in the $3f$ response, as shown in Fig. 5.9(c). We show the $3f$ response from the same experimental run at $T = 5.5\,\mathrm{mK}$, along with (b) the Fourier transform and (c) the autocorrelation. As before, we fit and subtract a polynomial background from the data; the $h/2e$ component within the window in Fig. 5.11(b) is inversely transformed and plotted (solid line) in relation to the raw data (dashed line) in Fig. 5.11(a). From the $3f$ response, we can make a separate determination of the amplitude of the $h/2e$ current by accounting for the reduction due to the third-order Bessel function factor $J_3(2\pi x) \approx 0.390$, where again $x = (2.26/4.00)$. We find that the total $h/2e$ current as given by the $3f$ response is $1.69\,\mathrm{nA}$, within 20% of the value of $1.98\,\mathrm{nA}$ from above. This small discrepancy results from

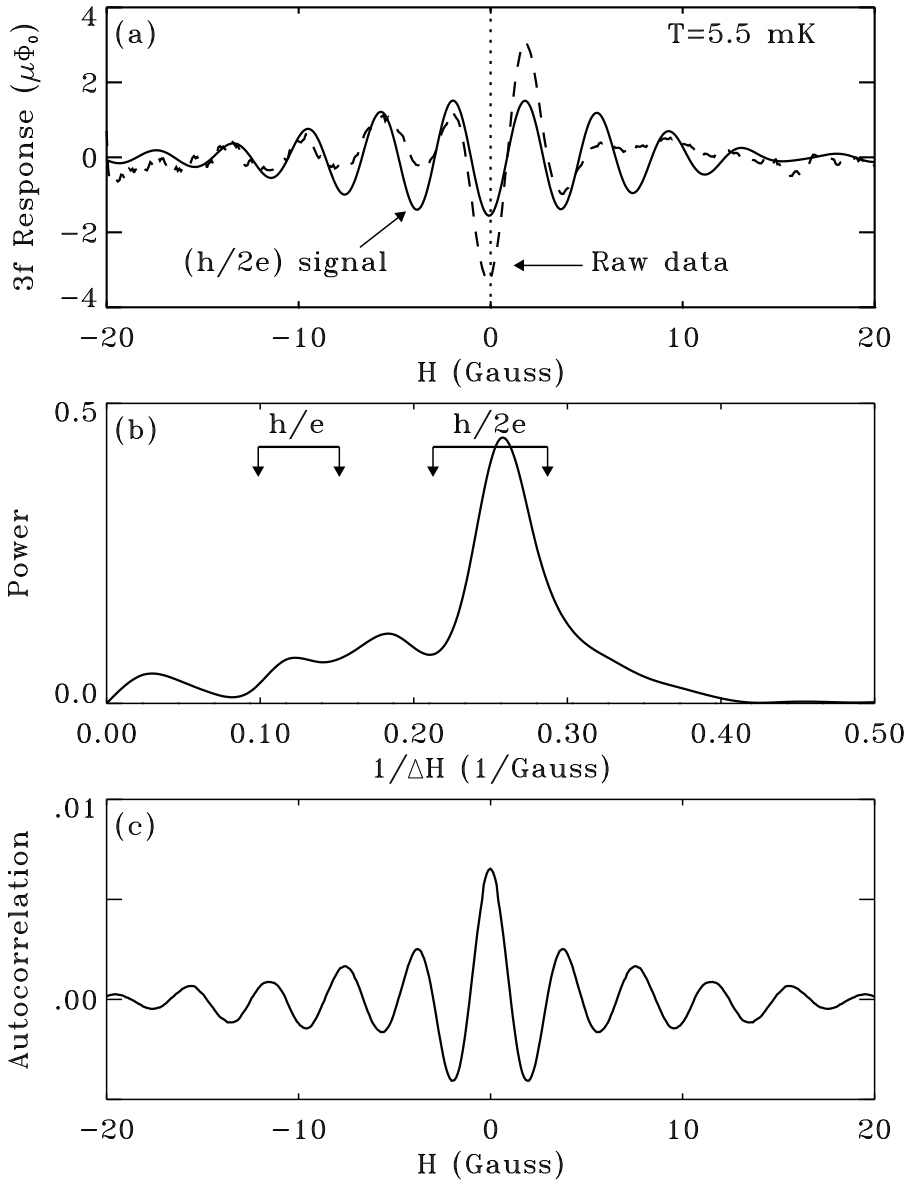

Figure 5.11: Fourier analysis of $h/2e$-periodic oscillations in the $3f$ response, taken simultaneously with the $2f$ data shown previously in Fig. 5.10. Though not optimized by the 2.26 G modulation, the amplitude here agrees with the $2f$ determination to within 20%. The sign determination for this even-function data is identical to that in the odd-function $2f$ data.

our assumption of a sinusoidally varying current, i.e. $I \propto \sin 2\pi\phi/\phi_p$; strictly speaking, the persistent current by definition must only be periodic mod 2π.

For consistency in determining the amplitudes, we subtract the same-order polynomial background from each data set, with some unintended consequences. In both Figs. 5.10(b) and 5.11(b), there seems to be yet another peak in the Fourier spectrum, here shown around $0.07 - 0.08\,\mathrm{G}^{-1}$, that moves if a higher or lower order polynomial background is subtracted. This low-frequency peak results from the finite field range of our data and the background subtraction. The size of our rings has been chosen large enough to avoid confusion of the h/e or $h/2e$ signals with this anomalous peak, along with any other low-frequency response that may be present in our system.

5.3.3 Measuring the h/e Oscillations

As stated in Ch. 4, the Bessel function dependence on the amplitude of the ac field modulation proves essential to distinguishing between the h/e and the $h/2e$ periodic response. Given the finite field range of our measurements, we can expect half the number of h/e versus $h/2e$ oscillations under similar conditions. For the same harmonic, e.g. the $3f$ response, the maximum of $J_3(2\pi\phi_{ac}/\phi_p)$ differs for $\phi_p = h/e$ or $h/2e$. In Fig. 5.12, we show the magnetic response in the three harmonics when using a much larger modulation amplitude at the same base frequency of $f = 2.02\,\mathrm{Hz}$. For this run at $T = 6.3\,\mathrm{mK}$, we again slowly sweep the magnetic field at $3.6\,\mathrm{G/hr}$ and average each data point over a time $t \approx 80\,\mathrm{sec}$. The $h/2e$ oscillations so prominent in Fig. 5.9, however, are not seen in the unprocessed data; the $3f$ response in fact shows one h/e oscillation of period $\sim 8\,\mathrm{G}$, symmetric about zero field. For a modulation amplitude of

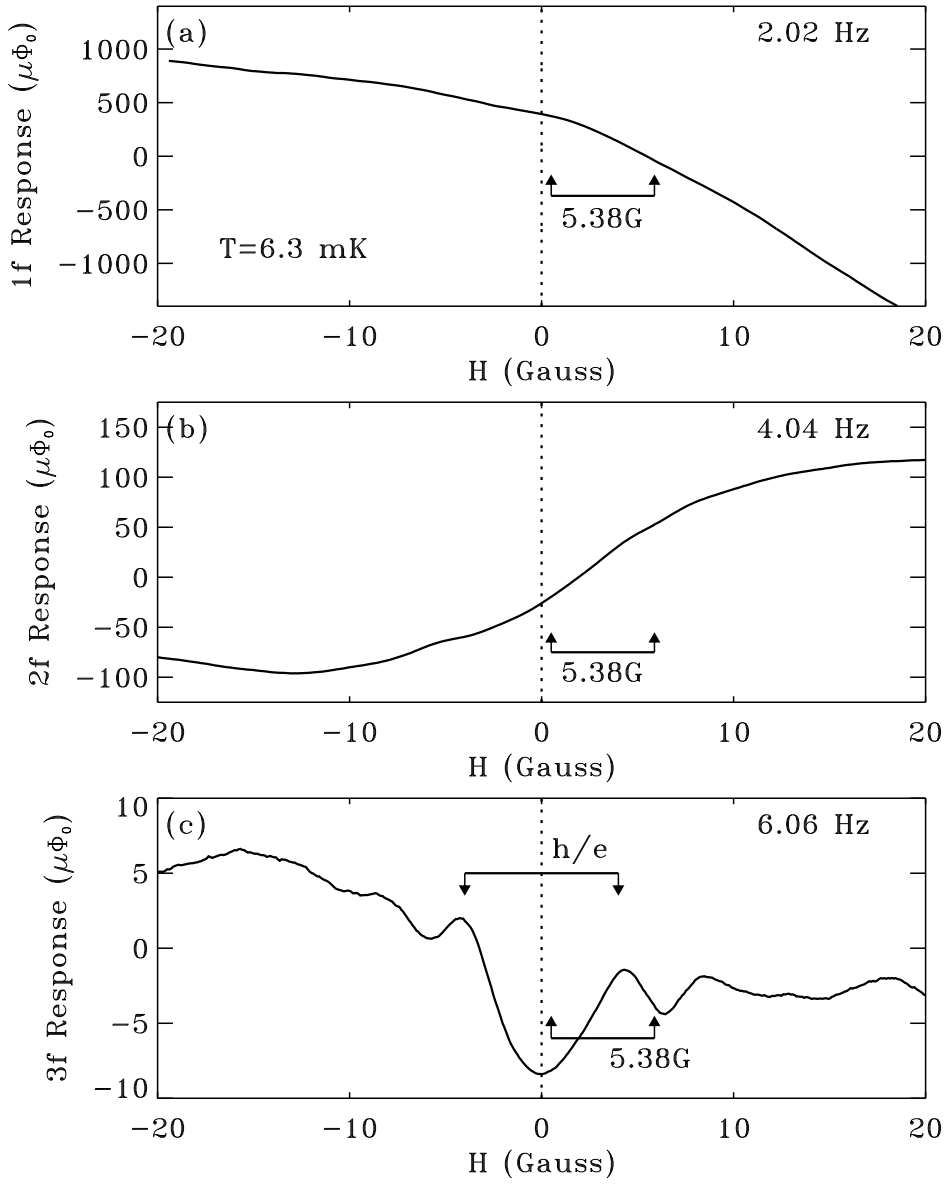

Figure 5.12: Demonstration of the h/e oscillations in higher harmonics of the response, using a larger 5.38 G ac modulation of the applied magnetic field. We again use a low modulation frequency $f = 2.02$ Hz, but with a larger amplitude to accentuate the h/e oscillations by maximizing $J_3(2\pi x)$, where $x = (5.38/8.00)$. The $3f$ response only demonstrates one clear ~ 8 G oscillation indicative of the h/e persistent current.

5.38 G that is more than twice 2.26 G, we find that the h/e component is highlighted in the $3f$ response, given the near maximum of $J_3(2\pi x) = 0.434$, where $x = (5.38/8.00)$.

With the help of background subtraction and Fourier analysis, we improve the h/e signal in the third harmonic data in Fig. 5.12(c). In Fig. 5.13, we show the raw data (dashed line) after background subtraction in (a), as well as the Fourier transform (b) and the autocorrelation (c). As before, we plot the h/e contribution (solid line) in (a) by taking the inverse transform of the bandpassed signal within the h/e window in (b). From this, we determine a total current amplitude of $I_{1T} = 1.92\,\mathrm{nA}$ for the h/e oscillations in the $3f$ response, with diamagnetic sign.

For both the h/e and $h/2e$ oscillations, the exact amplitudes we report depend on some important details of our analysis. The first is the placement of the bandpass windows in the power spectrum for each data set, representing the magnetic field associated with an h/e or $h/2e$ flux quantum through the area of our rings. Though determined consistently for all data sets, we have found that shifting the windows to the right or the left can affect the resulting inverse transform by as much as 20%. Second, in all the data sets, we note that the amplitude of the oscillatory response diminishes away from zero field, leading us to estimate the amplitude by averaging only over the data near zero field, instead of over the entire field range. While an envelope for the $h/2e$ average current may be understood via a theoretical connection to weak localization, an envelope for the h/e typical current is not expected. Moreover, the field scales for the h/e and $h/2e$ envelopes are very similar and not related, for example, by a factor of two.

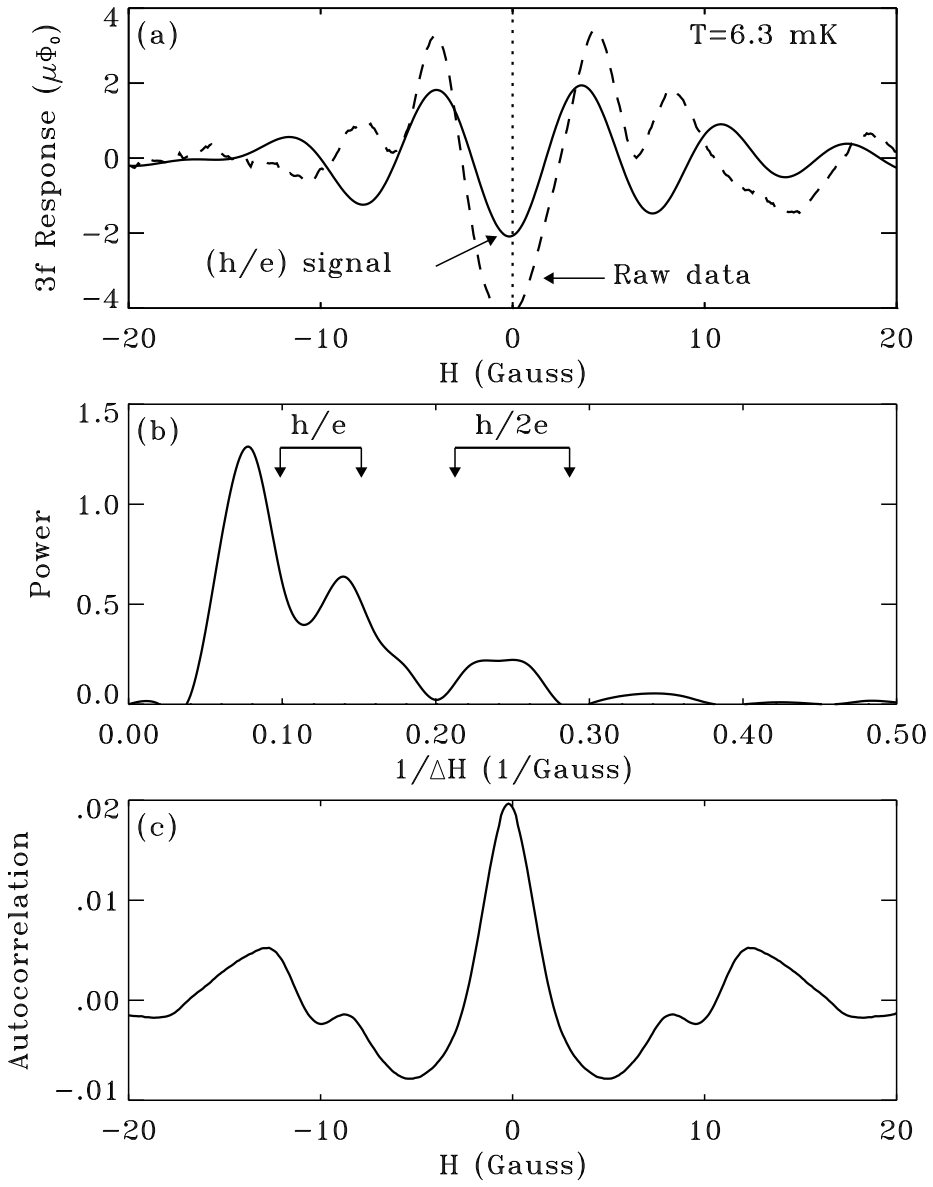

Figure 5.13: Fourier analysis of h/e-periodic oscillations in the $3f$ response. As with other graphs, the dashed line in (a) represents the raw data, after subtracting a sixth-order polynomial-fit background. The solid line represents the h/e contribution, taken from the h/e window in the power spectrum in (b). The 5.38 G modulation has been chosen to maximize this $3f$ response, as given by $J_3(2\pi x)$, where $x = (5.38/8.00)$.

5.4 Temperature Dependence

In the previous Section, we report the maximum amplitudes for both the h/e and $h/2e$ currents, measured at the lowest available temperatures in our dilution refrigerator. In Fig. 5.14(a), we reproduce the data shown above for the $h/2e$ oscillations in the second harmonic ($2f$) at 5.5 mK. We compare that to the data in Figs. 5.14(b) & (c) for the same harmonic, taken at 49 mK and 215 mK, respectively, with the same ac modulation and signal averaging time. No oscillations can be reliably reported at the highest of these three temperatures, even though the Fourier bandpass technique will yield an artificial $h/2e$ or h/e signal for the inverse Fourier transform. Even considering our improvements in SQUID sensitivity and data analysis methods, multiple measurement runs from 215 mK up to 500 mK fail to reveal any trace of the persistent current, despite the measurement of a temperature independent τ_φ for the control meander in this temperature range (see Fig. 5.7). As a consequence, we are restricted to less than two orders of magnitude in temperature dependence for evaluating the $h/2e$ or h/e oscillations. In Table 5.2, we summarize the results for the sign and amplitude of the h/e and the $h/2e$ currents at our base temperatures of $T \approx 5.5 - 6.5\,\mathrm{mK}$, along with a possible fit to an exponential temperature dependence, given the limited temperature range of our measurements. In Ch. 6, we compare these results to the other experiments, as well as to the various theoretical predictions.

Before moving ahead to more general comparisons, we note that the temperature dependence of our data warrants some additional consideration. In Fig. 5.15, we show the combination of data from several cooldowns for the temperature dependence of both contributions from our array. At higher temperatures, the

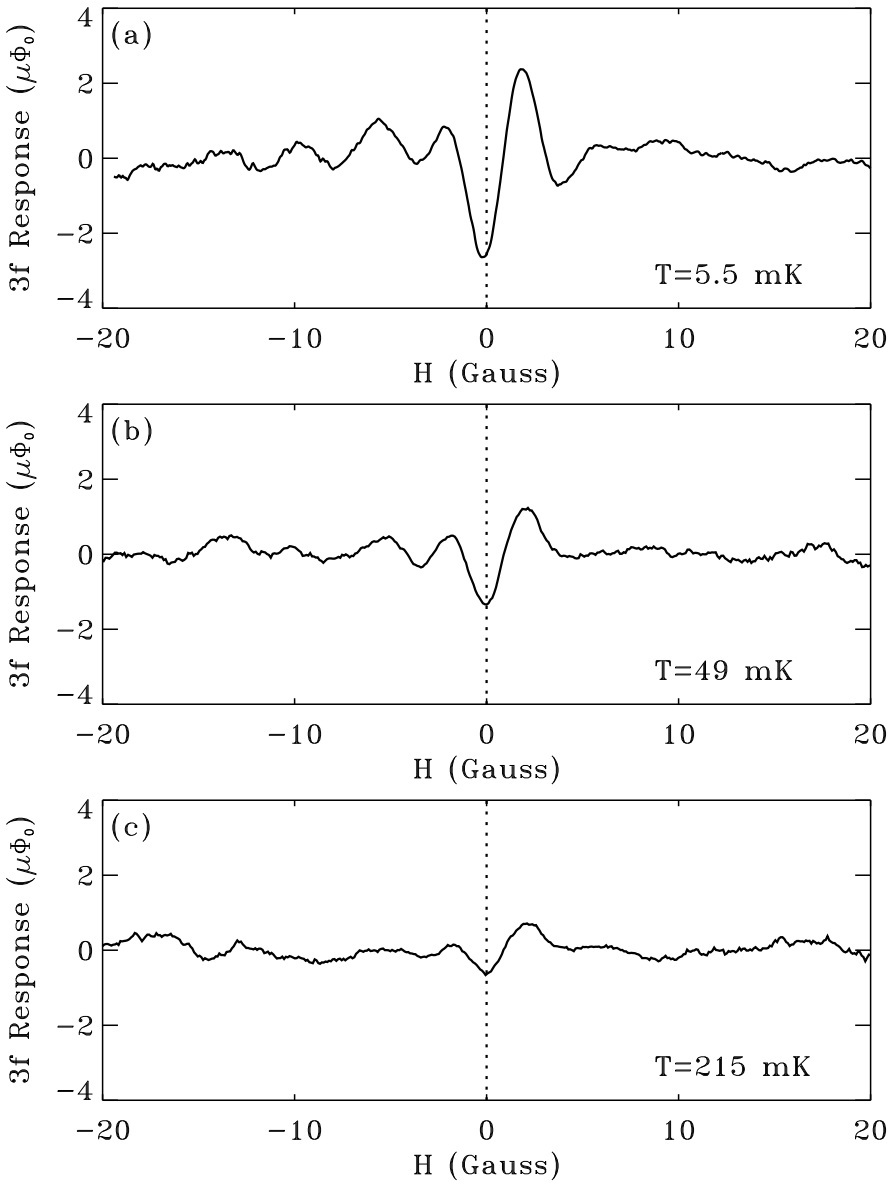

Figure 5.14: Comparison of experimental runs at different temperatures, looking for $h/2e$ oscillations in the third harmonic data, before Fourier analysis: (a) at 5.5 mK, (b) at 49 mK, and (c) at 215 mK. Despite multiple measurement runs at temperatures up to 500 mK, no reliable oscillations can be reported from 215 mK on up. In all three cases, the applied magnetic field is modulated at 2.02 Hz with an amplitude of $\sim 2\,$gauss.

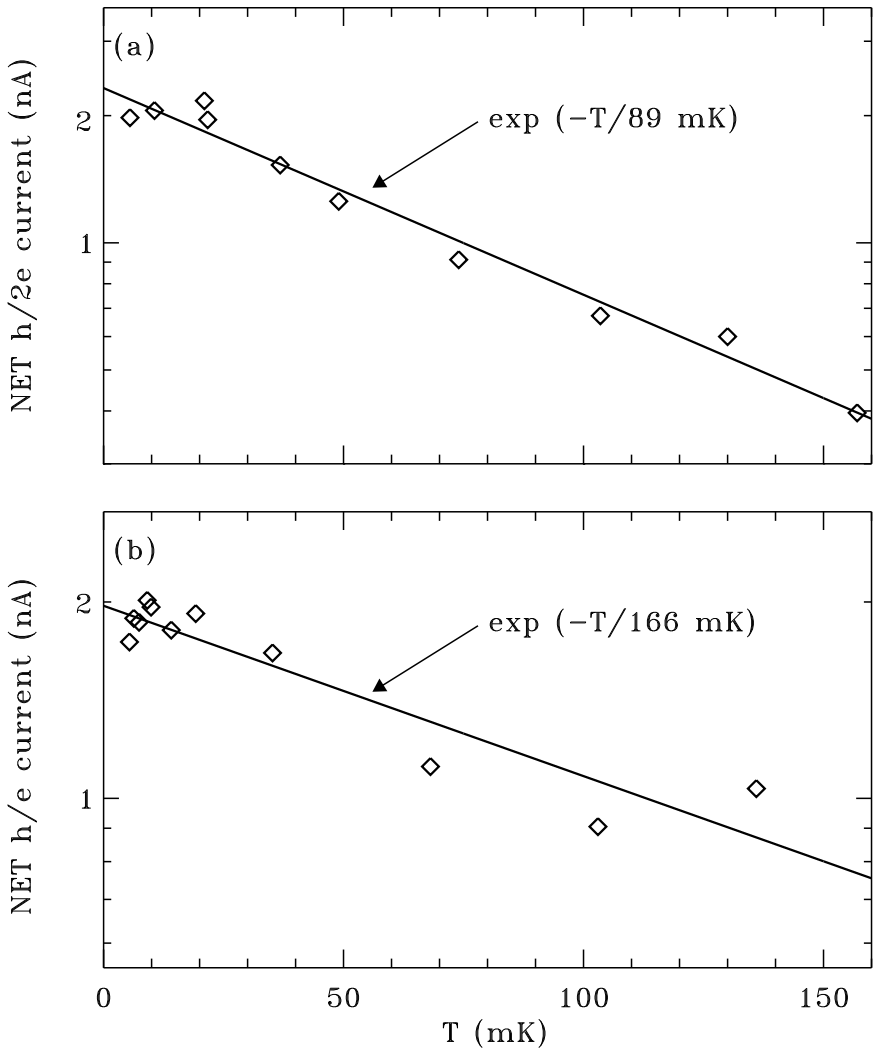

Figure 5.15: Temperature dependences of the total $h/2e$ and h/e currents calculated from the net magnetic response of the 30 Au rings. The solid lines represent weighted fits to the form $\exp(-T/T_0)$. The characteristic temperature T_0 for the $h/2e$ data is close to half of that for the h/e data.

Experiment		I_{1T} (h/e period)				I_{2T} ($h/2e$ period)			
N	system	per	sign	ampl	temp	per	sign	ampl	temp
30	Au	h/e	dia	1.92 nA	$e^{-T/166}$	$h/2e$	dia	1.98 nA	$e^{-T/89}$

Table 5.2: Summary of our results for the sign and amplitude of the total currents I_{1T} and I_{2T} at lowest temperatures, along with possible exponential fits for the temperature dependence up to $\sim$ 200 mK. We discuss these results in more detail in Ch. 6.

lower signal-to-noise ratio limits the precision of our amplitude determinations. We thus show weighted fits to the form $\exp(-T/T_0)$, with $T_0 = 89$ mK for the stronger temperature dependence of the $h/2e$ current about half the $T_0 = 166$ mK for the h/e current. Above the temperature range shown, no reliable signal appears above the level of the flux-noise.

The narrow temperature range of our data, however, allows for other interpretations. In Fig. 5.16, we replot the same data from Fig. 5.15 as a function of $\sqrt{T}$ instead of T. At higher temperatures, we see that the part of the data sets follow the alternate exponential form of $\exp(-\sqrt{T/T_0})$, with T_0 for the stronger $h/2e$ dependence similarly half of that for the h/e. Plotted this way, however, both sets of data demonstrate a knee around 20 mK, indicative of a saturation of the signal. Assuming this feature is significant and not solely plot-dependent, we envision two possible scenarios.

The first scenario suggests the saturation effect is physical – more specifically, due to some electronic interaction or electron level correlation on the energy scale of 20 mK. In a previous experiment [4], the measured h/e-periodic typical

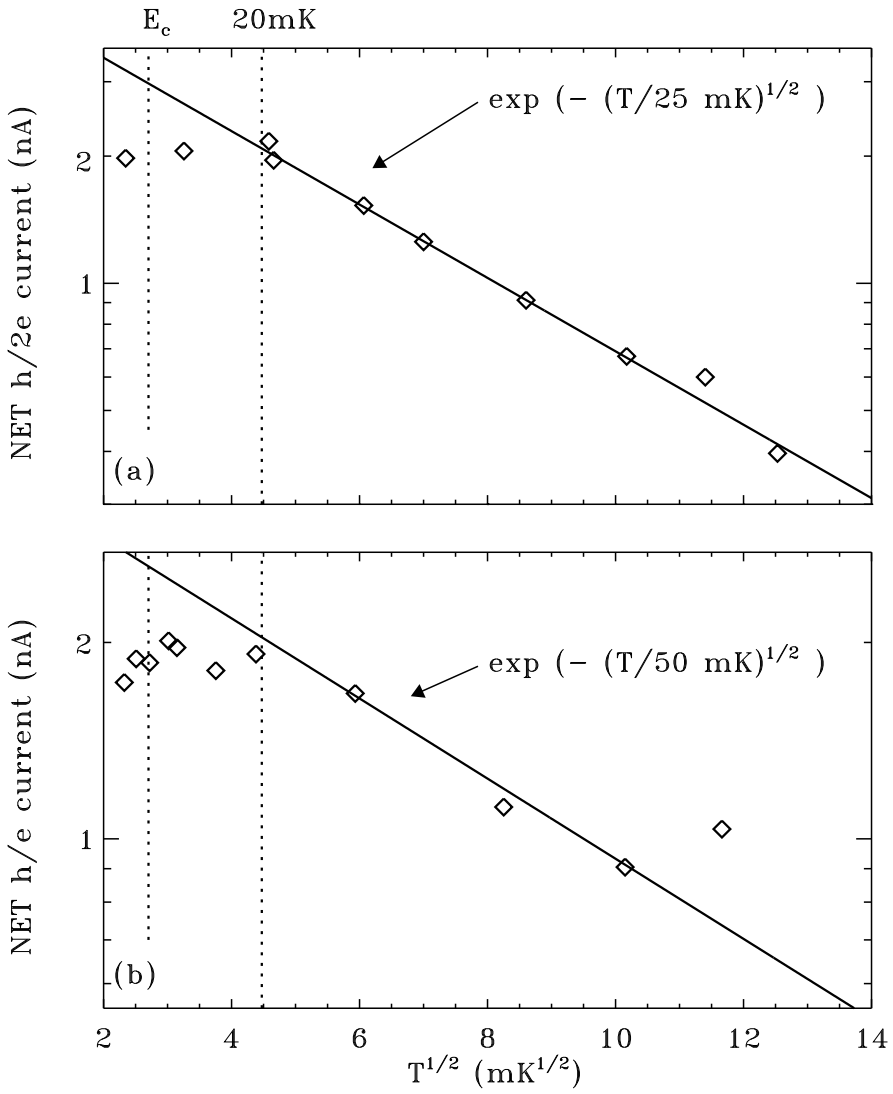

Figure 5.16: Alternate graphs of the temperature dependences of the total $h/2e$ and h/e currents, plotted versus $\sqrt{T}$ instead of T. Over the limited temperature range of our measurement, the data follows the form $\exp(-\sqrt{T/T_0})$, with T_0 for the stronger $h/2e$ dependence similarly half of that for the h/e. Plotted this way, however, both sets of data appear to saturate below 20 mK, above our calculated Thouless temperature of $E_c \approx 7.3$ mK.

current in two separate rings, when plotted as a function of $\sqrt{T}$, demonstrated a saturation below 10 mK, which corresponds with the Thouless scale E_c calculated for those rings. For our results, the agreement is not as apparent: the saturation temperature of 20 mK is almost three times the Thouless energy $E_c \approx 7.3$ mK. Moreover, any necessary adjustment to our inferred value of E_c would suggest a persistent current amplitude much larger than measured.

The second scenario does not provide any clearer answers, but does stem from a familiar concern of all low-temperature physicists: what is the actual temperature of my sample? In the Ch. 7, we discuss the calibration process and the limitations of the thermometers used to measure the helium bath temperature in the sample cell, as well as our independent experimental efforts to determine the internal temperature of the electrons in this class of quasi-1D mesoscopic Au systems with weak disorder.

Chapter 6

Discussion

Upon review, the set of results we presented in Ch. 5 has significant impact on our understanding of the persistent current problem. In this Chapter, we discuss the specific contributions of our new measurements of the h/e and $h/2e$ oscillations and make individual comparisons with the four original experiments [2, 4, 5, 7]. We also consider the agreement of our results within the theoretical frameworks of competing descriptions for the sample-specific and the ensemble-average contributions to the response [32–40]. Of particular importance is how our new measurements affect the existing experimental challenges to conventional theories. With regards to the broader objectives outlined in Ch. 4, we also discuss the more fundamental questions raised by our results.

6.1 Experimental Comparison

We begin by comparing the specific physical details of our actual Au sample with the six different samples from the original experiments [2, 4, 5, 7]. Table 6.1 lists the relevant dimensional and energy scales for each, as also described before in Tables 4.1 and 5.1. For completeness, we have also included the details for

Experiments			L	L_φ	l_e	Δ	E_c	$e\Delta/\hbar$	$eE_c/\hbar$	ev_F/L
N	system	shape	(μm)	(μm)	(μm)	(mK)	(mK)	(nA)	(nA)	(nA)
1	GaAs	circ	8.3	25	11	32	159	0.67	3.33	5.2
1	Au	circ	12.6	12	0.07	0.016	4.78	0.00033	0.10	18
1	Au	circ	7.5	12	0.07	0.027	13.2	0.00056	0.28	30
1	Au	rect	8.0	12	0.07	0.025	11.8	0.00052	0.25	28
16	GaAs	sq	12	20	8	4.4	134	0.09	2.8	4.2
30	Au	circ	8.0	15.6	0.09	0.019	7.3	0.00040	0.15	28
10^5	GaAs	sq	8	7	3	8.2	33	0.17	0.67	3.6
10^7	Cu	sq	2.2	2.57	0.03	0.31	24.8	0.0065	0.52	102

Table 6.1: Comparison of our sample set to the metallic or semiconducting rings from other experiments. Though intermediate in number ($1 < N << \infty$), our $N = 30$ Au rings are close to the majority of sample sets in both size (L) and phase coherence length ($L_\varphi > L$). The fortuitous similarities in energy scales (Δ and E_c) and corresponding scales for a persistent current ($e\Delta/\hbar$, $eE_c/\hbar$, and ev_F/L) form the basis for comparing our results to previous measurements, particularly for the case of diffusive systems with weak disorder. For completeness, we also include the 16-ring GaAs sample from a new experiment (Ref. [10]) that followed our own work.

a 16-ring GaAs sample from a new experiment (Ref. [10]) that followed our own work. Aside from the essential difference in ensemble number, our sample resembles the others in many ways, of order $L \sim 10\mu$m in circumference and with a similar phase coherence length $L_\varphi \geq 10\mu$m. Though different by nature from the GaAs-AlGaAs rings with nearly-ballistic electrons ($l_e \geq L$), our metallic Au rings are quite comparable to the other Au or Cu samples, in terms of electron diffusion ($l_e << L$) as well as disorder ($1 << k_F l_e \leq 1000$). Consequently, for the sample sets with metallic rings, we can qualitatively summarize the relevant energy scales as

$$\Delta \geq 10\,\mu\text{K and } E_c \sim 10\,\text{mK} \tag{6.1}$$

and the associated current scales as

$$\frac{e\Delta}{\hbar} \sim 0.0004 \text{ nA}, \frac{eE_c}{\hbar} \sim 0.2 \text{ nA, and } \frac{ev_F}{L} \sim 10 \text{ nA}. \tag{6.2}$$

Though perhaps due more to fabrication constraints, the overall similarity of the sample sets allows for comparing results from separate experiments as well as relating the different energy scales of the problem.

As shown previously in Table 5.2, at our lowest temperature of 5.5 mK, the amplitudes of the total h/e and $h/2e$ currents from all thirty rings are $I_{1T} = 1.92$ nA and $I_{2T} = 1.98$ nA. For comparison to different experiments, we must distinguish between the current *per ring* and the total current response from the whole array. As described in our proposal (see Eq. (4.1)), we have chosen an intermediate number $N = 30$ of rings in order to explore both the typical and average contributions in the same array. Therefore, as with the other two experiments in multiple-ring arrays, we divide the total $h/2e$ response by N to give the average current $I_{\text{av}} = \langle I_2 \rangle$ per ring; however, for comparing to the

single-ring measurements, we must divide the total h/e response by $\sqrt{N}$ to yield the typical current $I_{\rm typ} = \sqrt{\langle\, I_1^2 \,\rangle}$ per ring. For our experiment, then, we calculate $I_1 = I_{1T}/\sqrt{30} = 0.35\,\mathrm{nA}$ and $I_2 = I_{2T}/30 = 0.066\,\mathrm{nA}$, respectively, per ring. Though other choices are certainly possible, these are decidedly more speculative for the persistent current problem.

The left side of Table 6.2 lists the results for the measured amplitude of the h/e-periodic response at lowest temperatures, along with the measured sign and temperature dependence, where available. For comparison to the results from a single Ga-As ring [5], individual Au rings [4], or sixteen Ga-As square loops [10] (measured at 15 mK, 4.5 mK, and 20 mK, respectively), we present the amplitudes in terms of ev_F/L (see Table 6.1). Our amplitude per ring of $I_1 = 0.025\,ev_F/L$ at 6.3 mK is remarkably 10–40 times smaller than these other measurements, including those in single gold rings of similar dimension and disorder. In addition, we measure a net diamagnetic sign for the total h/e response, in contrast to the paramagnetic sign seen before in two different Au samples. We emphasize that these results are not necessarily inconsistent, given the sample-specific nature of the h/e-periodic typical current as a fluctuation effect, with random sign and zero mean. Comparing temperature dependences in terms of $e^{-\sqrt{T/T_0}}$, our h/e signal falls off less quickly, again in comparison to that in similar Au rings [4]. As mentioned earlier, we also see a similar saturation of the h/e data at low temperatures when plotted as a function of $\sqrt{T}$, but at a temperature almost three times larger than the Thouless energy $E_c \approx 7.3\,\mathrm{mK}$ of our rings. Though distinctly different, our results provide significant, complementary evidence for a problem investigated only twice previously.

The right side of Table 6.2 lists the results for the $h/2e$-periodic response,

Experiments			$I_{\text{typical}} \equiv \sqrt{\langle I_n^2 \rangle}$				$I_{\text{average}} \equiv \langle I_n \rangle$			
N	system	[Ref]	per	sign	ampl	temp	per	sign	ampl	temp
1	GaAs	[5]	$\frac{h}{e}$	– ? –	$0.77\,\frac{ev_F}{L}$	– ? –				
1	Au	[4]	$\frac{h}{e}$	– ? –	$0.17\,\frac{ev_F}{L}$	– ? –				
1	Au	[4]	$\frac{h}{e}$	para	$1.0\ \frac{ev_F}{L}$	$e^{-\sqrt{\frac{T}{4.8}}}$				
1	Au	[4]	$\frac{h}{e}$	para	$0.21\,\frac{ev_F}{L}$	$e^{-\sqrt{\frac{T}{4.8}}}$				
16	GaAs	[10]	$\frac{h}{e}$	– ? –	$0.33\,\frac{ev_F}{L}$	– ? –				
30	Au	[9]	$\frac{h}{e}$	dia	$0.025\,\frac{ev_F}{L}$	$e^{-\sqrt{\frac{T}{50}}}$	$\frac{h}{2e}$	dia	$0.35\,\frac{eE_c}{\hbar}$	$e^{-\frac{T}{89}}$
10^5	GaAs	[7]					$\frac{h}{2e}$	dia	$2.24\,\frac{eE_c}{\hbar}$	$e^{-\frac{T}{190}}$
10^7	Cu	[2]					$\frac{h}{2e}$	– ? –	$0.77\,\frac{eE_c}{\hbar}$	$e^{-\frac{T}{80}}$

— *not measured* —

Table 6.2: Comparison of our results to other measurements from single rings or multiple-ring arrays. We denote the amplitudes of the current oscillations in terms of either ev_F/L or $eE_c/\hbar$, instead of nA, and provide the sign and temperature dependence, where available. Regarding the h/e-periodic oscillations, we measure an amplitude per ring of $I_1 = 0.025\,ev_F/L$ that is 10–40 times smaller than seen previously and notably diamagnetic in sign. Given the random sign and sample-specific nature of the typical current, these results are not inconsistent. Regarding the $h/2e$-periodic oscillations, our measured amplitude of $I_2 = 0.35\,eE_c/\hbar$ agrees to within a factor of 2 with the sole other measurement in metallic rings, while adding a diamagnetic sign determination to complement that seen in quasi-ballistic rings.

including the measured sign and temperature dependence, where available. For comparison to the ensemble-averaged current measured in either 10^5 Ga-As [7] or 10^7 Cu [2] square loops (measured at $\sim$ 50 mK or extrapolated to $T = 0$, respectively), we present the amplitudes per ring in terms of $eE_c/\hbar$. (Though Ref. [2] is the only experiment to present its findings at $T = 0$ based on a fit to e^{-T/T_0}, the difference at actual base temperatures is less than 10%.) In our array of disordered Au rings, we measure an $h/2e$ signal of $I_2 = 0.35\, eE_c/\hbar$ per ring at 5.5 mK, only a factor of two smaller than seen in the array of disordered Cu rings. Importantly, we measure a diamagnetic sign for the total $h/2e$ response, which was left undetermined for the Cu rings. Our agreement with this sole other experiment on metallic rings extends to the exponential temperature dependence e^{-T/T_0}, with both yielding characteristic temperatures of $T_0 \approx 80-90$ mK despite the differences in size and disorder of the respective samples. In comparison to the larger result from the Ga-As rings, again in a quasi-ballistic instead of a diffusive system, we at least note an agreement in the diamagnetic sign of the response. We add that the new experiment on the h/e current in a small array of 16 GaAs rings [10] fails to measure the $h/2e$ current altogether.

On the whole, our combined set of results fit nicely within the framework of existing experiments, with no apparent contradictions or grave inconsistencies. In particular, the resulting combination of data for the sign and amplitude of the $h/2e$ current points strongly towards the need for better theoretical understanding, to be discussed below. Regarding the additional information to be deduced from the measured temperature dependences, we note that the number of such data sets has nearly doubled as the result of our efforts.

6.2 Theoretical Understanding

In Ch. 3, we have identified specific points of disagreement between previous experimental results and the major theoretical calculations for the persistent current. Here we compare our new results to the range of predictions for both the typical current $\sqrt{\langle I^2 \rangle}$ and the ensemble-average current $\langle I \rangle$. Taken in conjunction with earlier experiments, our new results: (i) reveal new insights into the sample-specific nature of the typical current and also (ii) augment the experimental challenge to several conventional theories of the average current.

In our recap of theories of the persistent current in Ch. 3, we described a host of different calculations, depending on whether the canonical or grand-canonical ensemble is used, or whether electron-electron interactions are included. In all calculations, however, the results for the typical current are the same – on the order of the Thouless energy E_c, and either paramagnetic or diamagnetic in sign. Specifically, we recall Eq. 3.6:

$$\langle I_m^2 \rangle = 4 \times \frac{96}{(2\pi)^2 m^3} \left(\frac{eE_c}{\hbar} \right)^2 \left[1 + \frac{m}{2} \frac{L}{L_\varphi} + \frac{m^2}{3} \left(\frac{L}{L_\varphi} \right)^2 \right] e^{-mL/L_\varphi} , \tag{6.3}$$

which yields (using $L/L_\varphi \approx 1/2$):

$$\sqrt{\langle I_1^2 \rangle} = 2.8 \left(\frac{eE_c}{\hbar} \right) \tag{6.4}$$

for the first harmonic ($m = 1$) of the typical current. This prediction agrees very well with our result of a diamagnetic sign and an amplitude of:

$$I_1 = 0.35\,\mathrm{n}A = 2.3 \left(\frac{eE_c}{\hbar} \right) \tag{6.5}$$

Given the limited range of our data, a comparison of our fit of $e^{-\sqrt{T/50}}$ to the predicted temperature dependence of $e^{-\sqrt{T/7.3}}$ (since $E_c = 7.3$ mK for our sample) may not be especially useful for theorists; however, the weaker temperature

dependence does indicate that we are able to measure an h/e current at much higher temperatures than expected.

In addition to yielding good agreement with the calculated value for the amplitude of the typical current, we also provide a reference point for comparing to sample-specific results from other experiments in disordered systems, such as in Ref. [4]. Our results for the h/e contribution also confirm that a random sign is possible for the typical current, since we measure a diamagnetic sign where only paramagnetic sign had been seen previously. Unfortunately, the weak temperature-dependent data cannot distinguish between different predictions for exponential functional form or energy scale dependence. But overall, our results fit well into the framework for the typical current.

The same cannot be said for our results for the average current. In Ch. 3, we outlined the two major competing theories for the average current $\langle I_2 \rangle$, with $h/2e$ flux periodicity. Both strictly require a paramagnetic sign, with predicted amplitudes of either:

$$\langle I_2 \rangle = \frac{4}{\pi} \left(\frac{e\Delta}{\hbar} \right) \tag{6.6}$$

for noninteracting electrons [39], or:

$$\langle I_2 \rangle = 0.2 \left(\frac{eE_c}{\hbar} \right) \tag{6.7}$$

for interacting electrons [35]. Neither of these predictions can account for our measurement of a diamagnetic sign and a much larger amplitude of:

$$I_2 = 0.066\,\mathrm{n}A = 0.44 \left(\frac{eE_c}{\hbar} \right) \tag{6.8}$$

Furthermore, the two predicted temperature dependences of $e^{-\sqrt{T/T_0}}$ and $e^{-T/3T_0}$, respectively, (where $T_0 = E_c = 7.3$ mK for our sample) are much stronger than

what is actually observed: we can fit our $h/2e$ data to either $e^{-\sqrt{T/25}}$ or $e^{-T/89}$, as described in Ch. 5.

We point out here that the prediction of $\sim 0.2\, eE_c/\hbar$ for interacting electrons approaches our result (within a factor of 2), but the sign is required to be paramagnetic [35]. Substituting an attractive phonon-mediated interaction yields the correct diamagnetic sign but reduces the amplitude by an order of magnitude [46]. Given the prominence of the e-e interaction calculation in the literature on persistent currents, we must reiterate here that this theory cannot account for our results – in sign, amplitude, or temperature dependence.

The significant gap between theory and the set of $h/2e$ persistent current experiments has prompted theorists to look elsewhere for a solution. One recent suggestion [40] connects the ensemble-averaged $h/2e$ current $\langle I_2 \rangle$ to the intrinsic dephasing time τ_0 at $T = 0$ [23], via a universal relationship $\langle I_2 \rangle = Ce/\tau_0$ (where the constant C of order 1 also contains the sign). Estimating $\tau_0 = 4.2$ ns [23] and accounting for strong spin-orbit scattering in our gold rings, this formula yields a value of 0.025 nA but paramagnetic in sign, as compared to our diamagnetic measurement of 0.066 nA per ring. For larger arrays of rings with weaker spin-orbit scattering, this new idea appears to give the correct $h/2e$ amplitude based on τ_0 [2,7], as well as the observed diamagnetic sign [7]. Though interesting in concept and consistent with the amplitudes measured in multiple-ring experiments, this new theory fails to account for the sign in all cases. In this light, by adding the sign determination for diffusive gold rings and providing a comparison for the temperature dependence, our new results seem especially helpful in reinforcing the strong experimental challenge to existing theories of the average current.

6.3 Exploring Frontiers

As discussed in previous Chapters, the persistent current problem fits into a larger context of mesoscopic phenomena at the nanoscale level. Measuring the magnetic response and other thermodynamic properties is less common and arguably more difficult than measuring transport phenomena, but the field in general presents an equally important opportunity for exploring the physics of systems of nanoscale dimensions.

With regards to decoherence in general, the persistent current is a probe of the low-lying states of the phase coherent wavefunctions of the conduction electrons. But, as opposed to transport measurements, there are no leads to drive the current, nor pads to act as electron reservoirs. Fabricated atop an insulating SiO_x/Si substrate, the rings in our experiment are electrically isolated from electron reservoirs or other external sources of dephasing. In essence, the mere presence of a persistent current signal is direct evidence of the correlation of electron wavefunctions in a phase coherent system. By virtue of measuring anything at all, we provide an independent measurement of the coherent electron wavefunctions near the zero-temperature ground state, distinctly separate from the non-equilibrium measurements of weak localization or conductance fluctuations.

Moreover, as discussed at the end of Ch. 4, our work on the persistent current problem addresses the nature of self-averaging in mesoscopic systems. In single-rings, the h/e contribution to the typical current is the dominant signal; in multiple-ring arrays, any signal from the h/e typical current (which grows as $\sqrt{N}$) is overwhelmed by the $h/2e$ average current (which grows as N). But, in our ensemble comprised of an intermediate number $N = 30$ of rings, we have measured both the typical and average contributions to the persistent current

in the same sample and, in turn, highlighted the distinction in mesoscopics between the average value over an ensemble and the typical value varying from one member to another. The situation for this thermodynamic property:

$$\langle I^2 \rangle \neq \langle I \rangle^2 \tag{6.9}$$

parallels that from mesoscopic transport experiments:

$$\langle G^2 \rangle \neq \langle G \rangle^2 \,, \tag{6.10}$$

as discussed in Ch. 2. In this manner, an experimental demonstration of the difference between the typical value and the ensemble-average value of the persistent current identifies the self-averaging principle of thermodynamic quantities as truly mesoscopic in nature.

Chapter 7

Cross-checks

For any one experiment, a thorough cross-examination of the results often leads to even more experiments, sometimes along entirely new avenues of investigation. In this Chapter, we describe our efforts to answer the questions surrounding the high-frequency environment as well as the temperature dependence in our persistent current experiment. The result is two separate and novel measurements: one on the possible dephasing effects of SQUID back-action and the other on the Johnson noise temperature of our samples. Interestingly enough, both capitalize on our experience with using SQUIDs, and both investigate some aspect of noise in mesoscopic systems.

7.1 SQUID Back-action

The specialized pickup coil used for our persistent current experiment provides good sensitivity to the typical and average currents, but this unconventional design is not without its drawbacks. By integrating the pickup coil inductance directly into our SQUID loop, for example, we improve total flux sensitivity but also introduce an electrical path for the high-frequency currents present in

the SQUID junctions. As opposed to a more standard configuration, where the flux signal measured by the pickup coil is coupled via a flux transformer to a separate SQUID loop [54], our connected configuration allows for GHz-scale Josephson currents in the SQUID loop to couple directly to our Au rings, in the same way that the persistent current signal couples to the SQUID loop. But does this actually affect the persistent current? The classical electromagnetic effects of this SQUID back-action are typically factored into the inductance calculations during the preliminary design process of the lithographic SQUID patterns. In an attempt to rule out possible quantum dephasing effects due to SQUID back-action in our particular inductance design, we have designed a separate test experiment, focusing on the effect of high-frequency Josephson currents on electronic phase coherence.

For any SQUID device, the frequency f_J of the Josephson oscillations depends on the average voltage $\langle v(t) \rangle$ across the SQUID and, ultimately, on the bias current i. For optimized SQUID devices like ours, we can estimate the exact dependence using the following formula [55]:

$$f_J = \frac{\langle v(t) \rangle}{\Phi_0} = \frac{2e}{h} \left\{ iR_{\|} \sqrt{1 - \left[\frac{2I_c}{i} \cos \frac{\pi \Phi_{ext}}{\Phi_0} \right]^2} \right\}, \tag{7.1}$$

where the critical current in the two junctions $2I_c = 10\,\mu$A and the parallel sum of the shunts $R_{\|} = 2.5\,\Omega$. For a typical bias current of $i = 13.6\,\mu A$, we estimate that $f_J = 11.1\,$GHz. From our discussion of the physical parameters of our Au sample in Ch. 5, we note that the phase coherence times determined from weak localization measurements are on the order of nanoseconds. Considering the close correspondence of these different timescales, we propose to measure the effect of high-frequency Josephson currents in a SQUID on the phase coherence time τ_φ

in a closely-coupled mesoscopic Au control-type meander. For our purposes, one key feature is that by tuning the bias current i of the SQUID, we can roughly adjust the frequency of the Josephson oscillations and look for differences in the weak localization correction to the resistance of the meander.

For this test, we use a particular SQUID device (shown in Fig. 7.1) that is identical to the SQUID used in the persistent current measurement, but with a long Au "well" meander patterned in place of the thirty Au rings. Shaped like a well to fit in the $7\,\mu$m gap between the field coils, our meander is $350\,\mu$m in total length, 180 nm wide, and 60 nm thick; it is also fabricated from the same purity gold as the rings and at a similar evaporation rate. The right side of Fig. 7.1 depicts the lithographic pattern of just the meander, showing the large square bonding pads which enable four-terminal measurements of the resistance. At low temperatures, we measure a resistance $R = 760\,\Omega$ and calculate a mean free path $\ell_e = 37\,$nm and a diffusion constant $D = 0.017\,\mathrm{m}^2/\mathrm{s}$. The difference in disorder as compared to our Au rings is partly a result of the difference in linewidths. Designing a wider meander, however, allows us to use the relatively narrow magnetic field range of the on-chip Nb field coils to observe more of the full width of the weak localization correction. In this way the dc SQUID can still be operated as before, without using an external magnetic field coil.

Cooling down to $T = 6.0\,$mK in our dilution refrigerator, we proceed to tune the Josephson frequency only at specific intervals, based on the relative noise performance of the current-biased SQUID. For the four-terminal measurements of the Au well meander, we utilize a low-noise PAR 124A lock-in amplifier set at 26.3 Hz, with a typical excitation current of 10–20 nA across the sample. In Fig. 7.2, we show three overlapping traces of the magnetoresistance, taken

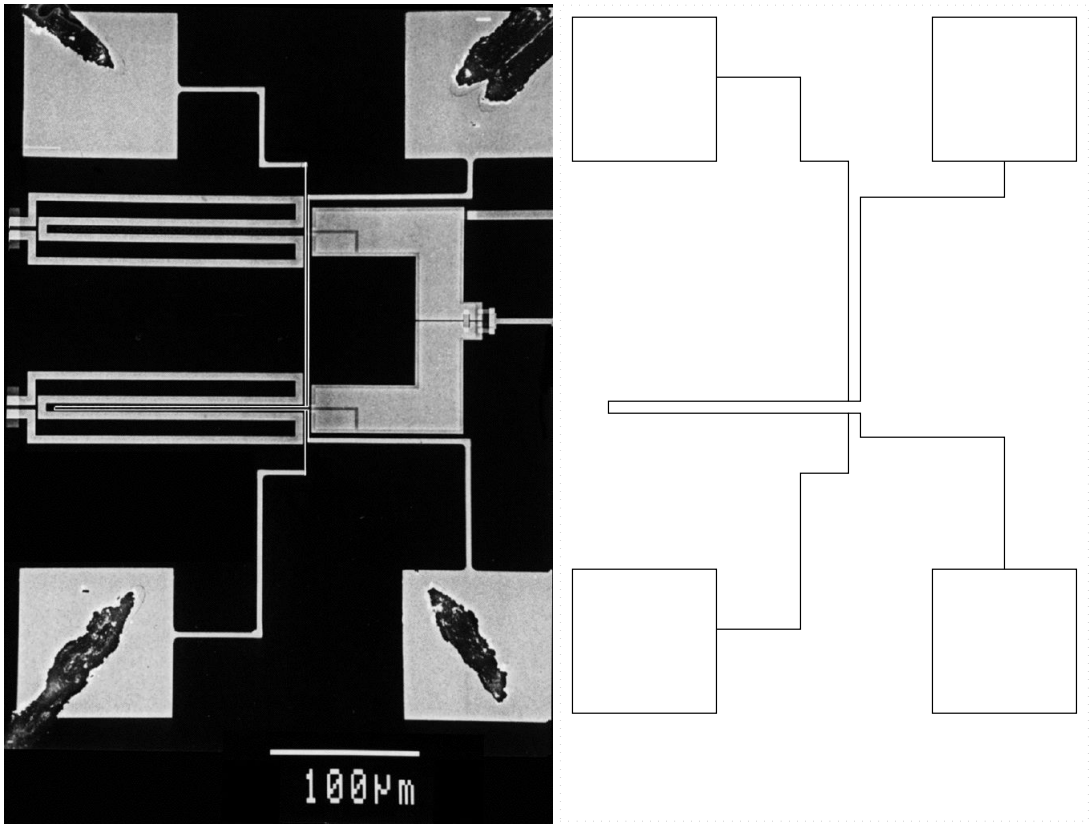

Figure 7.1: Unconventional design of our separate "well" experiment, to check for dephasing effects due to SQUID back-action. A simple 350 nm-long Au meander is patterned – in place of the thirty Au rings – similarly over one arm of the integrated SQUID pickup coil, in the narrow 7 μm gap between the Nb field coils. Also patterned are large square bonding pads which connect to the meander as shown, enabling four-terminal weak localization measurements in order to determine the dephasing effects of high-frequency Josephson currents in the closely-coupled SQUID pickup coil. For clarity, we depict on the right the lithographic pattern of just the well-shaped meander and the bonding pads.

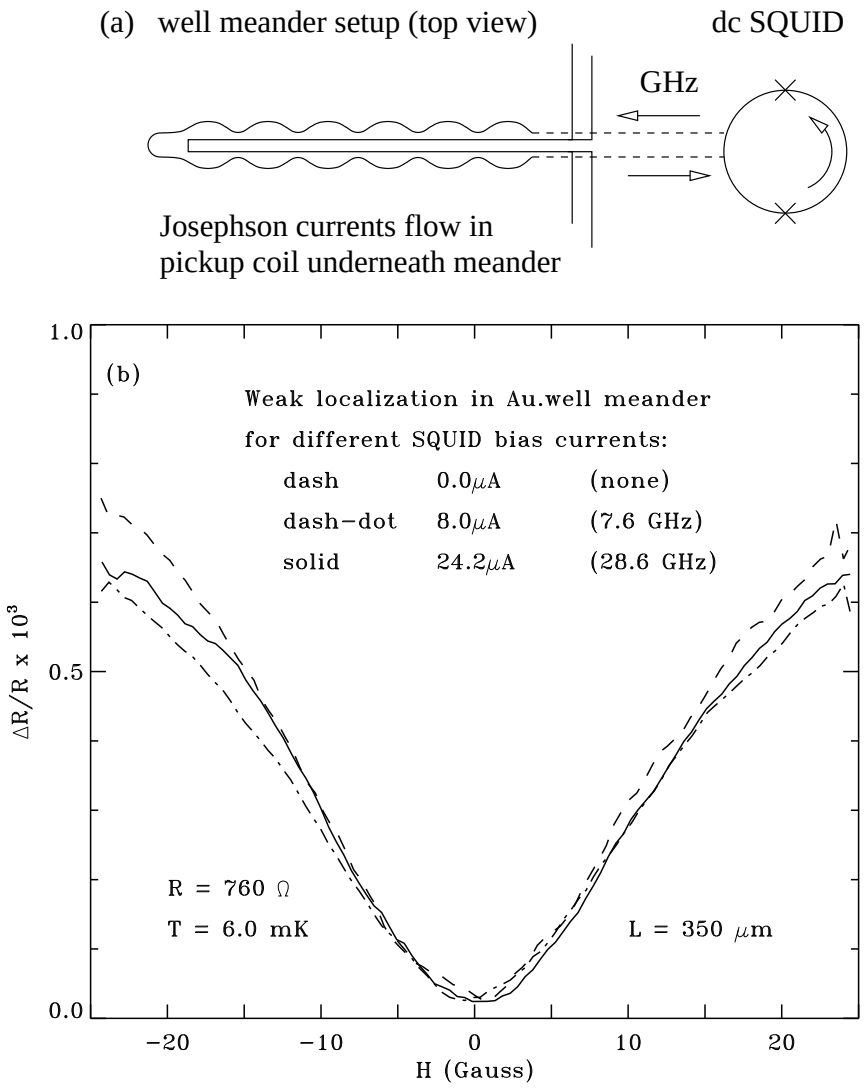

Figure 7.2: Comparison of weak localization measurements in the presence of high-frequency Josephson currents from a dc SQUID. (a) Depending on the bias current of the SQUID, GHz-scale currents flow in the pickup coil underneath the Au well meander. (b) We plot three overlapping traces of the four-terminal magnetoresistance. No change in the overall size of the weak localization correction is seen when varying the frequency of Josephson oscillations with different SQUID bias currents.

with different SQUID bias currents, including no bias at all. In short, we report no change in the overall size of the weak localization correction when varying the frequency of Josephson oscillations. Away from zero field, we do note some nontrivial differences between traces; unfortunately, the critical current of our Nb field coils prevents us from exploring this further at higher magnetic fields.

With regard to the persistent current experiment, these null results necessarily cannot change any of our conclusions. With our integrated SQUID design, the amplitude of the persistent current may indeed be limited by high-frequency Josephson currents even if the phase coherence time τ_φ is not; however, the amplitude is *at least as large* as reported, and larger than or equal to what is theoretically predicted. Our results for the sign are similarly not affected. On a different note, concerning just the measurement of τ_φ, the electromagnetic coupling to our Au well meander is not exactly the same as to our array of Au rings. A better high-frequency decoherence experiment would feature more precise and uniform control of the coupling factor, as well as the exact frequency and power level of the GHz radiation.

7.2 Johnson Noise Temperature

At the end of Ch. 5, we discussed a possible saturation in the temperature dependence of the persistent current and raised the question about thermometry and the actual temperature of our sample. In this Section, we describe the thermometers used to measure the bath temperature in the sample cell, as well as our independent experimental efforts to determine the internal temperature of the electrons in this class of quasi-1D mesoscopic Au systems with weak disor-

der. We then evaluate the intriguing results in the context of the temperature dependence of the persistent current.

For decades, the subject of thermometry has been of considerable challenge to many low-temperature experimentalists [52, 53, 56]. In our commercial (SHE) dilution refrigerator, we depend mainly on the cerium-magnesium nitrate (CMN) thermometer connected to the mixing chamber, based on the Curie-Weiss law $\chi \propto 1/(T-\Delta^{\circ})$ for paramagnetic salts, down to $\sim$ mK temperatures. A commercial (SHE) RLM inductance bridge and (SHE) rf SQUID susceptibility readout are also used with this setup. As a secondary thermometer, we use a germanium resistance thermometer (GRT) also attached to the mixing chamber. In the conventional bottom-loading design of our cryostat, the sample cell is attached to the mixing chamber, such that the sample itself, as well as the substrate and lead contacts, is immersed in the $^3\mathrm{He} - {}^4\mathrm{He}$ solution in the mixing chamber. Regarding the thermal connection to the samples in question, we can investigate the internal electron temperature in this general class of diffusive Au samples from the measured e-e interaction contribution to the resistivity (as described in Ch. 2), as well as the measured Johnson noise temperature in separate samples.

The Johnson-Nyquist relation [57, 58] describes the current noise:

$$\langle I^2 \rangle = 4k_B T_N / R \tag{7.2}$$

arising from the thermal motion of electrons in a sample of resistance R. As compared to the bath temperature T, the noise temperature T_N reflects the intrinsic thermodynamic temperature of the electrons; however, at very low temperatures of order $\sim$ mK, and with resistances of order $\sim$ kΩ, this noise measurement becomes quite challenging. Our solution is to employ a resonant tank circuit along with a sensitive low-noise dc SQUID.

(a) Normal setup with a tightly−coupled planar input coil:

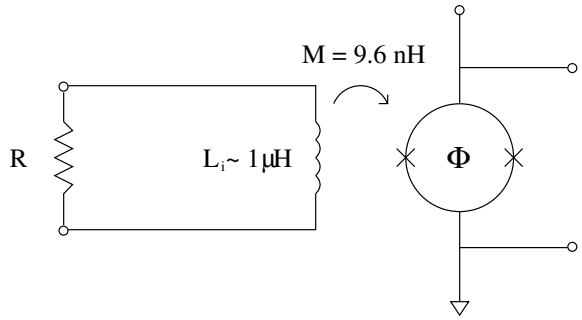

(b) Adding a resonant tank circuit for impedance matching:

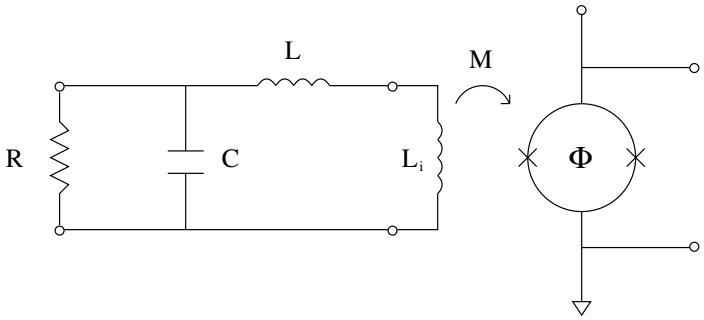

Figure 7.3: Comparison of SQUID input circuits for the Johnson noise measurement of a large resistance at millikelvin temperatures. (a) We start with a low-noise SQUID that incorporates a tightly-coupled planar input coil with mutual inductance $\mathcal{M} = 9.6$ nH. (b) Adding a resonant circuit allows for impedance matching of the resistance R to the SQUID inputs. Our unusual choices for the capacitance $C = 2\,\mu$F and the inductance $L = 2\,$mH combine to amplify the current noise in the resistor at a suitable resonant frequency $f_0 = 2.5\,$kHz. See text for calculations.

We illustrate this point using the simple circuit schematics shown in Fig. 7.3. We start with a specialized IBM-made SQUID (represented in Fig. 7.3(a)) that incorporates a tightly-coupled planar input coil with mutual inductance $\mathcal{M} = 9.6\,\mathrm{nH}$. Even so, at $T = 10\,\mathrm{mK}$, the Johnson current noise in a $R = 5.66\,\mathrm{k}\Omega$ sample:

$$I = (4k_BT/R)^{1/2} = 0.01\,\mathrm{pA}/\sqrt{\mathrm{Hz}} \tag{7.3}$$

results in a coupled flux:

$$\Phi = \mathcal{M}I = 0.05\,\mu\Phi_0/\sqrt{\mathrm{Hz}} \tag{7.4}$$

well below the noise floor of our SQUID detector. Adding a resonant circuit (as shown in Fig. 7.3(b)), however, can make our big resistor $R = 5.66\,\mathrm{k}\Omega$ appear as a smaller resistor r to the SQUID inputs:

$$r = \frac{L}{CR} = 0.17\,\Omega\,, \tag{7.5}$$

where the capacitance $C = 2\,\mu\mathrm{F}$ and the inductance $L = 2\,\mathrm{mH}$. The current noise through this equivalent series resistance is now (again at $T = 10$ mK):

$$I = (4k_BT/r)^{1/2} = 1.8\,\mathrm{pA}/\sqrt{\mathrm{Hz}}, \tag{7.6}$$

and the flux coupled to our SQUID is correspondingly larger:

$$\Phi = \mathcal{M}I = 8.4\,\mu\Phi_0/\sqrt{\mathrm{Hz}}. \tag{7.7}$$

Our choice for the capacitance C and the inductance L of the tank circuit also results in a suitable resonant frequency:

$$f_0 = \frac{1}{2\pi\sqrt{LC}} = 2.5\,\mathrm{kHz} \tag{7.8}$$

well below the unity gain point of the SQUID ($15 - 25\,\mathrm{kHz}$).

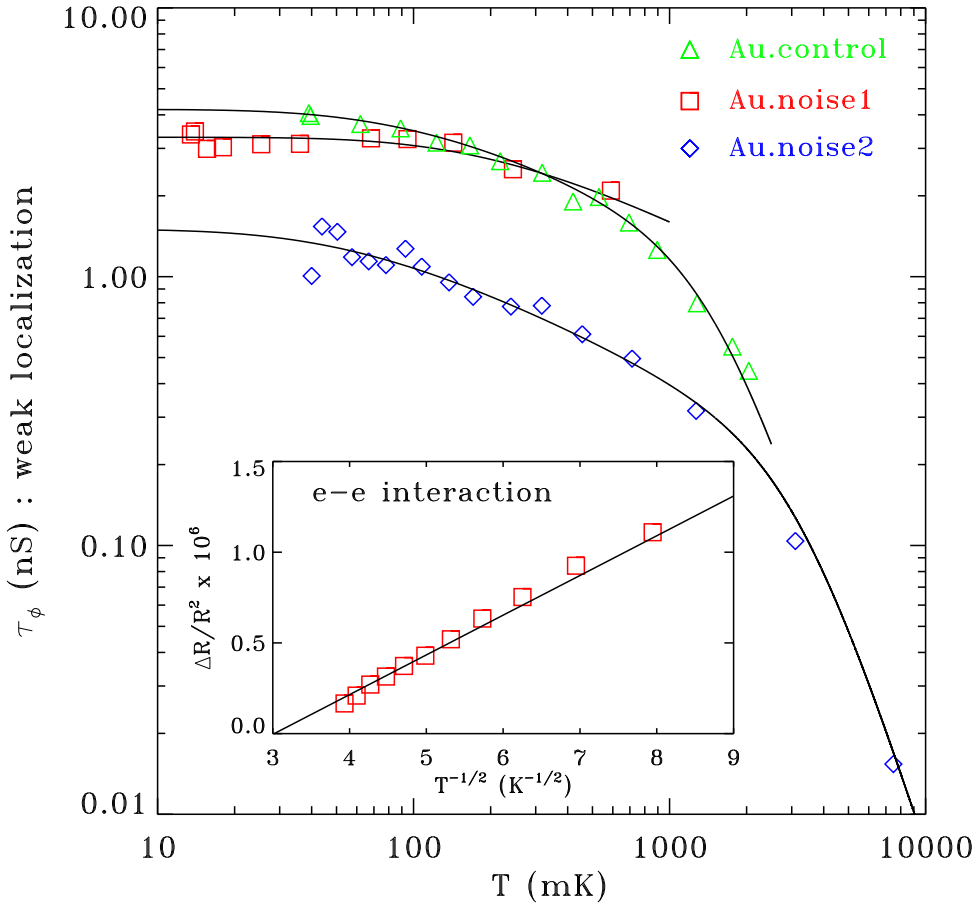

Figure 7.4: Temperature dependence of the phase coherence time τ_φ for the quasi-1D disordered Au wires used in the Johnson noise experiment. The larger graph shows the anomalous saturation of the phase coherence time τ_φ for two Au.noise samples, plus the Au.control meander (△) for the rings in our persistent current experiment. The inset though shows the typical linear $1/\sqrt{T}$ dependence of the e-e interaction correction to the resistivity for one sample (□), suggesting that the electrons are still in equilibrium with the helium bath environment down to lowest temperatures.

Sample	R (kΩ)	L (μm)	w (nm)	t (nm)	D (m^2/s)	τ_0 (ns)
Au.control	0.30	207	110	60	0.061	4.2
Au.noise1	5.66	107	60	38	0.0033	3.3
Au.noise2	2.88	20.3	30	18	0.0051	1.5

Table 7.1: Comparison of standard physical parameters for the Au control meander and the Au noise samples. The last column lists the saturation value τ_0 of the phase coherence time at low temperatures.

In testing new samples for our Johnson noise experiment, four-terminal measurements yield similar results to those found in Ch. 5. Table 7.1 lists the physical parameters of our Au noise samples, as well as the saturation value τ_0 of the phase coherence time at low temperatures. In Fig. 7.4, we show the temperature dependences of two fundamental mesoscopic parameters, the phase coherence time τ_φ and the e-e interaction correction to the resistivity $\Delta R/R^2$, for the two new samples (labeled Au.noise1 and Au.noise2), as well as the Au.control sample data from Sec. 5.2. The larger graph shows the anomalous saturation of the phase coherence time τ_φ for all three Au wires, starting at around 1 K. The strong linear $1/\sqrt{T}$ dependence of the e-e interaction correction to the resistivity, however, suggests that the conduction electrons are still in equilibrium with the helium bath environment down to lowest temperatures.

We briefly describe some preliminary results from our separate experiment on Johnson noise in mesoscopic systems [59]. In Fig. 7.5, we show the temperature dependence of our SQUID-based measurements of the Johnson-Nyquist noise

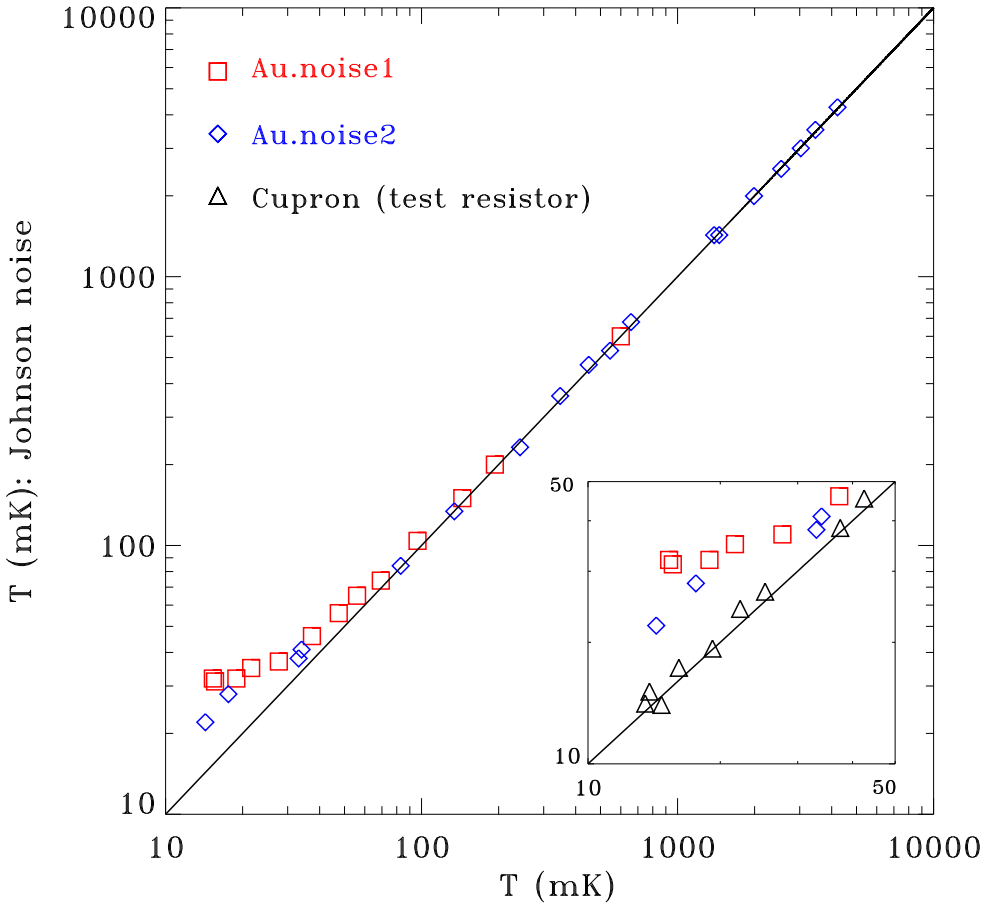

Figure 7.5: Temperature dependence of the Johnson-Nyquist noise temperature for two quasi-1D, disordered Au systems. The larger graph shows the agreement of the measured noise temperature T_N with the bath temperature T in both the Au.noise1 and Au.noise2 samples, down past the relatively high temperatures at which τ_φ demonstrates saturation. The inset zooms in on the region below 50 mK, where the temperature agreement ends without explanation. The measured noise temperature of our control-test ($\triangle$) – a $\sim 3.3\,\mathrm{k}\Omega$ macroscopic resistor wound from common 2-mil Cu-Ni wire – demonstrates no such anomaly.

temperature for these two representative Au meanders. The larger graph shows the agreement of the measured noise temperature T_N with the bath temperature T down past the relatively high temperatures at which τ_φ demonstrates saturation (see Fig. 7.4). In the inset, we focus on the anomalous data below 50 mK, where the noise temperature does not agree with the bath temperature, despite a series of careful checks [59]. For example, we also measure a "macroscopic" control resistor with $R = 3.36\,\mathrm{k}\Omega$, wound from 13.7 meters of 2-mil-diameter commercial Cupron (Cu-Ni) wire: here the Johnson noise temperature shows no such anomaly down to our lowest temperatures of 15 mK. Like the persistent current, Johnson-Nyquist noise is an equilibrium phenomenon that displays some unusual behavior at very low temperatures in our investigations. One possible explanation points to the breakdown of the fluctuation-dissipation theorem in mesoscopic systems. More likely, our measurements include one or more experimental artifacts that further tests will elucidate.

Nevertheless the question of thermometry remains. In combination with the plots of the temperature dependence of the persistent current shown previously in Figs. 5.15 and 5.16, the preliminary data from our Johnson noise experiments suggest that the very low temperature regime deserves more careful consideration, with respect to thermodynamic as well as transport phenomena. Regarding the main results of this thesis on the persistent current, we suggest that any anomalous effects or experimental artifacts should only diminish rather than enhance the amplitude of a robust, periodic signal due to the phase coherence of electrons; hence, both contributions to the persistent current are again *at least* as large as measured. As we discussed in Ch. 6, this fact has important consequences for our understanding of the persistent current problem.

Chapter 8

Conclusion

In this thesis, we have presented the first temperature dependent measurements of both the $h/2e$ and the h/e components of the persistent current from an array of 30 diffusive Au rings. The magnitude of our $h/2e$ response corresponds to an average current per ring of $\sim eE_c/\hbar$, in agreement with previous experiments in multiple-ring systems. The magnitude of our h/e current is also found to be $\sim eE_c/\hbar$. These results, including the diamagnetic signs of the response and the origin of the characteristic scale T_0 in the temperature dependence, cannot be explained completely within the framework of existing theories.

More generally, in contrast to the relatively sparse set of results from prior experiments, this thesis work represents the most complete measurement of the persistent current to date. By focusing on the sign, amplitude, and temperature dependences for both the h/e and $h/2e$ contributions, we fill the specific gaps in knowledge left by previous experiments, especially regarding the sign of the current. We also provide a reference point for each of the studies on diffusive rings, since neither addressed the same contribution to the persistent current. Finally, our measurement on thirty rings is the first to fall in the range between

single ring experiments and measurements of much larger multiple-ring arrays that approach the thermodynamic limit of $N \to \infty$.

As anticipated, our success stems from choosing a statistically small number of rings. We must also credit the unique design of a specialized inductance geometry for our custom-made SQUID detectors. But other, more general factors include the sustained performance of the often temperamental dilution refrigerators used to reach millikelvin temperatures, as well as the controlled fabrication of clean gold samples with long phase coherence lengths. The most critical ingredient may in fact be patience, since every one of the experimental efforts – including ours – has taken years, not months, to complete.

Many of the above challenges may discourage or limit further research on persistent currents, but pressing questions remain: does the sign of the typical current change if the disorder configuration changes? Does the resulting range of amplitudes then follow a Gaussian distribution? For the average current, is the amplitude always larger than expected for ensembles of any size? Does its sign depend on spin-orbit scattering, or on some other experimental variable? For either contribution, what mechanism can account for the robustness of the persistent current signal at higher temperatures? How does the temperature scale relate to the amplitude? And finally, what is the exact relationship between the persistent current problem and intrinsic decoherence in mesoscopic systems? There's still "plenty of room at the bottom" for more work on persistent currents; we can only hope that future researchers will be inspired to pick up the challenge.

Bibliography

[1] R. P. Feynman, Engr. and Sci. (1960).

[2] L. P. Lévy, G. Dolan, J. Dunsmuir, and H. Bouchiat, Phys. Rev. Lett. **64**, 2074 (1990), as well as in Ref. [3].

[3] L. P. Lévy, Physica B **169**, 245 (1991).

[4] V. Chandrasekhar *et al.*, Phys. Rev. Lett. **67**, 3578 (1991).

[5] D. Mailly, C. Chapelier, and A. Benoît, Phys. Rev. Lett. **70**, 2020 (1993), as well as in Ref. [6].

[6] D. Mailly, C. Chapelier, and A. Benoît, Physica B **197**, 514 (1994).

[7] B. Reulet, M. Ramin, H. Bouchiat, and D. Mailly, Phys. Rev. Lett. **75**, 124 (1995), as well as in Ref. [8].

[8] B. Reulet, H. Bouchiat, and D. Mailly, in *Quantum Dynamics of Submicron Structures*, edited by H. A. Cerdeira, B. Kramer, and G. Schön (Kluwer, Dordrecht, The Netherlands, 1995).

[9] E. M. Q. Jariwala, P. Mohanty, M. B. Ketchen, and R. A. Webb, Phys. Rev. Lett. **86**, 1594 (2001).

[10] W. Rabaud *et al.*, Phys. Rev. Lett. **86**, 3124 (2001).

[11] Y. Imry, *Introduction to Mesoscopic Physics* (Oxford University Press, Oxford, 1997).

[12] S. Washburn and R. A. Webb, Adv. Phys. **35**, 375 (1986).

[13] *Mesoscopic Phenomena in Solids*, Vol. 30 of *Modern Problems in Condensed Matter Sciences*, edited by B. L. Altshuler, P. A. Lee, and R. A. Webb (North-Holland, Amsterdam, 1991).

[14] S. Washburn and R. A. Webb, Rep. Prog. Phys. **55**, 1311 (1992).

[15] G. Montambaux, in *Quantum Fluctuations*, Vol. LXIII (1995) of *Les Houches*, edited by S. Reynaud, E. Giacobino, and J. Zinn-Justin (Elsevier Science, Amsterdam, 1997), p. 387.

[16] P. Mohanty, in *Complexity from Microscopic to Macroscopic Scales: Coherence and Large Deviations*, edited by A. T. Skjeltorp and T. Vicsek (Kluwer, Dordrecht, The Netherlands, 2001).

[17] N. W. Ashcroft and N. D. Mermin, *Solid State Physics* (Saunders College Publishing, Fort Worth, TX, 1976).

[18] D. J. Thouless, Phys. Rev. Lett. **39**, 1167 (1977).

[19] B. L. Altshuler, in *Nanostructures and Mesoscopic Systems: Proceedings of the International Symposium*, edited by W. P. Kirk and M. A. Reed (Academic Press, Boston, Santa Fe, NM, 1992), pp. 405–416.

[20] B. L. Altshuler and A. G. Aronov, in *Electron-electron Interactions in Disordered Systems*, edited by M. Pollack and A. L. Efros (North-Holland, Amsterdam, 1985), pp. 1–154.

[21] S. Chakravarty and A. Schmid, Phys. Rep. **140**, 193 (1986).

[22] G. Bergmann, Phys. Rep. **197**, 1 (1984).

[23] P. Mohanty, E. M. Q. Jariwala, and R. A. Webb, Phys. Rev. Lett. **78**, 3366 (1997).

[24] R. P. Feynman and A. R. Hibbs, *Quantum Mechanics and Path Integrals* (McGraw-Hill, New York, 1965).

[25] S. Hikami, A. I. Larkin, and Y. Nagaoka, Prog. Theor. Phys. **63**, 707 (1980).

[26] C. P. Umbach, S. Washburn, R. B. Laibowitz, and R. A. Webb, prb **30**, 4048 (1984).

[27] P. A. Lee, A. D. Stone, and H. Fukuyama, prb **35**, 10039 (1987).

[28] B. L. Altshuler, A. G. Aronov, and D. E. Khmel'nitskii, J. Phys. **C15**, 7367 (1982).

[29] F. Hund, Ann. Phys. (Leipzig) **32**, 102 (1938).

[30] N. Byers and C. N. Yang, Phys. Rev. Lett. **7**, 46 (1961).

[31] M. Büttiker, Y. Imry, and R. Landauer, Physics Letters **96A**, 365 (1983).

[32] H. Bouchiat and G. Montambaux, J. Phys. (Paris) **50**, 2695 (1989).

[33] G. Montambaux *et al.*, Phys. Rev. B **42**, 7647 (1990).

[34] H. Cheung, E. Riedel, and Y. Gefen, Phys. Rev. Lett. **62**, 587 (1989).

[35] V. Ambegaokar and U. Eckern, Phys. Rev. Lett. **65**, 381 (1990).

[36] U. Eckern, Z. Phys. B **82**, 393 (1992).

[37] A. Schmid, Phys. Rev. Lett. **66**, 80 (1991).

[38] F. von Oppen and E. Riedel, Phys. Rev. Lett. **66**, 84 (1991).

[39] B. Altshuler, Y. Gefen, and Y. Imry, Phys. Rev. Lett. **66**, 88 (1991).

[40] V. E. Kravtsov and B. L. Altshuler, Phys. Rev. Lett. **84**, 3394 (2000).

[41] Y. Aharonov and D. Bohm, Phys. Rev. **115**, 485 (1959).

[42] F. Bloch, Phys. Rev. **137**, A787 (1965).

[43] F. Bloch, Phys. Rev. B **2**, 109 (1970).

[44] U. Eckern and A. Schmid, Europhys. Lett. **18**, 457 (1992).

[45] R. Smith and V. Ambegaokar, Europhys. Lett. **20**, 161 (1992).

[46] V. Ambegaokar and U. Eckern, Europhys. Lett. **13**, 733 (1990).

[47] M. B. Ketchen and R. A. Webb, design for "Phoenix 10" integrated dc SQUID.

[48] G. Arfken, *Mathematical Methods for Physicists*, 3rd ed. (Academic Press, Boston, 1985).

[49] M. B. Ketchen *et al.*, Appl. Phys. Lett. **59**, 2609 (1991).

[50] IBM, trimfit 92 software program: inductance modeling and calculation.

[51] F. W. Grover, *Inductance Calculations* (Van Nostrand, New York, 1946).

[52] O. Lounasmaa, *Experimental Principles and Methods Below 1K* (Academic Press, New York, NY, 1974).

[53] G. K. White, *Experimental Techniques in Low-Temperature Physics*, 3rd ed. (Oxford University Press, Oxford, 1979).

[54] M. B. Ketchen and J. M. Jaycox, Appl. Phys. Lett. **40**, 736 (1982).

[55] T. P. Orlando and K. A. Delin, *Foundations of Applied Superconductivity* (Addison-Wesley, Reading, MA, 1991).

[56] R. C. Richardson and E. N. Smith, *Experimental Techniques in Condensed Matter Physics at Low Temperatures* (Addison-Wesley, Redwood City, CA, 1998).

[57] J. Johnson, Phys. Rev. **32**, 97 (1928).

[58] H. Nyquist, Phys. Rev. **32**, 110 (1928).

[59] E. M. Q. Jariwala, T. R. Stevenson, and R. A. Webb (unpublished).